

REDUCTION OF SOLID OXYGEN CARRIER (CuO) BY SOLID FUEL (COAL) IN CHEMICAL LOOPING COMBUSTION

Yan Cao, Zhongxian Cheng, Lingyu Meng,
John, T. Riley, Wei-Ping Pan

Institute for Combustion Science and Environmental Technology
(ICSET)
Western Kentucky University,
Bowling Green, KY 42101
Yan.cao@wku.edu

Introduction

Chemical looping combustion is a promising technology to combine fuel and pure O₂ in-situ, allowing for easy CO₂ sequestration later. However, presently the majority of studies on chemical looping combustion are focused on gaseous fuel, typically natural gas, which has a limited supply and is expensive compared to abundant solid fuels, such as coal¹⁻². Thus, the development of chemical looping combustion with solid fuels will prolong the service time of our major energy resource--coal.

The proposed study of chemical looping combustion by solid fuel will focus on the investigation of possible processes and the establishment of a novel concept for applying the Chemical Looping Combustion (CLC) Process with solid fuel³. The theoretical reaction enthalpy, chemical equilibrium and chemical reaction kinetics for the chemical looping combustion by solid fuel will be studied. In this paper, the reduction of the selected oxygen carrier (CuO) using coal as the fuel supply in this promising combustion technology has been investigated by SDT (TGA+DSC), which simulates a micro-reactor, combined with different characterization tools: FTIR, XRD and SEM-EDX.

Experiment and Instrumentation

Samples. Two samples were used for the experiments. The first sample, referred to as Coal #1, consisted of only Coal #1. The second sample, referred to as a mixture sample, consisted of a 50% (by weight) CuO and 50% Coal #1.

DSC-TGA (SDT). Approximately 10 mg of sample was placed in an alumina pan in an SDT (simultaneous TGA & DTA) 1960 V3.0F and was heated from ambient temperature at 10 °C/min to a range of 800 °C to 900 °C. The experiments were carried out in both ultra-pure high (UHP) CO₂ and UHP N₂. The following parameters are collected after testing: time (min), heating rate (°C/min), weight loss (%), weight loss rate (%/min), corrected heat flow of reaction (w/g), and corrected heat flow rate (w/gmin).

TGA-FTIR. Approximately 10 mg of sample was placed in a ceramic boat and heated from room temperature to 900 °C at a heating rates of 50 °C/min in the TGA 951 under flowing (50 ml/min) UHP CO₂. The Dupont 951 TGA is interfaced to a Perkin Elmer 1650 series Fourier Transform Infrared Spectrometer (FTIR) with a permanent silicon transfer line (length one inch). The purge gas carries the evolved gas from the TGA through a 70 ml-sample cell with KBr crystal windows. The cell is placed in the IR scanning path and is kept at 150 °C by wrapped heating tape to prevent possible condensation. The IR detection range was from 450 cm⁻¹ to 4400 cm⁻¹. The 3D spectra and profiles of gaseous species evolving from the TG system are recorded and analyzed using GRAMS/32 v4 software.

XRD. A THERMO ARL X'TRA X-ray diffractometer using CuK α radiation was used to analyze each of the samples. A tube voltage of 40kV and a tube current of 20mA were used for each sample. The samples were scanned every 0.04 degrees from 20 to 90

degrees. The XRD patterns are identified with a database of over 8000 inorganic compounds.

SEM-EDX. The reaction residue samples were prepared by being doped onto carbon tape. The SEM analysis was performed using a JEOL LSM-5400 SEM. Attached to the SEM for energy-dispersive X-ray analysis (EDX) is a KEVEX Sigma 1 system with a Quantum detector for elemental analysis down to carbon in the periodical table. The instrument operating parameters were as follows: electron beam energy, 15keV; working distance, 30mm; sample tilt angel, 0°; In most cases, two elements, Cu and O, were selected to be analyzed at 2000X magnification.

Test Results

SDT Tests at a higher temperature (900 °C). In this test, reaction paths, reactivity and reaction heat flows for the 2 samples were accurately evaluated using an SDT (TGA+DSC) to simulate a micro-reactor at a high temperature (900°C). The samples were heated at 10°C/min in 2 different atmospheres (CO₂ and N₂). Testing results are shown in **Figures 1** through **Figure 2**.

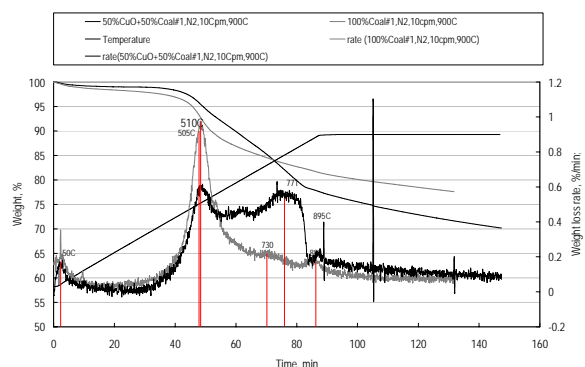


Figure 1-1. Weight loss history of coal #1 and mixture sample in nitrogen with a temperature ramp of 10 °C/min

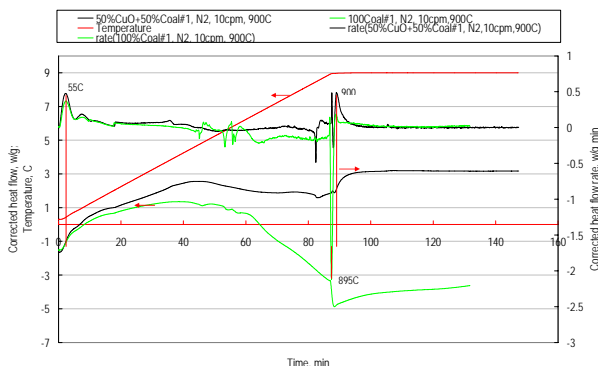


Figure 1-2. Corrected heat flow history of coal #1 and mixture sample in nitrogen with a temperature ramp of 10 °C/min

The nitrogen atmosphere presented the simplest reaction mode for the reduction of the oxygen carrier by coal. Two different reactions could have occurred--one is coal pyrolysis, which is endothermic, and the other is reduction of CuO by coal pyrolysis products, which is an exothermic reaction. Comparison of the weight loss history and the corrected heat flow history in nitrogen between the Coal#1 sample and the mixture sample are shown in **Figure 1-1** and **Figure 1-2**, respectively.

As can be seen in **Figure 1-1**, as the temperature increases starting from atmospheric temperature, 2 peaks evolve at about 50 °C

and about 505 °C for both samples that are attributed to coal moisture loss and partial release of coal pyrolysis products, respectively. Peak heights for the coal sample were a little bit higher than those of the mixture sample due to the fact that the mixture sample contained only half the coal of the Coal #1 sample. As the temperature approaches 770 °C, the peak intensity levels reverse with the mixture sample possessing the larger peaks. This implies that the pyrolysis products of coal or the gasification of coal char have begun reducing the CuO. As the temperature approaches 890 °C, pyrolysis is almost complete, and the reduction of CuO has also decreased. Due to the need for reductants, the reduction process lags behind the pyrolysis process until sufficient reductants have been released. During the coal pyrolysis process, the coal initially releases large molecules at a low temperature of about 400 °C with little exothermic enthalpy variation. However, above 400 °C, the heat flow of the mixture sample goes up and separates from that of the coal sample, which implies that the coupled exothermic reduction reaction of CuO starts and proceeds. The exothermic reduction reaction of the CuO in the mixture sample compensates for the endothermic pyrolysis process, especially around 890 °C; therefore, the heat flow of the mixture sample shows a totally different trend compared with that of the coal sample as can be seen in **Figure 1-2**. It also implies that the reduction reaction of CuO with small pyrolysis molecules is favored under higher temperatures.

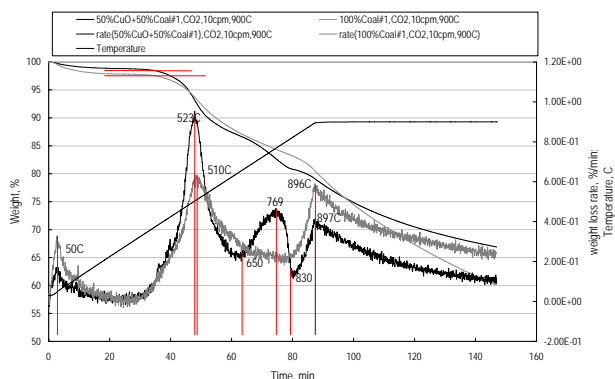


Figure 2-1. Weight loss history of coal #1 and mixture sample in carbon dioxide with a temperature ramp of 10 °C/min

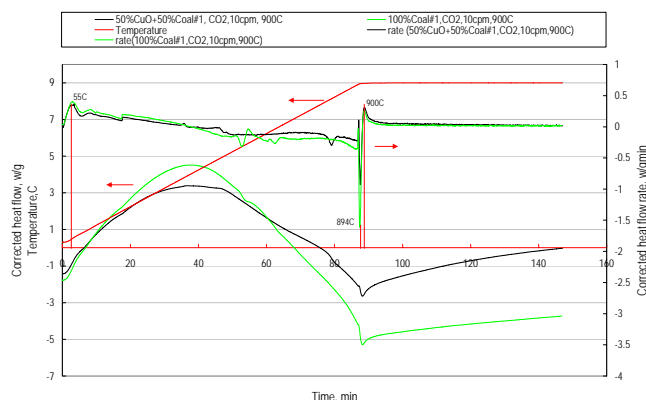



Figure 2-2. Corrected heat flow history of coal #1 and mixture sample in carbon dioxide with a temperature ramp of 10 °C/min.

In a carbon dioxide atmosphere, the reaction paths are far more complicated. Two more reactions are added to the process compared with the results in the nitrogen atmosphere--carbon dioxide

gasification of coal and coal char, which have strong endothermic properties. Comparison of the weight loss history and the corrected heat flow history in carbon dioxide between the Coal#1 sample and the mixture sample are shown in **Figure 2-1** and **Figure 2-2**, respectively.

As the temperature increases from atmospheric temperature, two DTG peaks can be seen at 50 °C and 505 °C for both samples. The peak at 50°C corresponds to coal moisture loss, while the peak at 505°C could be attributed to the partial loss of coal pyrolysis products and/or the carbon dioxide gasification of this product. Also, there may be some coal char gasification. The peak heights are different due to the difference in the amount of coal present as explained above. It is assumed that the gasification of coal pyrolysis products could improve the reduction of CuO due to the increase of small molecular products evolved, such as hydrogen, carbon monoxide and methane, which are more reactive toward CuO reduction compared with the large molecules present in the nitrogen atmosphere. Therefore, no peak is apparent for the carbon dioxide gasification process at 770 °C of the coal #1 sample. However, a large peak is seen from the mixture sample. We believe that above 650 °C, CuO reduction reactivity is improved due to an increase in evolved effective reductants such as H₂, CO and CH₄, with a maximum at about 770 °C. A large peak is seen for the coal sample at 890 °C, which is different from those shown in **Figure 1-1** in the nitrogen atmosphere. It is assumed that the rapid procession of coal char gasification by carbon dioxide at this temperature is responsible for this evolution. This weight loss peak should also have been observed in the mixture sample tests, but it was not seen. The majority of the CuO is believed to have been reduced in the 650°C to 820°C range before the evolution of reductants at 890°C.  s, at temperatures higher than 890 °C, carbon dioxide gasification of coal char is the only reaction occurring in the system.

The heat flow tests clearly verify the above assumptions, as shown in **Figure 2-2**. Two stages appear in heat flow chart. In the lower temperature stage, the heat flow of the mixture sample is a little bit higher than that of coal sample due to reduction of CuO. In the higher temperature stage, heat flow trend line follows that of coal sample to go down due to fact that endothermic property of gasification process dominates the whole process. If there was reactive CuO still available, then the exothermic CuO reduction process should have occurred. After the endothermic peak at 890 °C, the heat flow trend line slowly recovered back to zero which implies a slowdown of the carbon dioxide gasification process as carbon conversion increases.

Products characterizations by FTIR, XRD and SEM-EDX

FTIR. The evolved gas of the mixture sample (50%CuO+ 50% Coal#1) in CO₂ atmosphere from the TGA tests was sent to the FTIR for determination of gas compositions. The 2D FTIR spectras of the mixture sample at the individual times were shown in **Figure 3**. The vertical axis is absorbance units. The horizontal axis is in wavenumbers (cm⁻¹). H₂ can not be detected by FTIR due to its symmetrical stretching molecule structure which is the inactive by infrared spectroscopy. In the whole process as the temperature increases (405, 550, 900 °C), no apparent CO peak appears at spectra wavenumber unit of 2178 cm⁻¹. And the main gas constituents of the mixture sample were CO₂, at spectra wavenumber units of 2359cm⁻¹ (main), 674 cm⁻¹ and 3600-3700 cm⁻¹, and H₂O at wavenumber units of 3800-3900 cm⁻¹ and 1400-1500 cm⁻¹ with some pollutant species.

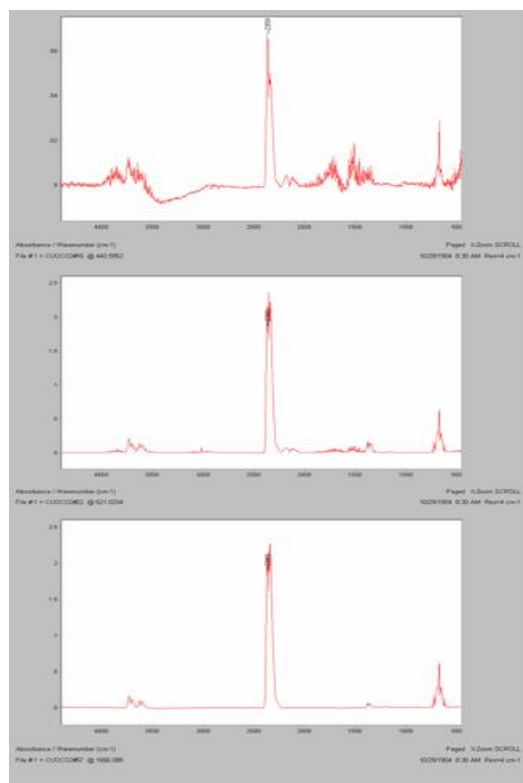


Figure 3. FTIR patterns of 100% Coal#1 and mixture sample of 50% CuO+ 50% Coal#1 at CO₂ atmosphere and heating rate of 50 °Cpm

XRD. 100mg mixture sample of CuO+Coal#1 (50%:50%) were prepared by a DuPont 951TGA for XRD tests. The sample was heated from room temperature to 900°C at a heating rate of 100 deg/min and held for 1hr under CO₂ atmosphere with a flow rate of 50mL/min.

The XRD spectra of the mixture sample residue was shown in **Figure 4**. The 2θ angles and its intensities of XRD spectrum for the chemical pure reference materials and the prepared mixture sample residue were listed in **Table 1**. Peaks with the higher relative intensities were at 43.3°, 30.5° and 50.4°. The 2θ peaks at 43.3° and 50.4° represent Cu phase in the residue of raw mixture sample after CO₂ testing. The peak at 30.5° corresponded to sulfur species in the residue. There is no obvious peak at 35.5° in **Figure 4** indicating most of the CuO was converted into Cu in XRD detection limit. In **Figures 4**, there are no apparent peaks at 36.4° and 42.3°, which indicates there is no Cu₂O in the samples.

Table 1. XRD Spectrum Data from Library And Sample

Item	2θ	Relative Intensity %
CuO	35.5	100
	38.7	96
Cu ₂ O	36.4	100
	42.3	37
Cu	43.3	100
	50.4	46
CuO+Mt Storm Coal 1:1 residue in CO ₂	43.2	100
	50.3	23.09

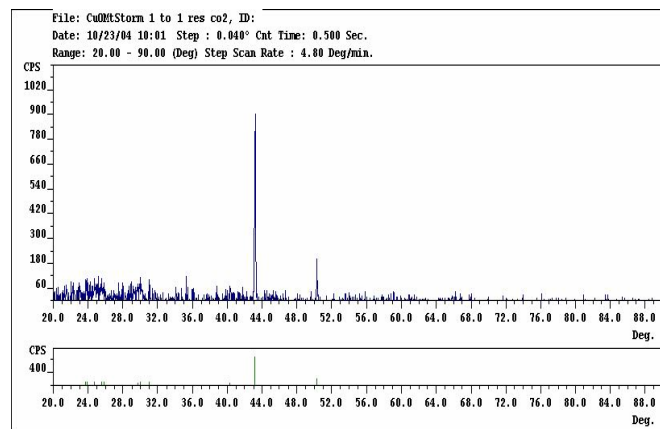


Figure 4. XRD characterization of mixture sample in CO₂ atmosphere

SEM-EDX. SEM images of chemical pure CuO sample changed a lot after being treated at 900 °C for 1hr in CO₂ atmosphere, as shown in **Figure 5** at different magnifications. The previous chemical pure CuO particle lost its original rod-like shape with dimension of 1-3um under treatment of higher temperature. The CuO particles aggregated and developed into larger one with dimension of 5-10 um. Their atom weight ratios were close to 25%:75% by EDX analysis. In CO₂ atmosphere, there should be no reaction occurred, however, some crystal structure of CuO sample may change in higher testing temperature of 900 °C. The SEM images of mixture sample of CuO+Coal under being treated at 900 °C and CO₂ atmosphere were shown in **Figure 6** at different magnifications. Due to larger atom weight of Cu atom in comparison with that of carbon atom, the image of Cu should be much brighter than that of coal char. This is verified by EDX analysis by selected image sites in Figure 7. EDX analysis of the dark site marked with square gives very high carbon atom concentration with about 95% and that of the brighter site marked with circle gives higher Cu atom concentration with 80%, and the oxygen atom concentration is below 10%. The produced Cu particles melt, aggregate and developed into larger cauliflower-like aggregate materials with dimension of 50 um or more, those of coal char size. Some small Cu ball observed is good proof that Cu produced in CuO reduction process is melted and splashed.

The melting and aggregating of Cu produced will result in loss of oxygen carrier capacity. In order to prevent melting and investigate the aggregating phenomena of CuO-Cu system, lower temperatures are suggested in reduction reactor.

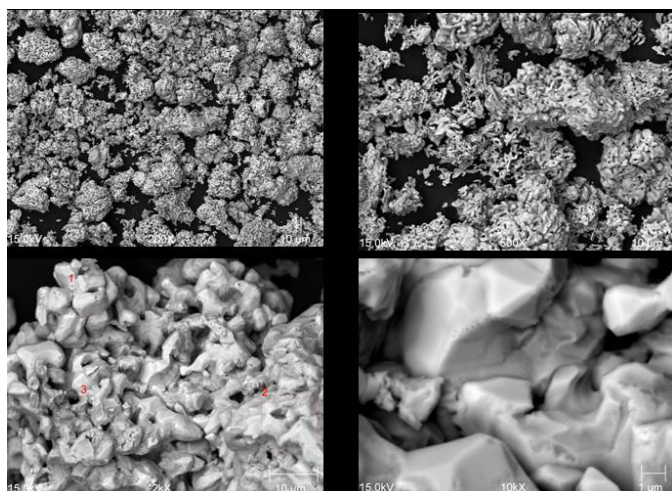


Figure 5. SEM images for sample of CuO at 900 °C, CO₂ atmosphere and temperature ramp of 100 °Cpm

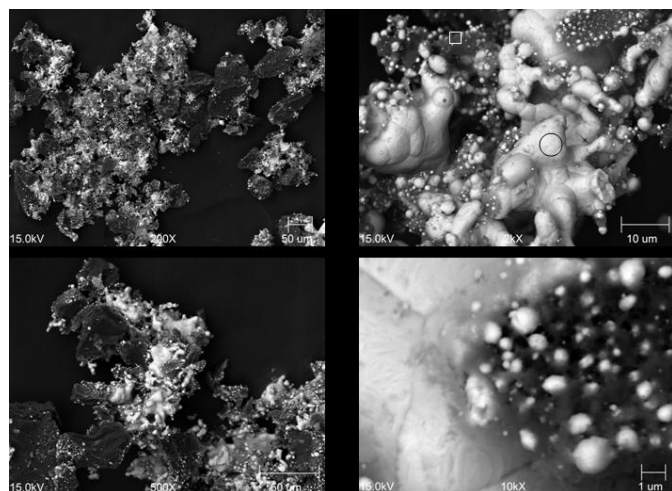


Figure 6. SEM images for mixture sample of 50% CuO+50%Coal at 900 °C, CO₂ atmosphere and temperature ramp of 10 °Cpm

Conclusions

In this paper, utilization of coal in chemical looping combustion technology was investigated by SDT (TGA+DSC), a simulating micro-reactor, combined with the following characterization tools including FTIR, XRD and SEM-EDX for detection of reaction products. The experiment was focused on reduction of the selected oxygen carrier (CuO) by using coal as the fuel supply. Testing results indicated that the oxygen carrier (CuO) could be directly reduced by pyrolytic products of coal in a N₂ atmosphere and by the reducing gas evolved during CO₂ gasification of coal char. The majority of produced gas was found to be CO₂ and H₂O, which is desired. The oxygen carrier (CuO) reduction process started at a lower temperature (approximately 500 °C). A Cu phase could clearly be observed in the SEM-EDX analysis. A suitable temperature range for CuO as oxygen carrier should be below 900 °C in order to control the extent of oxygen carrier melting.

References

- (1) Bredesen, R.; Jordal K.; Bolland, O. *Chemical Engineering and Processing*, **2004**, 43, 1129–1158
- (2) Klara, S.M.; Srivastava, R.D. *Environmental Progress*, **2002**, 21(4), 247-253.
- (3) Yan Cao, Kunlei Liu, John T. Riley, Wei-Ping Pan. *Prepr. Pap. - Am. Chem. Soc., Div. Fuel Chem.*, **2004**, 49 (2), 815.

MOLECULAR BASED KINETIC MODELING OF VACUUM GAS OIL CATALYTIC CRACKING

Ryuzo Tanaka, Michael T. Klein, Prsanna V. Joshi,¹ Wei Wei, Craig A. Bennett, Gang Hou, and Ankush Kumar

School of Engineering
Rutgers, the State University of New Jersey
98 Brett Road, Piscataway, NJ 08854-8058

¹ College of Engineering
University of Delaware
Newark, DE 19716

Introduction

Heavy oil upgrading and ultra-clean fuel production are critical matters for the petroleum industry. Processes must be engineered both to increase refinery efficiency and to protect the environment. One of the practical ways to achieve these goals is the flexible usage of the combination of atmospheric residue hydrodesulfurization (AR-HDS) and fluid catalytic cracking (FCC). The control and fine-tuned optimization of this process would be enhanced through the development of high-fidelity reaction models based on the molecular characters of feedstock. While this is to be developed for the combined process, as a first step, kinetic models of FCC were generated and examined.

Approach

Reaction models are useful tools for process design and control of FCC units. They are used routinely for process optimization: determination of appropriate process conditions and selection of feedstock. Traditionally, due to the complexity of the feedstock and associated analytical and computational hurdles, lumped modeling schemes have been employed for fluid catalytic cracking reaction models.¹⁻³ In such schemes, the entire reaction mixture is described in terms of lumps, defined based on boiling point, solubility or some such physical property. Each lump represents a large number of different molecules with vastly different reactivities. Consequently, lumped reaction models have little chemical significance and limited predictive capabilities.

The new paradigm in reaction modeling is to track each molecule in the feed and the product through the process and to move toward models having fundamental kinetic information and precise predictive capabilities. These notions of reaction modeling at the molecular level have been developed for heterogeneous catalytic processes, as well.⁴⁻⁹

The goal of detailed molecular modeling is to develop models that have good predictive and extrapolative capabilities over a range of process conditions and feedstock. This requires the incorporation of as much fundamental kinetic information as possible. At the most fundamental level the development of such reaction models involves modeling of the chemistry at the mechanistic level. Mechanistic models provide several advantages but their solve time can be very large. In typical industrial applications, such as real time process control, this can be a very debilitating limitation. Hence, there is a need to develop techniques that allow faster solution of the model. One of the model pruning strategies capable of significantly reducing model solution time is stochastic rules, selection during the initial model construction.

Stochastic FCC Model Building Rules

In FCC chemistry, two reaction families - protolytic cleavage and hydride transfer - lead to a combinatorial explosion of species and reactions. In hydride transfer, each ionic species can abstract H from any of the several C-H bonds in the molecule, resulting in new

ionic species. The resultant ionic species undergo further hydride transfer reactions, and so on, thereby setting off the combinatorial explosion. A typical gasoil has molecules with several C - C bonds that are the reactive centers for protolytic cleavage. Each of the many such molecules in a gasoil feedstock can undergo several protolytic cleavages resulting in a large number of species and reactions. It is not useful to eliminate these reactions through use of reaction rules because each of the reaction is a kinetically significant reaction pathway.

A path towards curtailing the combinatorial explosion is through stochastic elimination of protolytic cleavage and hydride transfer reactions. In this scheme, of all the possible kinetically equivalent protolytic cleavage or hydride transfer reactions that a molecule can undergo only a fraction are allowed. The choice is made through stochastic sampling.

First an exhaustive list of all the possible reactive sites in a molecule is generated. The probability of reaction at a particular site is defined by a probability density function. In principle, the probability of reaction at a particular site can account for differences in reaction rate. For example, certain large functional groups, due to geometric constraints, may have a lower probability of reacting at particular sites on a zeolite.

Next, random numbers are generated, and the probability density functions sampled to select from the list the specific reactions to be modeled. The reaction rate constants for these reactions are scaled up appropriately to account for the fact that only a fraction of all the possible reactions have been incorporated in the model. This ensures that the disappearance kinetics for the molecule remains accurate although only a few of all the possible reactions are allowed.

A Case Study

Tetradecane has 13 possible protolytic cleavage sites; pentadecane has 14, hexadecane has 15 and so on. The reaction products are similar in each case, namely, carbenium ions in the range $C_2 - C_{n-1}$ and alkanes in the range $C_1 - C_{n-2}$. Each of the resultant carbenium ions carries out a large number of hydride transfers from all of the linear paraffins and other species, thus resulting in a combinatorial explosion of the reactions and species. It is possible to select, stochastically, a fraction of the protolytic cleavages for each normal paraffin and a few of the hydride transfer for each carbenium ion. This stochastic elimination of the reactions greatly reduces the number of reactions.

The elimination of the reactions through stochastic sampling does not significantly sacrifice chemical significance or skew the product distribution because of compensation effect. Since several similar molecules undergo similar reactions to give similar products, the scaled up reactions of one molecule compensate for the eliminated reactions of the other molecules within the same reaction family. The molecules in gasoil are fairly large and the deviations in product distribution are sufficiently small for gasoil FCC.

Model Verification

Models with stochastic rules were developed for a paraffinic mixture and compared to the model with all reactions explicitly modeled. The feed for the test case was an equimolar mixture of normal paraffins in the carbon range $C_{15} - C_{24}$. **Table 1** summarizes the model diagnostics for the various models. Model 1 includes all possible reactions and provides the benchmark for comparison. In Model 2 and Model 3, only 1/2 and 1/3 respectively of the possible protolytic cleavages and hydride abstractions were stochastically selected.

Table 1. Diagnostics for Various Models

	No. of Species	No. of Reactions	Solution. Time (mins)
Model 1	625	10677	216.13
Model 2	417	5022	26.31
Model 3	403	4563	23.53

A simple probability density function (pdf), zero for the end positions and uniform elsewhere was used. The equation for the pdf is given by

$$f(n, x) = H(x - 2) - H(x - n)$$

where n is the number of carbons,

x is the site carbon; $x \in [1, n]$

H is the heaviside function

Figure 1 compares the results for the three models. The results for all three models are comparable, thereby indicating that it is possible to use stochastic rules without significantly sacrificing chemical significance.

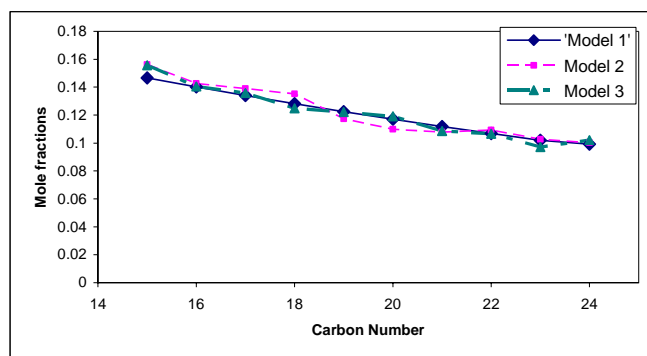


Figure 1. Paraffin Concentrations in Product Stream for Stochastic FCC Mechanistic Model.

The Models 2 and 3 are significantly smaller than the Model 1 and solve almost eight times faster.

References

- (1) Weekman, V. W.; Nace D. M., *AIChE J.* **1970**, *16*, 397-404.
- (2) John, T. M.; Wojciechowski, B. W. *J. Catal.* **1975**, *37*, 348.
- (3) Jacob, S. M.; Gross, B.; Volts, S. E.; Weekman, V. W. *AIChE J.* **1976**, *22*, 701-713.
- (4) Liguras, D. K.; Allen, D. T. *Ind. Eng. Chem. Res.* **1989**, *28*(6), 665-673.
- (5) Liguras, D. K.; Allen, D. T. *Ind. Eng. Chem. Res.* **1989**, *28*(6), 674-683.
- (6) Quann, R. J.; Jaffe, S. B. *Ind. Eng. Chem. Res.* **1992**, *31*(11), 2483-2497.
- (7) Quann, R. J.; Jaffe, S. B. *Chem. Eng. Sci.* **1996**, *51*(10), 1615.
- (8) Watson, B. A.; Klein, M. T.; Harding, R. H. *Ind. Eng. Chem. Res.* **1996**, *35*(5), 506-1516.
- (9) Joshi, P. V., "Molecular and Mechanistic Modeling of Complex process Chemistries: A Generic Approach to Automated Model Building", Ph.D. Dissertation, University of Delaware, 1998.

CHEMICALLY ACTIVATED DECOMPOSITION OF N-PENTYL RADICALS AT HIGH TEMPERATURES

Wing Tsang

National Institute of Standards and Technology
Gaithersburg, MD 20899

Introduction

This presentation is concerned with the chemically activated decomposition of alkyl radicals under high temperature combustion conditions. Alkyl radicals are the immediate products resulting from radical attack on hydrocarbon fuel molecules and hence the first intermediate during their combustion. Their decomposition reactions lead to the production of a 1-olefin and another smaller alkyl radical. These reactions are competitive with oxygen molecule attack on the radical site and the relative rates determine whether oxidative or pyrolytic decomposition mechanisms will be the controlling process. We have been concerned with the rate constants for the thermal decomposition of the larger alkyl radicals. These involve beta bond scissions as well as isomerization processes. The general situation is rendered more complex by the contributions from energy transfer effects. We have been able to solve this problem through a combination of experiments and theory.

There remains one class of decomposition reactions that need to be covered. This involves the chemically activated decomposition of alkyl radicals. Such radicals are formed when hydrogen atoms add to the 1-olefins leading to the formation of alkyl radicals in the 1 and 2 position. The new molecular distribution function for the alkyl radical will now contain the exothermicity of the reaction. The "hot" molecule can now decompose by the reverse ejection of the hydrogen atom, be stabilized by collisions with the bath molecule or undergo the sequence of reaction involving beta bond scission and isomerization. As the temperature is increased the stabilized radical can now also decompose thermally. Thus chemical activation adds another level of complexity to the decomposition process. In this presentation our aim is to describe the phenomenon and give some indication of the consequences of this new contribution to the radical decomposition mechanism.

Practically all the past work on chemically activated decompositions have dealt with studies near room temperature (1). The consequence is that there are no contributions from the thermal decomposition of the stabilized molecule. The aim of the present work is to arrive at a general picture of the case where chemical activation reaction is occurring under combustion temperatures

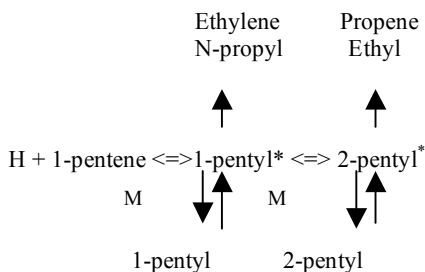


Figure 1: Mechanism for the chemically activated decomposition of 1-pentyl radical

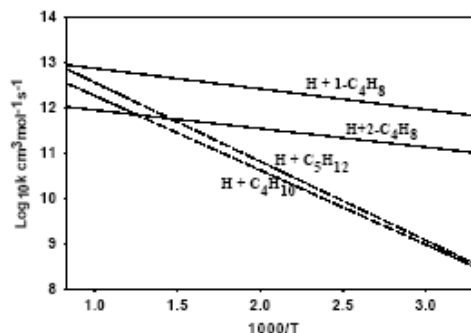


Figure 2: Rate constants for addition to olefins and abstraction from alkanes.

Obviously, at high enough pressures energy transfer will be so fast that chemical activated decomposition cannot occur. On the other hand if chemical activation is of some importance we will be interested in how rate constants and product distributions will be effected.

Scope of Work

The system that we will be describing in detail is the decomposition of 1-pentyl radicals formed as a consequence of the non-terminal addition of hydrogen atom to 1-pentene. This is a prototypical system that has the features (isomerization and decomposition) that is characteristic of all larger alkyl radicals. Figure 1 contains the specific process of interest

These reactions are competitive with abstraction from the non-vinyl hydrogens in the three olefins. This can be seen in Figure 2. Here we compare rate constants for abstraction (2,3) with those for addition (4). It can be seen that at low temperatures the addition reaction is more important despite the large number of abstractable hydrogens. Note that although the 1-olefin contains abstractable allylic hydrogens it is known that their rate constants for hydrogen abstraction is no more than a factor of 2 or 3 larger than comparable secondary hydrogens (5). Thus ignoring addition reactions may have serious consequences up to temperatures in excess of 1000 K. Abstraction from olefins will lead to the formation of dienes such as butadiene. These are much likely precursors of soot than the olefins. Thus the addition of hydrogen to the larger olefins has the consequence of giving alkyl radicals another chance to decompose to form olefins or be reacted with oxygen.

Procedure

Our approach will be to derive the time dependent distribution functions for each of the species from the solution of the time dependent master equation and then to calculate rate constants on the basis of RRKM specific rates (6). A typical distribution function for 1-pentyl radicals formed as a consequence of non-terminal H-atom addition to 1-pentene can be found in Figure 3. It can be seen that there are essentially two regions where the distribution function above the first reaction threshold is invariant. The first is in the region after 10^{-8} sec. Here the flux of input radicals is exactly balanced by those that are stabilized or decomposed. During this time the concentration of deactivated molecule is continually increasing. The rate of thermal decomposition is thus also increasing. When the input flux is now balanced by the thermal and chemically activated decompositions the second and indeed true steady state is

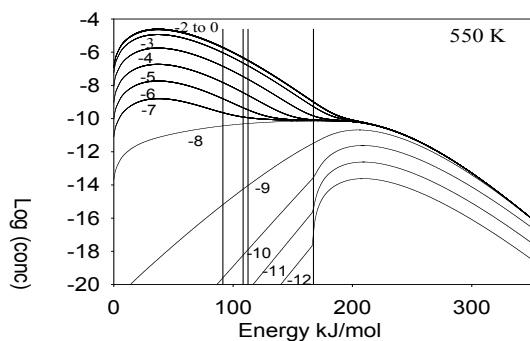


Figure 3: Energy distribution functions as a function of time at 1 bar. The vertical lines are reaction thresholds. The first on the right is for isomerization. The next two are for C-C bond cleavage. The last is for C-H bond cleavage (chemical activation process). The numbers are the logarithm of the time.

reached. The first steady state is the situation for the usual low temperature experiments. In this case it takes so long for the stabilized molecule to reach a concentration where decomposition can occur so that the thermal reaction can be ignored. The reader is reminded that the transition states used in the RRKM calculations are the same for the thermal and chemical activation processes. The only difference is in the initial distribution functions. For thermal reactions it is of course the Boltzmann distribution.

Results

Chemical activation results are usually expressed in terms of decomposition to stabilization ratios or for the present purposes the branching ratio for product formation. Some typical results can be found in Figure 4. At the lowest temperatures the first steady state dominates and after a short incubation time one obtains a constant branching ratio for the four processes. 1-Pentyl radical is the primary product. However some isomerization also occurs. As the temperature is increased. One begins to notice the onset of the second steady state is observed. At the highest temperatures the two steady state region runs into each other.

A particular point of interest is the relative yields from the two isomers. It can be seen that the products from the initial reactant (1-pentyl) predominate under chemical activation conditions and then switches over when the thermal reaction becomes predominant. This is understandable in terms of the formation of very "hot" molecule initially. Thus the isomerization reaction with its low A-factor and despite the low threshold is only weakly accessed. For the thermal decomposition process the longer reaction time and the greater stability of the 2-pentyl radical

The possibility of a time varying rate constant is of course a serious problem when one seeks to use such data for simulation purposes. However it can be seen that at low temperatures the two regions are widely separated. For practical purposes it should be possible to simply use the first steady state branching ratio. At the higher temperatures this is no longer a problem as far as the branching for decomposition is concerned since the two regimes run into each other. However on no longer has constant branching ratio for the stabilization process. Fortunately under such conditions the steady state concentration for the stabilization products is small. Thus little error is introduced by using an average value.

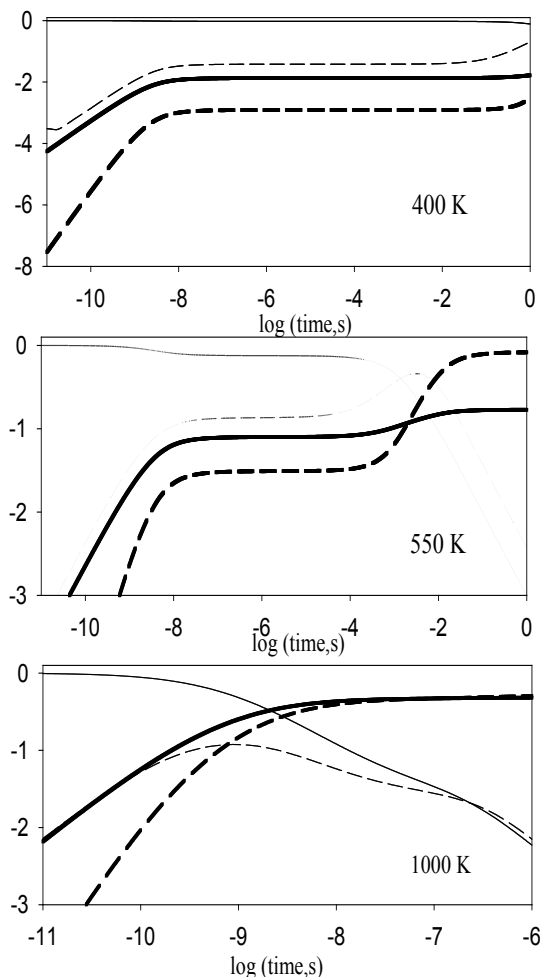


Figure 4: Branching ratio for decomposition and stabilization products during the chemically activated decomposition of 1-pentyl radical from H atom non-terminal addition to 1-pentene. The lines are for 1-pentyl formation (light) and product formation from 1-pentyl (heavy) and 2-pentyl formation (light-dashed) and product formation from 2-pentyl (heavy-dashed). Results are at stated temperature and 1 bar.

Actually it is possible to treat the results in a more rigorous manner. Specifically it is possible to first calculate the branching ratio on the assumption that no thermal decomposition can take place and then calculate the rate constant for the thermal decomposition process using the thermal rate constant appropriate for the reaction pressure for the situation where stabilization product is linearly increasing with time. One can then readily reproduce the curves plotted in Figure 4.

All of these branching ratios are of course functions of the pressure. The effects can be seen in Figure 5 and Figure 4b for reactions at 550 K. As expected, as the pressure is increased the contribution from the chemically activated decomposition is decreased. It appears that the ratio of the branching ratios is also

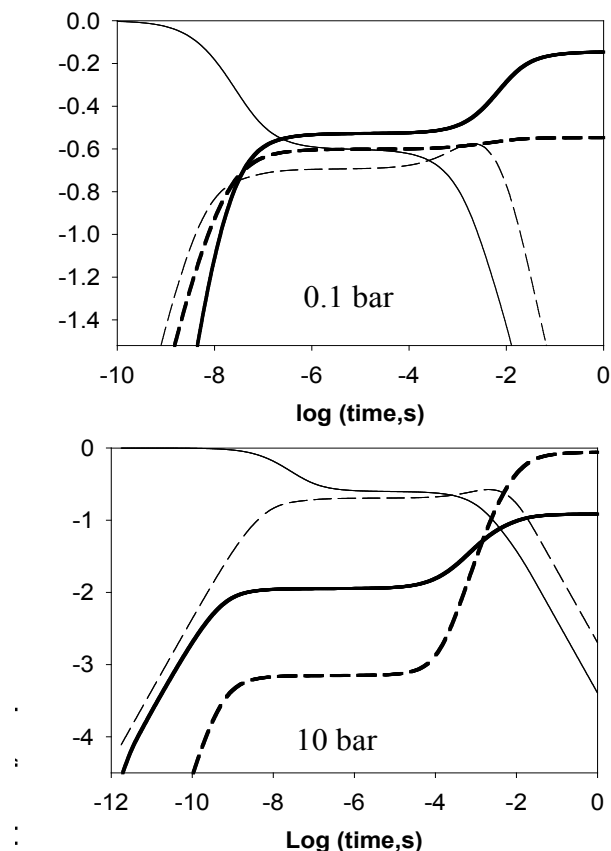


Figure 5: Branching ratios as a function of pressure at 550 K. . The lines are for 1-pentyl formation (light) and product formation from 1-pentyl (heavy) and 2-pentyl formation (light-dashed) and product formation from 2-pentyl (heavy-dashed).

dependent on pressure. A particular interesting aspect of the curves is that the onset of the thermal process is not strongly effected by the pressure.

It is interesting that for OH, the other reactive radical in combustion system, chemical activation processes of this type must be less important. This is because the barrier for beta bond scission involving an OH radical is much lower than that for C-C bond cleavage. Hence OH is more likely to abstract. The consequence is that it is in oxidative systems that more dienes are likely to be formed. On the other hand they are more likely to be destroyed than in the pyrolytic system. These uncertainties on the relative importance of various processes can only be settled when detailed simulations are carried out.

Summary

We have demonstrated the necessity of considering chemically activated decomposition of alkyl radicals during the decomposition of hydrocarbon fuels under combustion conditions. This is because hydrogen atom additions to olefins are at least as important as abstraction processes at temperatures up to 1000 K. Through the solution of the time dependent master equation branching ratios for product formation and reactant stabilization have been determined

using the 1-pentyl decomposition as an illustrative case. The new feature brought about by the high temperatures to chemically activated processes is the contributions from the decomposition of the deactivated molecules. At sufficiently high temperatures the chemically activated and thermal process merge into each other and simplifies the treatment methodology.

References

- (1) Holbrook, K A., Pilling, M. J., and Robertson, S. H., "Unimolecular Reactions" 2nd Ed., John Wiley and Sons, New York, 1996.
- (2) Baldwin, R. R. and Walker, R. W., Trans. Faraday Soc. 1964, 60, 1236.
- (3) Baldwin, R. R. and Walker, R. W., J. Chem. Soc., Faraday Trans. I, 1979, 75, 140.
- (4) Harris, G. W. and Pitts, J. N., J. Chem. Phys., 1982, 77, 3994.
- (5) Tsang, W. and Walker, J.A., 22nd International Symposium on Combustion (The Combustion Institute, Pittsburgh, PA), 101 (1988).
- (6) Tsang, W., Bedanov, V., and Zachariah, M.R., J. Phys. Chem. 100, 4011 (1996).

CPD MODEL CALCULATIONS OF BLACK LIQUOR AND BIOMASS PYROLYSIS

T. Judson Wooters, Larry L. Baxter, and Thomas H. Fletcher,

Department of Chemical Engineering
350 CB, Brigham Young University
Provo, Utah 84604

Introduction

The Chemical Percolation Devolatilization (CPD) model¹ was originally developed to describe coal pyrolysis using a description of coal chemical structure. This model has already been extended to apply to other materials, including polyurethane foams. In this work, the CPD model is applied to black liquor pyrolysis. This project is part of the development of a generalized model for describing the devolatilization of low-grade fuels such as black liquor and biomass. Black liquor is the post pulping residue made up of Kraft lignin (slightly different than the original lignin) and residual carboxylic acids (from the hemicelluloses). The use of a network pyrolysis model like the CPD model has the advantage of being more mechanistic than simple 2-step models, as well as being applicable to a wider range of heating rates and pressures.

Model Background and Application

The CPD model was developed by Fletcher and coworkers¹ to describe coal pyrolysis using five parameters to describe the unique chemical structure of individual coal types (Table 1). Coal is described as a series of aromatic clusters connected by labile or char bridges. Side chains are also attached to the aromatic units. A kinetic model determines rates for bridge breaking, and the relationship between bridges broken and detached clusters is modeled using percolation statistics for Bethe lattices. A pressure-dependent vapor-liquid equilibrium model determines the release of detached clusters. A crosslinking model describes reattachment of metaplast to the char. The model has been demonstrated to predict tar and light gas pyrolysis yields as a function of time, temperature, heating rate, pressure and coal type.

Table 1. Five Structural Parameters

MW _{cl}	Molecular weight of the cluster
M _δ	Molecular weight of side chains
σ+1	Coordination number (number of attachments per cluster)
p ₀	Initial fraction of intact bridges
c ₀	Initial fraction of char bridges

The first four parameters in Table 1 are traditionally determined from ¹³C NMR measurements in the parent fuel. The fifth parameter (c₀) must be found empirically, and was set to zero in this work.

The CPD model uses a coal-type independent set of parameters for the kinetic model. The kinetic model uses competing reactions to predict volatile yields as seen in Figure 1. A broken or intermediate labile bridge can either form two side chains (one for each cluster) or else form a stable char bridge releasing part of the bridge as light gas.

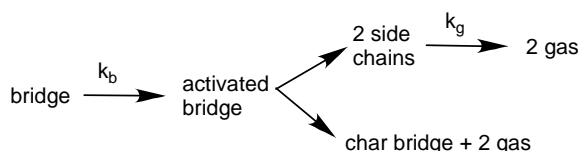


Figure 1. Kinetic Model

For coals, the model was developed assuming a base structure of aromatic clusters connected by bridges, with side chains attached to the aromatic carbons. This approach was used to model black liquor based on average chemical structural parameters. In an alternate approach, structural and kinetic parameters are also determined for each component of biomass (hemicellulose, cellulose, and lignin). In the hemicellulose and cellulose, the base “cluster” unit was set to be the single anomeric carbon with its associated hydrogen. Hemicellulose is composed mainly of xylan and glucomannan. CPD model parameters are shown here for black liquor and xylan.

Experimental Method

The CPD model has been previously used to predict biomass and black liquor volatile yields with limited success; results of previously published modeling attempts^{2,3} were not reproducible due to insufficient documentation or numerical errors. However, the parameters reported in these two studies were useful in guiding this work.

The structure of a black liquor sample was analyzed by ¹³C NMR spectroscopy.⁴ Because black liquor consists largely of lignin, which is similar in structure to low-rank coals, initial kinetic parameters were originally set to the coal-independent values. Optimization of these kinetic parameters for black liquor was then performed by comparison with black liquor devolatilization data.

Xylan structural parameters were derived from theory alone.⁵ The kinetic parameter guesses for xylan were originally set to those reported by Sheng and Azevedo³ for hemicellulose, then optimized by comparison with data.

Modeling of the three other constituents (cellulose, lignin, and glucomannan) is currently in progress.

Experimental Data

Webster et al.⁶ measured black liquor pyrolysis yields in a nitrogen-purged furnace as a function of temperature. The black liquor was finely ground and 0.7 g was placed in a ceramic crucible. The black liquor was placed in the furnace for 10 minutes, where it was heated at a rate of 100 K/s to the desired final temperature. Data were also obtained by Iisa⁷ in a laminar entrained flow facility, with a heating rate of approximately 10⁴ K/s and residence times of less than a second.

Data on pyrolysis of xylan were obtained as a function of temperature at a heating rate of 0.33 K/s in a TGA by Alen et al.⁸

Results and Discussion

Structural Parameters. The NMR analysis of black liquor yielded a value for the coordination number (σ+1) of 3.6, which was used in the model. The coordination number found theoretically for Kraft lignin was 3.5, which was similar to the NMR results for black liquor but lower than the value of 4 used by Sricharoenchaikul.³ The initial fraction of intact bridges (p₀) determined from the NMR analysis was 0.33; the percolation threshold (1/σ) where no connected lattice exists was 0.38 for this sample. This indicates that the measured value of p₀ is not feasible. The NMR measurements may have been affected by the silica gel mixed with the black liquor sample or by the inherent minerals and/or the high oxygen content of the black liquor. The value of M_δ = 60 measured by NMR also seems incorrect based on theoretical lignin values (34-39); so a value of 37 was used. Finally, a value of MW_{cl} of 292 was used, which was close to the value of 297 determined by NMR.

Xylan exhibits slightly different chemical structures in hardwood and softwood. Both are sugars consisting of a backbone of xylose, but each has slightly different attachments. Hardwood xylan has methoxy-glucuronic acid side chains attached to every tenth

xylan molecule. Softwood xylan has more methoxy-glucuronic acid (attached to every fifth xylan molecule), but also has an arabinose attachment every 10th xylan.⁵ Even with these differences, the final structural parameters determined for the CPD model for both hardwood and softwood xylan were similar, and were set to be identical. Xylan therefore is assumed to have three attachments, all intact bridges: 1 ether bridge, and 2 bridges that comprise the sugar ring and attached side chains. Table 3 reports the structural parameters for both black liquor and xylan used here.

Table 3. Structural Parameters

	MW _{cl}	M _δ	p _o	σ+1
Black Liquor	297	37	.71	3.6
Xylan	85	24	1.0	3.0

Kinetic Parameters. Table 4 reports kinetic values obtained through fitting available measured volatile yields. Since the approach was to start with the coal-independent values and change as few parameters as possible, any changes for black liquor parameters are highlighted. For xylan, any changes made from the hemicellulose parameters of Sheng and Azevedo² are highlighted.

Table 4. Kinetic Parameters

	Coal ¹	Black Liquor	Hemicellulose ²	Xylan
E _b	2.60E+15	3.66E+18	1.00E+18	1.18E+18
A _b	55400	55400	51500	51500
σ _b	1800	1800	2500	100
E _g	0.9	0.9	0.01	1.08
A _g	0	0	-4900	0
σ _g	3.00E+15	6.33E+08	5.00E+12	5.00E+12
ρ	69000	41000	38200	38200
E _c	8100	3663	5000	5000
E _{cross}	3.00E+15	3.00E+15	3.00E+15	3.00E+15
A _{cross}	65000	65000	65000	65000

Total Volatiles. Only total volatile release was measured in these experiments; tar yield and gas species data were unavailable. Figure 2 shows that a good fit of both the Webster data and the Lisa data can be obtained using the parameters in Table 2. The high temperature data (above 1100 K) show mineral release, which is not treated by the CPD model. The modeling results for black liquor are actually the results of separate computations at each temperature.

A comparison of CPD model calculations with xylan data is shown in Figure 3. A very good fit to these data was achieved, matching the main rise in volatiles yield at 550-600 K as well as the final yield under these slow heating conditions. The initial mass release (below 500 K) is thought to be early CO₂ and/or H₂O release, and is not treated here.

Summary and Conclusion

The CPD model was shown to match limited data from black liquor pyrolysis using realistic chemical structure parameters and changes to 4 kinetic parameters from the values used for coal. The beginnings of a biomass pyrolysis model were shown by matching a portion of hemicellulose data (i.e., xylan). Predictions for cellulose and lignin pyrolysis are currently underway.

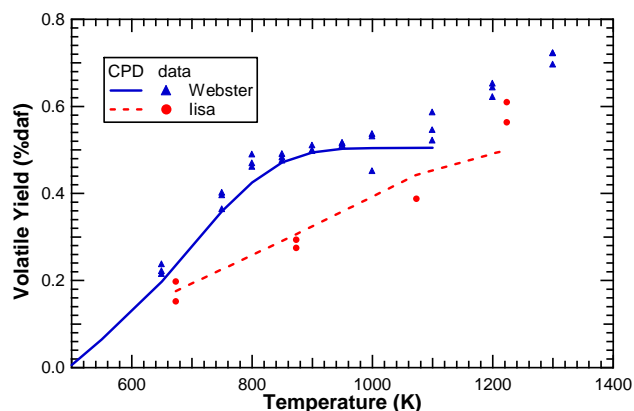


Figure 2. Comparison of CPD model calculations with black liquor pyrolysis data of Webster et al.⁶ and Lisa.⁷

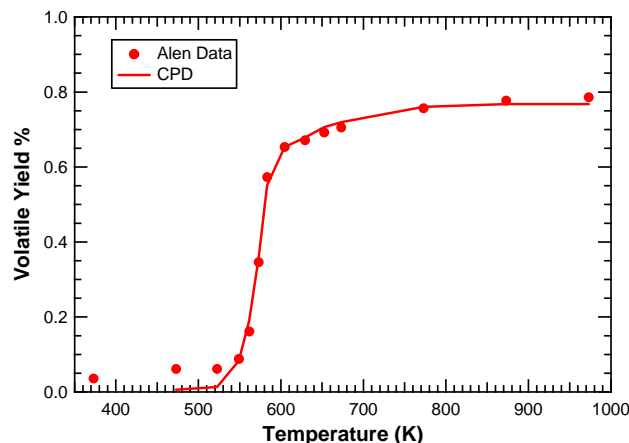


Figure 3. Comparison of CPD model calculation with xylan pyrolysis data of Alen et al.⁸

Acknowledgment

Work supported by the DOE Office of Industrial Technologies, Weyerhaeuser, International Paper, Georgia Pacific, and Boise Cascade.

References

1. Fletcher, T.H., Kerstein, A.R., Pugmire, R.J., Solum, M.S., Grant, D.M., *Energy & Fuels*, 1992, 6, 414-431.
2. Sheng, C., Azevedo, J.L.T. *29th International Symposium on Combustion*. 2002.
3. Sricharoenchaikul, V., *PhD Thesis*. 2001, Georgia Institute of Technology.
4. Solum, M. S., personal communication, 2002.
5. Ni, Y, Che 3801 Chemistry in Pulp and Paper Class Lecture 5, Pulp and Paper Research and Education. University of New Brunswick.
6. Webster, J.D., Fletcher, T.H., Baxter, L.L. 3rd Annual Joint Meeting of the U.S. Sections of the Combustion Institute. March, 2003, Chicago IL.
7. Lisa, K., Improved Recovery Boiler Performance Through Control of Combustion, Sulfur and Alkali Chemistry: Quarterly Report (Jan – Mar 2004). Chalmers University of Technology.
8. Alen, R., Ryttonen, S., McKeough, P., *Journal of Analytical and Applied Pyrolysis*, 1995, 31, 1 – 13.

THERMODYNAMIC ANALYSIS OF AUTOTHERMAL REFORMING OF LIGHT HYDROCARBONS FOR HYDROGEN

Wuyin Wang, Scott Q. Turn, Vheissu Keffer, Aurelien Douette

Hawaii Natural Energy Institute,
University of Hawaii,
1680 East-West Road, POST 109,
Honolulu, HI 96822
Email: Wuyin@hawaii.edu;
Tel: 808-956-5397; Fax: 808-956-2344

Introduction

Light hydrocarbons such as natural gas and liquefied petroleum gas (LPG) can be a convenient and promising source of hydrogen for PEM fuel cell^{1, 2, 3}. The components in natural gas and LPG include methane, ethane, propane, propylene, butane and pentane. Autothermal reforming (ATR) is an attractive practical process². Hydrogen-rich gas can be produced through catalytic reforming of the hydrocarbons in the presence of air and steam, followed by water gas shift (WGS).

The reaction between fuel and steam is endothermic and the reaction between fuel and oxygen is exothermic. Thermodynamic analysis of the autothermal process includes global mass balance, equilibrium of reactions and energy balance. Ahmed and Krumpelt² studied efficiency of reforming processes for different fuels under conditions of thermo neutrality. Their work presented maximum hydrogen yield from global chemical reaction. Theoretical maximum fuel processing efficiencies were determined based on vehicle applications and included losses associated with exhaust gas discharge without heat recovery, i.e. water in vapor state, LHV basis. Lutz et al.⁴ applied global reaction balances and chemical equilibrium in their analysis. Oxygen-to-carbon ration (O/C) and steam-to-carbon ratio (S/C) were optimized using only chemical equilibrium at high reforming temperature. Heat loss of the process was not addressed. Avci et al.³ reported a sophisticated simulation involving detailed reaction path. Not only thermodynamic data but also conversion data and kinetic equations were included.

This paper presents a simple analysis including global reaction balance, chemical equilibrium, and changes in enthalpy through the process. Process parameters, O/C and S/C, are optimized at maximum fuel processing efficiency under thermo neutral condition.

Thermodynamic Analysis

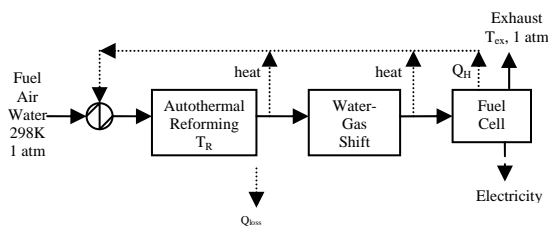
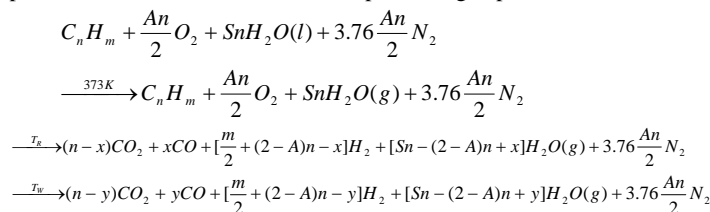


Figure 1. Schematic diagram of the reforming process.

The reforming process studied is shown in Figure 1. Light hydrocarbon fuels, air and water are introduced at 298 K, 1 atm. The inlet stream is heated by heat exchange with hot gases from downstream components. Above light-off temperature, the hydrocarbons start to react. Autothermal reforming is carried out at high temperature T_R . After the ATR the gases are cooled and undergo water-gas shift at T_W to reduce CO. Autothermal reforming and water-gas shift are included in the analysis. Further removal of CO is not included and will be discussed later. The energy balance is based

on a unit amount of fuel. Thermodynamic data are taken from FACTSage software and NIST WebBook⁵.

Mass balance. Thermodynamic analyses of hydrocarbons, methane, ethane, propane, propylene, butane and pentane, are performed. General reaction for fuel processing is presented below.



In the equations, A stands for O/C, S for S/C (H_2O/C), T_R for reforming temperature, and T_W for water gas shift temperature. Complete conversion of hydrocarbons is assumed in catalytic reforming. From the equations, the amount of hydrogen generated is $\left[\frac{m}{2} + (2-A)n - y \right]$ mol, which seems to be independent of steam/carbon ratio. However steam is required to shift equilibrium towards hydrogen generation.

Chemical equilibrium. Equilibrium is assumed to be reached for autothermal reforming and for water-gas shift. The equilibrium constant for water-gas shift reaction is expressed as:

$$K_p = \frac{P_{CO_2} P_{H_2}}{P_{CO} P_{H_2O}}$$

Energy balance. a. Heat of reaction (kJ/mol fuel) for ATR and WGS is derived from heat of formation at reaction temperatures h_i^f , where h_i^f includes the enthalpy of formation at standard conditions plus the sensible enthalpy at the reaction temperature.

$$\Delta H_R = \sum_{products} M_i h_i^f - \sum_{reactants} M_i h_i^f$$

M denotes moles of gas.

b. Heat of vaporization (kJ/mol fuel) of water at 373K, 1 atm is $\Delta H_V = 40.9 Sn$

c. Heat exchange in the sensible heat (kJ/mol fuel) of the cold and hot streams is calculated by:

$$\Delta H_{T_1}^{T_2} = \sum_i M_i \int_{T_1}^{T_2} C_{p,i}(T) dT$$

$$C_{p,i} = \sum_k C_k T^{P_k}$$

d. Heat loss (Q_{loss}) includes loss of the heat produced by the reactions and changes in enthalpy of hot streams. Heat loss from 0% to 50% is discussed. Heat loss of 20% is used in comparison of hydrocarbons.

e. Energy in exhaust gas includes sensible heat of gas and latent heat of steam. Recovery this part of heat will increase the thermal efficiency of the reforming process. In addition, it is assumed that the fuel cell will utilize about 80% of hydrogen fed to it and that the exhaust gas will contain about 8% hydrogen. Combusting the hydrogen from the fuel cell exhaust gas can improve the efficiency for the overall process of fuel to electricity.

Optimization of S/C and O/C. Process parameters: S/C and O/C are optimized by maximizing fuel processing efficiency (η) without external energy input.

$$\max(\eta) \text{ at } EB \geq 0$$

$$\text{and } \eta = \frac{M_{H_2} \cdot HHV_{H_2}}{M_{C_n H_m} \cdot HHV_{C_n H_m}}$$

EB is energy balance and M is mole of gas. Higher heating values (HHV) of hydrogen and of hydrocarbons are used, since final exhaust gas might be cooled before discharging.

The calculation is conducted taking 1 mole fuel as the basis and 298 K, 1 atm as the base state. Temperatures for ATR, WGS and fuel cell are selected to be 1073K, 573K and 353K, respectively. The energy balance is expressed as (kJ/mol fuel):

$$EB = -(\Delta H_{298}^{373} + \Delta H_v + \Delta H_{373}^{1073} + \Delta H_{R,ATR}^{1073} + \Delta H_{1073}^{573} + \Delta H_{R,WGS}^{573} + \Delta H_{573}^{353}) - Q_{loss}$$

Depending on whether the rejected hydrogen will be combusted, the exhaust gas from fuel cell may be heated or cooled. Energy in the exhaust gas, Q_{H_2} , is not included in the above energy balance.

Results and Discussion

Distribution of energy in autothermal reforming of propane.

In autothermal reforming, chemical energy of hydrocarbons (HHV) is converted to that of hydrogen, but heat loss and energy discharged with exhaust gas can't be avoided. Figure 2 gives an example of energy distribution in autothermal reforming of 1 mole propane. Heat loss is 20%. CO is assumed to be completely converted to H_2 . The fuel processing efficiency of the process is 85.5%. Up to 4% efficiency improvement can be achieved by recovering sensible and latent heat in the exhaust gas. Combusting the rejected hydrogen (18.0% of the total in Figure 2) can considerably improve fuel utilization.

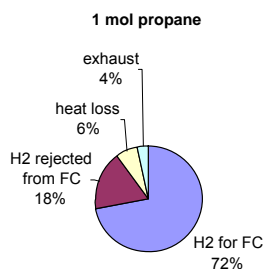


Figure 2. Distribution of energy in autothermal reforming of 1 mole propane.

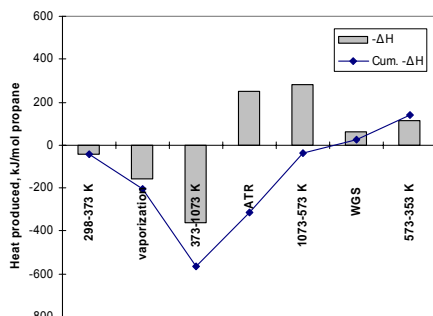


Figure 3. Heat budget for steps in the reforming process.

Figure 3 shows changes in enthalpy for each step and cumulative enthalpy changes in fuel processing. Raising temperatures of the inlet stream requires heat in the first three steps. Then, ATR and WGS reactions and cooling of the hot exit stream release heat for heat exchange. Note that in real situation, inlet gases only need to be heated to light-off temperatures of hydrocarbons to start ATR. In that case, step 3 will be less negative and step 4 (ATR) will be less positive, but the net sum of step 3 and 4 will be the same. If the heat loss of the process can be maintained at or below the small positive enthalpy value shown at the end of cumulative enthalpy change (Figure 3), then the process does not require external heat addition.

Hydrocarbons. Results of optimization for hydrocarbons with 20% heat loss are summarized in the upper part of Table 1. The differences between hydrocarbons are small, except for propylene. The higher S/C and lower O/C value for propylene result from lower ratio of H/C and higher energy content for propylene. Fuel processing efficiencies are around 85% to 87%. Hydrogen in reformat is about 40%. O/C is around one and S/C is about 1.3. Operating at this low S/C ratio could cause coking on catalyst surfaces. Combusting the rejected hydrogen from the fuel cell will lead to higher optimal value of S/C and improve the conversion conditions.

Table 1. Results of Thermodynamic Analysis for Hydrocarbons with 20% Heat Loss, and Propane with 0-50% Heat Loss.

	Heat loss (%)	Fuel processing efficiency (%)	O/C	S/C	H ₂ (%)
Methane	20	87.0	1.16	1.17	42.7
Ethane	20	86.0	1.03	1.28	41.1
Propylene	20	85.0	0.851	1.44	40.5
Propane	20	85.5	1.01	1.30	40.1
Butane	20	85.3	0.991	1.31	39.6
Pentane	20	85.1	0.983	1.31	39.3
Propane	0	91.8	0.860	1.58	43.0
	10	89.0	0.926	1.44	41.7
	20	85.5	1.01	1.30	40.1
	35	78.8	1.16	1.04	36.7
	50	69.0	1.40	0.693	31.6

Heat loss. The lower part of Table 1 shows the results for propane with 0% to 50% heat loss. At higher heat loss, more fuel is oxidized to provide heat, causing O/C to be higher, and S/C and process efficiency to be lower. Thermal integration and adequate insulation are important for fuel processing efficiency.

CO reduction. At 573K about 2% CO is left after WGS. Further CO removal can be achieved by WGS at temperature below 473K, by methanation, or by preferential CO oxidation with oxygen. The latter two options may result in a reduction of hydrogen, as methanation of CO consumes hydrogen and in preferential oxidation as much as double amount of air needed is injected ⁶.

Conclusions

Thermodynamic analysis of autothermal reforming of light hydrocarbons was performed with consideration of global mass balances, chemical equilibrium, and changes in enthalpy in the process. The simple analysis provided good understanding of autothermal reforming of light hydrocarbons. Thermal integration and insulation were of design importance. Operating parameters, S/C and O/C, were optimized with no external heat input. The optimal values for hydrocarbons are similar, except for propylene. Heat recovered from the fuel cell exhaust gas will provide small improvement in the fuel processing efficiency. Combusting hydrogen rejected by the fuel cell is favored for the overall fuel utilization, as well as for avoiding the coking problem due to low S/C.

References

- (1) Wang, W.; Turn, Q. T.; Keffer, V.; Douette, A. Prepr. Pap. - Am. Chem. Soc., Div. Fuel Chem., **2004**, 49 (1).
- (2) Ahmed, S.; Krumpelt, M. *Int. J. Hydrogen Energy*, **2001**, 26, 291-301.
- (3) Avci, A. K.; Önsan Z. I.; Trimm, D. L. *Appl. Catal. A: General*, **2001**, 216, 243-256.
- (4) Lutz, A. E.; Bradshaw, R. W.; Bromberg, L.; Rabinovich, A. *Int. J. Hydrogen Energy*, **2004**, 29, 809-816.
- (5) NIST Chemistry WebBook. <http://webbook.nist.gov/chemistry/>.
- (6) Brown, L. F. *Int. J. Hydrogen Energy*, **2001**, 26, 381-397.

MECHANISTIC STUDIES OF HYDROGEN FORMATION FROM AMINEBORANE

R. Scott Smith, Bruce D. Kay, Benjamin Schmid, Liyu Li, Nancy Hess, Maciej Gutowski & Tom Autrey

Pacific Northwest National Laboratory, Richland, WA 99252
University of Oregon, Eugene, OR

Introduction

There is currently great scientific and public interest in the future prospects of a hydrogen-based energy economy.¹⁻² The potential advantages of a *Hydrogen Economy* are far reaching, from the promise of an environmentally clean energy source through utilization of renewable fuels to an enhanced energy security where we are no longer dependent upon petroleum reserves. If we are to successful transition from an oil based energy economy to a hydrogen based energy economy significant progress in research to increase the efficiency and life time of fuel cells, decrease the economics costs of hydrogen production and the discovery of new materials to store adequate volumetric and gravimetric quantities of hydrogen, especial for on-board FC vehicular applications are needed. Recently, two critical reports suggested that significant new effort in fundamental research focused on these three crucial areas, storage, production and FC's, will be paramount to the success of a hydrogen economy.³⁻⁴

Our group has been working on developing a better fundamental understanding of the chemical and physical properties of amine borane complexes.⁵⁻⁷ These materials, especial ammonia borane (AB), NH_3BH_3 have high theoretical gravimetric (0.195 kg H_2 /kg) storage density. AB is isoelectronic with ethane yet is a solid at ambient temperatures with a density of 0.75 gm/cc providing a volumetric density of (0.142 kg H_2 /liter). AB is composed of a network of non-classical dihydrogen bonds formed between the hydridic hydrogens on boron and acidic hydrogen atoms on nitrogen ($\text{N}-\text{H}^{\delta+} \cdots \delta^- \text{H}-\text{B}$), $\text{H} \cdots \text{H}$ bond length of 2.02 Å. (Figure 1.) A recent neutron diffraction spectra shows that the molecule is composed of linear ($\angle 156$) $\text{N}-\text{H} \cdots \text{H}$ and bent ($\angle 106$) $\text{B}-\text{H} \cdots \text{H}$ bonds.⁸ The hydrogen bonding network makes AB a molecular crystal that undergoes a phase transition from orthorhombic to tetragonal at -40°C .

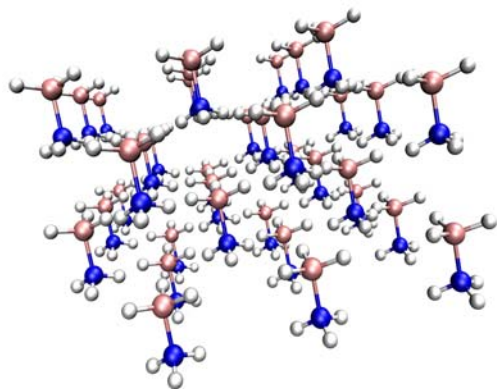


Figure 1. Schematic illustrating network of dihydrogen bonding complex of ammonia borane (NH_3BH_3).

Ammonia borane (borazane) has been examined as a potential hydrogen storage material.⁹⁻¹¹ Upon heating hydrogen is generated from the solid state however, little is known about the mechanism for release of H_2 . At first glance, the dihydrogen bonding feature ($\text{N}-$

$\text{H}^{\delta+} \cdots \delta^- \text{H}-\text{B}$) could lead one to believe that this may be a favorable step towards a bimolecular transition state leading to the formation of molecular hydrogen. However, there has not been an unambiguous test of the reaction mechanism.

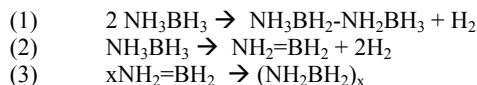
In this work we present spectroscopic experimental studies design to elucidate more about the potential mechanism for H_2 formation from amine borane complexes in the solid state and by catalytic pathways in solution. The solid phase thermal reaction involves a bimolecular dehydrocoupling reaction to yield a new B-N bond, i.e., $\text{HNBH}-\text{H} \cdots \text{HNBH}$ to yield $\text{HNBH}-\text{NBH}$ in contrast to our observations of the catalytic pathway involves the intramolecular abstraction of H-H from a single $\text{H}-\text{NBH}-\text{H}$ molecule to yield $\text{N}=\text{B}$ intermediate.¹²

Experimental

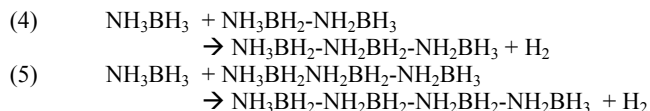
Differential Scanning Calorimetry. DSC analyses were performed using a Netzsch STA 409 TGA/DSC and a Pfeiffer QMS300 MS or a Setaram C80 Calorimeter. In the Netzsch equipment a heated fused silica capillary (200°C) was used to transfer the off gas from the TGA to the MS. The MS uses a standard electron impact ionization detector. The MS scanning rate was 12 seconds for a range of 1 to 100 amu. A thermal ramp of $1^\circ\text{C}/\text{min}$ from room temperature to 200°C using an argon flow of 20 cc/min was used in our analysis.

Results and Discussion.

Elucidation of the mechanistic pathways leading to the formation of hydrogen from Ammonia Borane. We have used a combination of D-labeling and calorimetry experiments to gain insight into the mechanistic pathway leading to the formation of molecular hydrogen from ammonia borane. Currently it is not even known if the reaction proceeds by a unimolecular (eq 1)¹³ or bimolecular pathway (eq 2-3).¹⁴⁻¹⁶



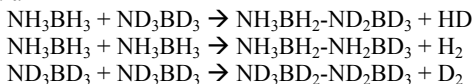
If reaction 1 is the mechanistic pathway then it follows that the dimer would form oligomers through subsequent bimolecular dehydropolymerization pathways (eqs 4-5). This bimolecular pathway involves the BH from one molecule of AB with the NH of another AB molecule to form a new B-N.



Temperature-program desorption mass spectroscopy. H_2 , D_2 and HD formation from a mixture of $\text{NH}_3\text{BH}_3 + \text{ND}_3\text{BD}_3$. In order to differentiate between a bimolecular and unimolecular hydrogen formation pathway deuterium labeled ammonia borane adducts were prepared. A solid state mixture of $\text{NH}_3\text{BH}_3 + \text{ND}_3\text{BD}_3$ (50/50 wt/wt) was prepared by dissolving the each isotopically pure material in THF. Then equal volumes of the THF mixtures were mixed together and the solvent removed under vacuum. The solid mixture was then analyzed by raman spectroscopy to demonstrate that there was no exchange reactions occurring during our mixing procedure leaving us with an intimately mixed solid containing both $\text{NH}_3\text{BH}_3 + \text{ND}_3\text{BD}_3$ (no ND_3BH_3 or NH_3BD_3). There are two different outcomes for gas formation that are expected for a bimolecular and a unimolecular pathway: if the reaction occurs by a bimolecular pathway we should be able to observe a complex statistic mixture of H_2 , D_2 and HD on

the other hand if the reaction proceeds by a unimolecular pathway then we should observe only H_2 and D_2 and no HD should be detected.

Bimolecular



Unimolecular



Ramping the temperature of the 50/50 wt/wt mixture of (NH_3BH_3 + ND_3BD_3) to 200 C generates the formation of all three species, f H_2 , D_2 and HD , with the predominate observed product $HD > H_2 > D_2$.

Calorimetry. *Kinetic Analysis of Hydrogen Loss from Solid State NH_3BH_3 – Isothermal Calorimetry.* The time-dependent behavior of the isothermal DSC curves (Figure 2) shows sigmoidal features indicative of auto catalytic behavior. There appears to be an onset delay before the reaction begins, followed by a rapid evolution of hydrogen reaching a maximum output followed by a rapid decay. These time-dependent traces are characteristic of solid state nucleation and growth kinetic models. Thus, one interpretation of the DSC data suggests that there may be two activated processes, the rate limiting step, a nucleation event, followed by a much more rapid growth, of polymer, until a significant amount of the hydrogen is released and then the reaction slows down again as the starting material is consumed.

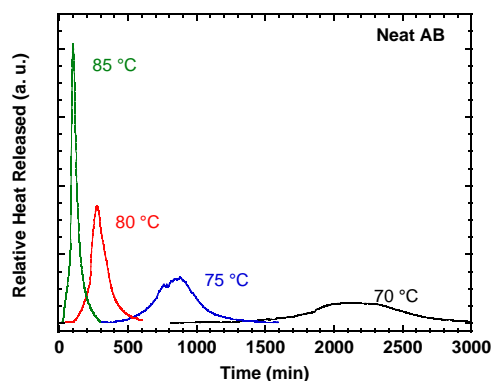


Figure 2. Isothermal DSC curves for the decomposition of ammonia borane as a function of temperature. Sigmoidal shape of curve is indicative of a solid state nucleation and growth kinetic model.

Conclusions

Details of the mechanistic pathway for hydrogen formation will permit the optimization and design of new hydrogen storage materials. This work shows that the loss of hydrogen from solid state AB occurs by an activated process that follows conventional nucleation and growth kinetic models. D- labeling studies strongly suggest that the reaction producing the hydrogen proceeds by a bimolecular pathway and not by a unimolecular pathway as previously believed.

Acknowledgement. The authors wish to acknowledge support from the Laboratory Directed Research and Development Program at the PNNL and the Nano Science and Technology Initiative. This research was performed in part using the Interfacial and Nano Science facility in the William R. Wiley Environmental Molecular

Sciences Laboratory, a national scientific user facility sponsored by the U.S. Department of Energy's Office of Biological and Environmental Research and located at the Pacific Northwest National Laboratory. Pacific Northwest is operated for the Department of Energy by Battelle.

Corresponding author: tom.autrey@pnl.gov

References

- (1) R. F. Service, *Science* **2004**, 305, 958. *Toward a Hydrogen Economy*.
- (2) Scientific American, May **2004**, *Questions about a Hydrogen Economy*.
- (3) National Academy of Engineering, **2004**, The Hydrogen Economy: Opportunities, Costs, Barriers, and R&D Needs.
- (4) American Physical Society, **2004**, *The Hydrogen Initiative*.
- (5) M. Gutowski, T. Autrey, *Prepr. Pap. –Am. Chem. Soc., Div. Fuel Chem.* **49**, 275 (2004).
- (6) T. Autrey, A. Gutowska, L. Li, J. Linehan, M. Gutowski, *Prepr. Pap. –Am. Chem. Soc. Div. Fuel Chem.* **2004**, 49(1), 150.
- (7) Y. Chen, J. L. Fulton J. C. Linehan T. Autrey, *Prepr. Pap. – Am. Chem. Soc. Div. Fuel Chem.* **2004**, 49(2), 972.
- (8) W. T. Klooster, T. F. Koetzle, Per, E. M. Siegbahn, T. B. Richardson, R. H. Crabtree, *J. Am. Chem. Soc.* **1999**, 121, 6337.
- (9) J. Baumann, Dissertation (2003), TU-Bergakademie Freiberg, Germany. The Freiberg group has been investigating NH_3BH_3 as a hydrogen storage material.
- (10) F. Baitalow, J. Baumann, G. Wolf, K. Jaenicke-Rößbler, G. Leitner, *Thermochim Acta* **2002**, 391, 159.
- (11) G. Wolf, J. Baumann, F. Baitalow, F. P. Hoffmann, *Thermochim Acta* **343**, 19 (2000).
- (12) Y. Chen, J. L. Fulton J. C. Linehan T. Autrey. submitted to *J. Am. Chem. Soc.* **2004**.
- (13) C. A. Jaska, K. Temple, A. J. Lough, I. Manners, *J. Am. Chem. Soc.*, **2003**, 125, 9424.
- (14) R. Komm, R. A. Geanangel, R. Liepins, *Inorg. Chem.* **1983**, 22, 1684.
- (15) V. Sit, R. A. Geanangel, W. W. Wendlandt, *Thermochim. Acta* **1987**, 113, 379.
- (16) D. -P. Kim, K. -T. Moon, J. -G. Kho, J. Economy, C. Gervais, F. Babonneau *Poly. Adv. Tech.* **1999**, 10, 702.

CATALYTIC PARTIAL OXIDATION OF METHANE: IS A DISTINCTION BETWEEN DIRECT AND INDIRECT REACTION MECHANISMS MEANINGFUL?

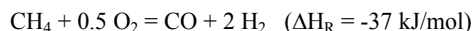
Tengfei Liu, Cynthia Snyder, and Götz Vesper

Chemical Engineering Department
1249 Benedum Hall, University of Pittsburgh
Pittsburgh, PA 15261

Introduction

Catalytic conversion of methane to synthesis gas is a key technology in the petrochemical industry. Its importance is expected to even further increase in coming years due to the increasing significance of natural gas as a feedstock for petrochemical processes. Furthermore, hydrogen production from fossil or biorenewable methane has added interest in this reaction in recent years.

While syngas is currently produced almost exclusively via steam reforming of methane, catalytic partial oxidation of methane (CPOM) has emerged in recent years as a technologically interesting alternative [1]. In CPOM, methane reacts directly with oxygen or air to form CO and H₂ in a one-step reaction:



The reaction is catalyzed by noble metals such as Pt or Rh, and is characterized by extreme reaction temperatures around 1000°C, which results in very high reaction rates and thus extremely short residence times in the millisecond range [2].

The extreme temperatures observed at autothermal conditions arise due to a complex interaction of total and partial oxidation pathways: preferential adsorption of oxygen on the catalyst surface results in a local over-oxidation of the catalyst front edge, which leads to the strongly exothermic total oxidation of parts of the methane feed [3]. While this is detrimental for syngas yields, it also leads to the high reaction temperatures which are thermodynamically necessary to shift the reaction route towards the mildly exothermic partial oxidation of methane.

However, much debate exists in the scientific community whether the initial total oxidation of part of the methane feed is followed by 'true', i.e. direct, partial oxidation or rather by reforming and/or water gas shift reactions in the second part of the catalyst bed. Unfortunately, the extreme reaction conditions as well as the intricate interplay between total oxidation and partial oxidation and/or steam reforming complicate the development of an understanding of the reaction mechanism. Due to the high reaction temperatures and the resulting low catalyst surface coverages, conventional surface science studies are not applicable to this reaction system. Furthermore, due to the extreme temperature gradients of up to 10⁶ K/m on the catalyst, conventional (isothermal) kinetic studies also can not be expected to reveal a complete picture of the reaction mechanism at realistic process conditions. Despite many years of intense research on this reaction, the reaction mechanism for CPOM at high-temperature millisecond contact time conditions is therefore still unresolved.

In the present paper, we report results from a study which allows us to gain better insights into the reaction mechanism of CPOM over Pt catalysts by varying the catalyst length and gas flow rate, and by correlating the obtained syngas yields with temperature profiles measured throughout the catalyst bed at reaction conditions.

Experimental

The experimental setup used for the investigations has been reported previously [5]. The reactor consists of a quartz-glass tube with catalyst and inert-zones, which is then inserted into a stainless steel housing. The reactants (CH₄ and air) are fed with standard mass-

flow controllers and product gases are analyzed with a double-oven gas chromatographic system.

The catalysts were alumina supported Pt catalysts. Extruded alumina monoliths with 400 cpsi and 17 mm diameter were coated with Pt via conventional precipitation from a H₂PtCl₆ solution. After impregnation, the catalysts were dried overnight at room temperature and then calcined at 600°C for 5 hours, followed by reduction in a gas flow of 5 vol% H₂ in N₂ at 500°C for 2 hours. This resulted in a closed metal film on top of the ceramic monolith (see figure 1). Typical weight loadings were ~5 - 6wt%. The length of these catalysts was varied between 2 mm and 10 mm.

A moveable thermocouple allowed for spatial temperature measurements throughout the catalyst as well as the inert zones surrounding the catalyst by means of moveable thermocouples.

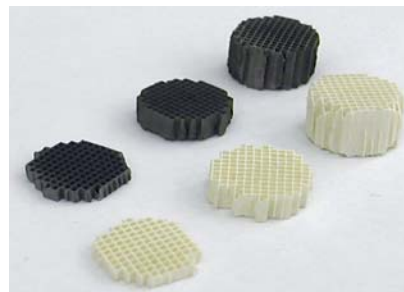


Figure 1. Alumina monoliths with 2 mm, 5 mm, and 10 mm length before and after impregnation with Pt.

Results and Discussion

Figure 2 shows temperature profiles (left graph) along with methane conversions and syngas selectivities (right graph) for a stoichiometric methane-air mixture (CH₄/O₂ = 2.0) at a total inlet gas flow of 4 slm (standard liters per minute) for three different catalyst lengths of 2 mm (squares), 5 mm (circles), and 10 mm (triangles). Gas flow is from left to right, and the vertical lines indicate the beginning of the catalyst (left-most line) as well as the end of the 2 mm, 5 mm, and 10 mm catalysts, respectively.

The temperature profiles already reveal significant difference between the three catalysts: while the temperature profiles in the first 2 mm are identical for all three catalysts, the temperature maximum for the 2 mm catalyst is increased by about 100°C in comparison to the other two catalysts. Most significantly, this temperature maximum is located downstream of the catalyst, i.e. outside the catalyst zone. Apparently, the extremely short residence time of less than 1 ms at these conditions is not sufficient for the catalytic reaction to go to completion, and hence post-catalytic homogeneous reactions occur. This is also reflected in the conversion and selectivities observed in this case (fig. 2, right graph): methane conversion and hydrogen selectivity are below 40%, i.e. much below the conversion and selectivity observed with the longer catalysts. Clearly, the post-catalytic homogeneous reactions are mostly combustion reactions as also indicated by the high maximum temperatures. Most likely, not all oxygen has been consumed in this short catalyst zone and hence leads to homogeneous combustion behind the catalyst. Since H₂ is much more reactive than CO and CH₄, this leads predominantly to water formation and hence to the observed decrease in H₂ selectivity. Since combustion consumes significantly more oxygen than partial oxidation, oxygen becomes the limiting reactant and limits overall methane conversion.

The 5 mm and 10 mm catalysts show identical temperature curves up to the temperature maximum of about 900°C which is located about 4 mm inside the catalyst. However, while the temperature profile for the 5 mm catalyst shows a rather flat, linear

drop following this maximum, the temperature profile for the 10 mm catalyst drops off steeply towards the end of the catalyst zone and then shows the same flat decrease in temperature as for the 5 mm catalyst.

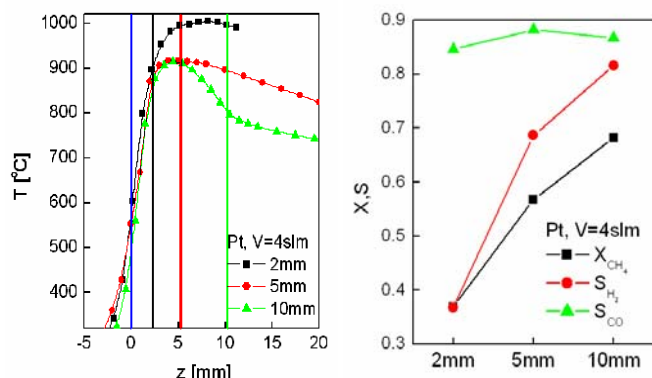


Figure 2. Temperature profiles inside the catalyst (left graph) for a 2 mm (squares), 5mm (circles) and a 10 mm (triangles) long catalyst along with the corresponding values for S_{CO} (triangles), S_{H_2} (circles), and X_{CH_4} (squares) (right graph).

The flat, linear drop in temperature behind the maximum temperature for the 5 mm catalyst can be traced back to heat losses. The temperature maximum is located close to the catalyst end, so that the rather high heat losses from the small laboratory reactor determine temperatures in the inert zones. No indication for post-catalytic reactions can be found in the temperature curve. All oxygen has been consumed over the length of the 5 mm catalyst, so that no post-catalytic combustion can occur. Correspondingly, methane conversion as well as hydrogen selectivity are strongly improved in comparison to the 2 mm catalyst.

In case of the 10 mm catalyst, the steep drop in the catalyst temperatures in the second half of the catalyst is a clear indication for endothermal reactions. The sudden change in the temperature gradient upon transition to the inert zone indicates that these reactions are truly catalytic. The nature of the endothermal reaction becomes apparent from the conversion and selectivity data: both methane conversion and hydrogen selectivity are further increased over the data for the 5 mm catalyst, indicating that steam reforming of methane is occurring in the second half of the 10 mm catalyst.

To probe further contact times and thus get a better temporal resolution for our data, we varied the flow rate through the three catalyst. Gas phase concentrations in the exit gas stream were then plotted against calculated catalyst contact time. The measured temperature profiles allowed us to exclude cases in which post-catalytic homogeneous reactions occur so that any trends observed should be due only to catalytic reactions. Furthermore, based on the temperature profiles it was possible to calculate true contact times rather than space velocities. (Changes in the mole number could not be taken into account but should make for comparatively small corrections only). The resulting data is shown in figure 3.

One can see that contact times in excess of about 2 ms are needed to achieve complete oxygen conversion in this system which is in agreement with our interpretation of the observations with the 2 mm catalyst. Furthermore, the parallel course of the methane and water curves for $\tau > 3$ ms indicates that once all oxygen has been consumed, the catalytic reaction pathway switches to steam reforming. No indication for any water-gas shift reaction can be found.

The change (decrease) in the slope of the hydrogen concentrations around 3 ms indicates that a change in the production rate of hydrogen occurs at this point. Due to postcatalytic homogeneous reactions, we do not have sufficient data at very short contact times to directly identify a reaction mechanism. While the amount of methane and oxygen consumption as well as the amount of hydrogen formed up to this point are in agreement with a true partial oxidation, the steep temperature increase at the catalyst entrance is only consistent with total oxidation, so that a combination of total oxidation followed by steam reforming is more likely.

Finally, the smooth curves for CO and CO_2 as well as the small amount of CO formed after complete oxygen consumption clearly indicate that CO is formed almost exclusively by direct oxidation of methane.

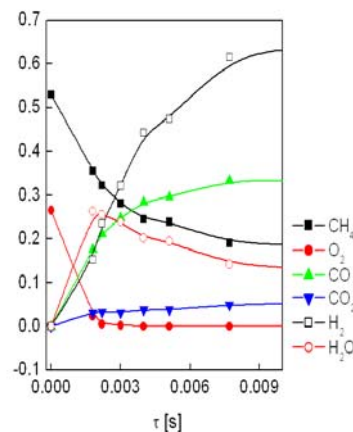


Figure 3. Concentrations of the reactants and main products in CPOM as a function of catalyst residence time.

Conclusions

The results from our investigation of CPOM at high-temperature millisecond contact time conditions shed new light on the reaction mechanism at realistic process conditions. The results indicate that a majority of the hydrogen is formed via steam reforming of methane, while CO is formed almost exclusively by direct oxidation. It appears therefore that the question whether the mechanism underlying CPOM is direct oxidation of methane or indirect oxidation via combustion and steam reforming is not really meaningful and needs to be answered separately for the carbon and the hydrogen pathways.

Future Work. We are currently extending the presented study by conducting detailed kinetic simulations with several published reaction mechanisms to test whether any of these mechanisms are in agreement with our experimental results and to implement necessary improvements.

References

- (1) Prettre, M., C. Eichner, and M. Perrin, *Trans. Faraday Soc.*, **1946**, 43: p. 335.
- (2) Hickman, D.A. and L.D. Schmidt, *Science*, **1993**, 259: p. 343.
- (3) Vesper, G. and J. Frauhammer, *Chemical Engineering Science*, **2000**, 55: p. 2271-2286.
- (4) Friedle, U. and G. Vesper, *Chemical Engineering Science*, **1999**, 54(10): p. 1325-1332.
- (5) Neumann, D., and G. Vesper, *AIChE Journal*, **2004**, in print.

RING OPENING OF METHYLCYCLOHEXANE OVER PLATINUM LOADED ZEOLITES

V. Calemma, A. Carati, C. Flego, R. Giardino, R. Millini

EniTecnologie SpA Via Maritano 26, 20097 San Donato Mil.se,
Milan, Italy

Introduction

The future requirements of reduced emissions for automotive fuels, to be used in the next generation engines are increasing the interest of the refining industry in new processes for the production of cleaner fuels. Besides a reduction of the sulfur content, a specification under scrutiny for the diesel fuel is the aromatic compounds content. Other than having a direct impact on the emission of polyaromatic hydrocarbons (PAH), the hydrogenation of aromatic structures leads to improvements of several characteristics of interest such as density, cetane number and boiling point. Commercial catalyst and processes are available for the saturation of aromatic rings [1]. However, a much higher improvement of diesel fuel quality is possible, if the aromatic saturation is followed by the ring opening of naphthenic compounds to produce alkanes without formation of lower molecular weight compounds.

The object of the present communication is to present the main results of a study carried out at bench scale level where the behavior of three platinum loaded catalysts towards the conversion of methyl cyclohexane has been investigated.

Experimental

Zeolites used in the present study were H-ZSM-5 (Si/Al=37), a dealluminated H-mordenite (Si/Al=50) and H-ZSM-23 (Si/Al=50). H-ZSM-5 and H-ZSM-23 were prepared according the recipes described in [2, 3]. Platinum was loaded on previously ground zeolites, by impregnation with an $\text{H}_2\text{PtCl}_6/\text{HCl}/\text{CH}_3\text{COOH}$ solution. Details of procedure are reported elsewhere [4]. In each case the platinum content was 1%.

The acidity distribution of the catalysts was determined by pyridine adsorption/desorption FT-IR spectroscopic method (mod. 2000, PE). After evacuation at 500°C, the wafer of pure material was contacted with pyridine at 200°C for 1 hour. Desorption at increasing temperature (200-500°C) was performed and the corresponding infrared (IR) spectra monitored, as described in [5].

The hydrocracking tests with methylcyclohexane (MCH) were carried out in a continuous bench scale fixed bed reactor operated down flow mode (height of the catalyst bed: 100 mm; internal diameter: 15 mm; catalyst particle size: 0.85-0.4 mm). The range of the operating conditions was: 220-320 °C, 2.0 MPa total pressure, H_2/MCH molar ratio of 10 and WHSV: 1-3 h^{-1} . After loading, the catalysts were activated by heating at 623 K, flowing hydrogen at 2.0 MPa. Reaction products were analyzed by on line GC. Identification of GC peaks was accomplished by GC-MS analysis.

Results and Discussion

Conversion of MCH on Pt/zeolites led to 30 compounds deriving from isomerization and hydrocracking reactions. The identified products can be lumped in three main groups. The first one made up of ethyl-cyclopentane (EtCP) and dimethyl-cyclopentanes (DiMeCPs), the second formed by normal and iso-ephanes (n/iso-C7) and the third constituted by open chain alkanes with less than 7 carbon atoms that is cracking products. Furthermore, significant yields of C_8 compounds made up of ethyl-cyclohexane (EtCH), dimethyl-cyclohexanes (DiMeCHs) and tri methyl cyclopentanes were obtained at high conversion levels (>60-70%).

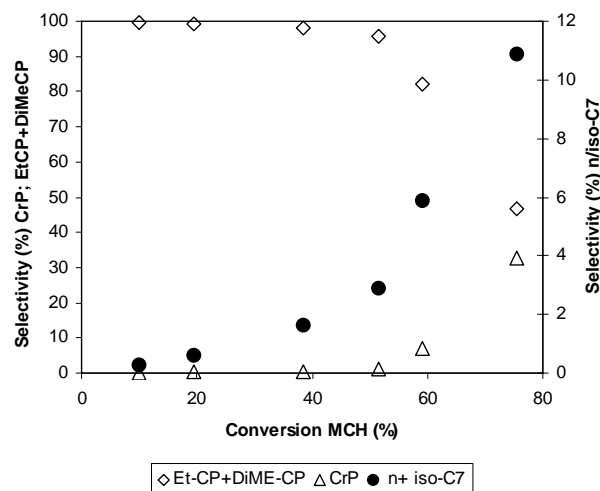


Figure 1. Conversion of MCH on Pt/mordenite. First-order selectivity plot for reaction products.

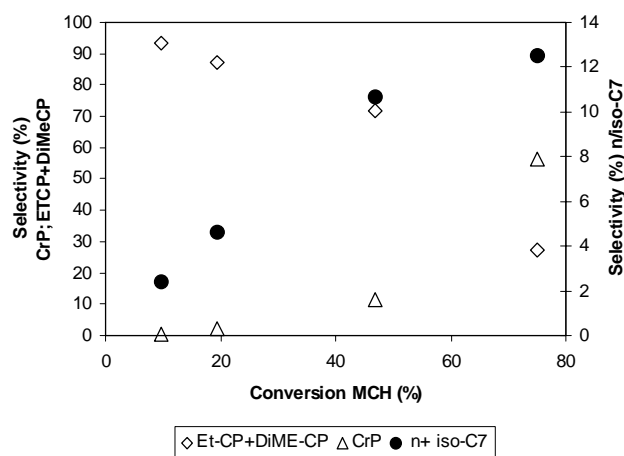


Figure 2. Conversion of MCH on Pt/ZSM-5. First-order selectivity plot for reaction products.

For a given reaction, a general method to discriminate between the primary products (i.e. those formed directly from the reacting substrate) and those of higher rank (i.e. those formed through consecutive reactions of an intermediate product) is to plot the selectivity of the products (molar yield/conversion) against the conversion of the feed. By extrapolating the resulting lines in the plots to zero conversion, the primary products show positive intercepts on the y-axis, whereas the non primary products display a zero intercept. The method, described in detail elsewhere [6], has a more general applicability and allows to establish the rank of the non primary products as well. Figures 1, 2 and 3 show the results of this procedure with the catalysts here investigated.

In the case of Pt/H-mordenite system, the data shows that the primary products of MCH conversion are DiMeCPs and EtCP, which further react to give n/iso-C7. The hydrocracking products (CrP) are non primary products formed by consecutive reaction of normal and iso-paraffins C7. Formation of EtCP and DiMeCPs can be explained in terms of classical mechanism of bifunctional catalysis via protonated cyclopropane (PCP) intermediate [7].

The selectivity plots and close inspection of reaction products suggest the network shown in Figure 4.

The evolution of the products in the case of Pt/ZSM-5 and Pt/ZSM-23 is qualitatively similar but displays significant differences as for the selectivity for primary products. With Pt/ZSM-5 catalyst, the selectivity for EtCP+DiMeCP at the lower bound of conversion is lower. However, the selectivity value at vanishing conversion of the products, still indicate that they are the primary products of MCH conversion (i.e. of isomerization followed by ring contraction). Differently, the data concerning the Pt/ZSM-23 show an EtCP+DiMeCP selectivity value at zero conversion significantly lower than 100 while the n/iso-C7 selectivity shows a positive intercept. This fact implies the presence of a reaction pathway which leads directly to the formation of n/iso-C7 by conversion of MCH. However, it should be stressed that a true primary product is the results of the first elementary step of the reaction and what, is named primary product on the basis of the analytical data does not necessarily mirror what happens in the catalyst. In this regards, the products identified are those that after reaction on the catalyst surface diffuse from the particle catalyst to the main fluid stream. If part of primary product, undergoes to a second elementary reaction step before “leaving” the catalyst, a situation similar to the one displayed by the Pt/ZSM-23 system would be observed.

The acid sites are mainly of Brønsted type (i.e. 100-200 $\mu\text{mol/g}$ with respect to 40-50 $\mu\text{mol/g}$ for the Lewis type) for all the catalysts. H-ZSM-23 based catalyst shows the largest amount of Brønsted sites, preferentially of medium and high acid strength. In Pt/H-ZSM-5 the acid strength distribution is similar to that of Pt/H-ZSM-23, while the number is halves. The Brønsted acid sites in H-mordenite based catalyst show distribution in the range of acid strength from weak to strong (Table 1).

Table 1. Acidity Distribution in the 1% Pt Loaded Zeolites

Strength	H-ZSM-5		H-mordenite		H-ZSM-23	
	Lewis	Brønsted	Lewis	Brønsted	Lewis	Brønsted
weak	22	11	5	43	4	17
medium	1	38	2	52	9	82
strong	0	52	0	30	0	93
very strong	27	10	39	11	26	0

The performances in hydrocracking of MCH are clearly influenced by the acid strength of the Brønsted active sites. Strong and very strong acid sites (e.g. in Pt/H-ZSM-23) favor β -scission rates of alkyl carbenium and consequent formation in our case of products deriving from breaking of C-C bond (n/iso-C7, CrP), while the primary products are favored in the presence of an acid distribution shifted towards medium-weak strength (e.g. in Pt/H-mordenite).

By contrast with this influence on selectivity, there was not found a direct relation between total density of acid sites and conversion of MCH. In our case the activity was mordenite>ZSM-5>ZSM-23 being the conversion of MCH (T: 280 °C; P: 20 atm, WHSV: 1 h⁻¹) 63%, 46% and 35% respectively.

Clearly, the situation is more complex and the activity does not simply depend on the concentration and strength of acid sites. A factor which surely plays an important role in determining the activity and selectivity of a catalyst is its pore structure. The presence of large pores makes easier the diffusion of both reactants and products so minimizing secondary reactions. In accordance with this line of reasoning both activity and selectivity for EtCP+DiMeCP follows the same order of the Constraint Index [8] of zeolites used during our study (mordenite: 0.5; ZSM-5: 7.3; ZSM-23: 10.6).

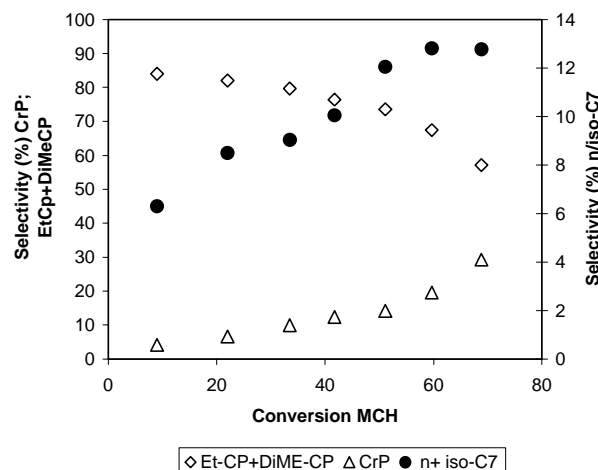


Figure 3. Conversion of MCH on Pt/ZSM-23. First-order selectivity plot for reaction products.

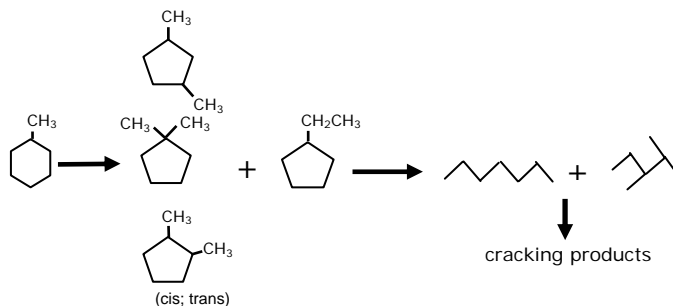


Figure 4. Observed reaction network for MCH hydroconversion in the presence of Pt/zeolite.

Conclusions

The hydroconversion of MCH on different platinum loaded zeolites (H-mordenite, H-ZSM-5 and H-ZSM-23) was investigated. Evolution of the system was rationalized in terms of a reaction network, where the conversion of MCH proceeds via isomerization and ring contraction leading to EtCP+DiMeCP as primary products. Subsequently, the primary products undergo to ring opening reaction, with formation of iso- and n-heptane. The latter, further react leading to the formation of lower molecular weight n-alkanes and iso-alkanes.

The changes in activity and selectivity were shown to be qualitatively linked to the acidity and pore structure of zeolites.

References

- 1) B.H. Reesink, M. Vaarkamp, -M. Chi, B.A. Duijndam, NPRA Meeting AM-00-22, San Antonio, TX, 2000.
- 2) C.J. Plank, E.J. Rosinski, A.B. Schwartz, GB Pat. 1.402.981, Assigned to Mobil
- 3) S. Ernst in: “Verified Syntheses of Zeolitic Materials”, H. Robson Ed., Elsevier, (2001) pag. 217.
- 4) V. Calemme, S. Peratello, C. Perego S. Pavoni, S. Guanziroli US Pat. 6,544,407, Assigned to Agip Petroli and EniTecnologie, 2003.
- 5) C. Flego, I. Kiricsi, C. Perego, G. Bellussi, *Catal. Lett.*, 35 (1995) 125
- 6) N.A. Bhole, M.T. Klein, K.B. Bischoff *Ind. Eng. Chem. Res.* 29 (1990) 313
- 7) J.A. Martens, P.A. Jacobs, J. Weitkamp, *Appl. Catal.*, 20 (1986), 239
- 8) S.I. Zones, T.V. Harris, *Microporous Mesoporous Mater.* 35-36, (1999), 31

PYROLYTIC EVALUATION OF TOBACCO SPECIFIC NITROSAMINE FORMATION FROM BURLEY TOBACCO

B.E. Waymack¹, R.M. Gray², and J.H. Smith¹

¹ Philip Morris USA Research Center, 4210 Commerce Road,
Richmond, VA 23234.

² Quantum Resources, c/o Philip Morris USA Research Center,
4201 Commerce Road, Richmond, VA 23234.

Introduction

The purpose of this work is to investigate the origin and possible means of reducing tobacco specific nitrosamines (TSNA) in cigarette smoke. TSNA in cigarette smoke has been the subject of significant research over the last few decades as noted in a recent review by Baker [1]. TSNA are considered to be undesirable constituents and there has been a general effort to reduce TSNA in tobacco/smoke, most notable in burley tobacco, which typically has higher levels of TSNA [2]. In general, TSNA in smoke have been proposed to come from vaporization of endogenous TSNA in the tobacco that form during the curing process(es) in the leaf [1,3,4,5]. However, there has been evidence of smoke formation mechanisms other than vaporization, namely pyro-synthesis [6,7]. To follow the process of TSNA formation during curing and treatment tobacco, we have developed a method for correlating smoke TSNA yields with yields determined by pyrolysis of tobacco materials. Using this pyrolysis approach, we have evaluated the proposed precursors for TSNA, as well as attempting to develop methods for reducing the TSNA yield in cigarette smoke. TSNA precursors in tobacco are believed to be tobacco alkaloids and nitrate and nitrite [1,8].

Experimental

Pyrolysis Procedure. Endogenous tobacco TSNA levels were determined from an aqueous ammonium acetate extraction of the tobacco filler and subsequent LC/MS analysis for TSNA. The smoke TSNA levels were determined from a standard FTC (Federal Trade Commission) smoking protocol using a fiber glass filter pad to trap condensable materials (referred to as total particulate matter or TPM) followed by extraction of the pad and LC/MS/MS analysis.

The pyrolysis experiments were performed under two sets of conditions. The standard pyrolysis procedure involves sliding a cigarette section (without filter) or plug of tobacco filler, or boat of ground tobacco (1 mm particle size), which was contained in a 10 mm ID quartz tube, into a preheated gold reflection tube furnace at 400 °C and holding for 5 min. Initial sample weights of 300-700 mg were used. The tube was constantly flushed by helium at a flow rate of 1700 cc/min. Total particulate matter (TPM) was trapped using the fiber glass filter pad in a holder attached to the exit of the quartz tube about 120 mm from the furnace exit. Pad breakthrough for TPM and TSNA was determined to be insignificant based on analysis of a second inline filter pad. Material that condensed on the quartz tube between the furnace and the filter pad was included with the TPM on the filter pad for aqueous ammonium acetate extraction and subsequent TSNA analysis by LC/MS/MS. The four TSNA determined were: N'-Nitrosornicotine (NNN), 4-methylnitrosamino-1-3-pyridyl-1-

butanone (NNK), N'-Nitrosoanabasine (NAT), and N'-Nitrosoanatabine (NAB).

A second set of pyrolysis conditions were used to investigate TSNA formation/evolution. Selected samples were heated at a constant rate of 30 °C/min and TPM pads changed about every 20 °C to determine the temperature evolution profile of the TSNA. Selected samples were also pyrolyzed at a set of fixed furnace temperatures from 250 - 600 °C to determine if preset pyrolysis temperatures had a significant effect on TSNA yields. The residence time of the gas in the hot zone was calculated to be about 0.1 second. Selected samples were also tested in the standard 400 °C furnace under a gas flow of 5% or 10% O₂ in helium as well as under 0.4% NO in helium to determine if these gases had a significant effect on the yield of TSNA.

Tobacco Materials. Tobacco samples consisted of a Kentucky reference 2R4F blend and selected burley tobacco samples from the 2002 - 2004 crop years. A sample of 2R4F and two of the burley samples were pyrolyzed after the standard endogenous filler TSNA extraction procedure to determine if any TSNA are 'bound', and not extractable with the solvents used.

Precursor Materials. Precursor materials consisted of nicotine (99+% from Acros Chemicals), nicotine tartrate (99%), nornicotine (99%) and anabasine (90%), all from Sigma-Aldrich Chemicals; mixed with either KNO₃ or KNO₂ (certified A.C.S. from Fisher Scientific) and Avicel microcrystalline cellulose (ash content < 0.008% from FMC Corp.) powder in a water slurry and then vacuum dried at 35 °C before pyrolysis. Target levels of about 2-2.5% of the alkaloid and about 2-4% of nitrate/nitrite on cellulose were used. These reflect nicotine contents of typical tobaccos [9] and gave an excess molar amount of nitrate/nitrite compared to the alkaloid. The nicotine content of the burley tobacco samples in this study ranged from approximately 2 to 4 %.

Results and Discussion

TSNA Smoke and Endogenous Levels. Figure 1 shows the chemical structure of the four TSNA studied here and the possible precursor alkaloids from which they could be derived via nitrosation. The pathway for nicotine to form NNK and NNN is complicated. This figure is shown to illustrate the chemical structures and not to imply the definitive pathways of formation.

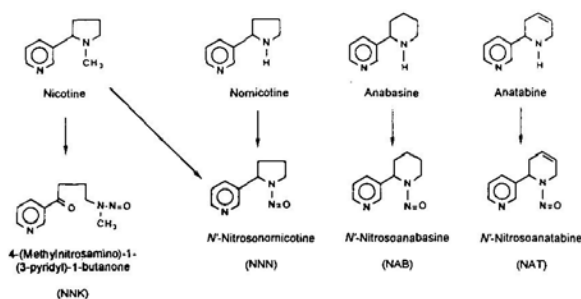


Figure 1. Tobacco alkaloids and TSNA [1]

The primary objective of this study was to determine if TSNA yields from pyrolysis of burley tobacco correlate with, and therefore provide a method for predicting, smoke TSNA yields. It could then be used as a means for studying the TSNA formation during curing/storage and possibly lead to ways to reduce them. The secondary objective was to use pyrolysis to investigate the mechanisms of TSNA formation and evolution. Are TSNA pyro-

synthesized during smoking and to what extent? And are any of the TSNA bound in the filler and pyro-released during smoking? Hopefully these results will lead to understanding their formation and eventually a means by which to reduce or minimize them in smoke.

When smoke TSNA yields are compared with the corresponding TSNA endogenous levels in the filler, one would expect to see an increasing smoke yield with increasing endogenous filler levels. Data from a set of 2002 burley samples showed nearly constant smoke yields over a range of a factor of more than three in endogenous filler levels of TSNA. This data is shown in Figure 2.

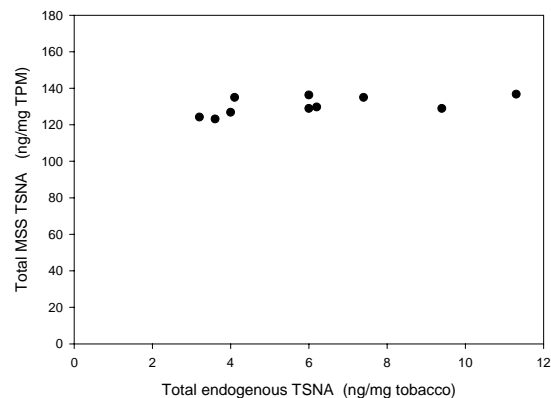


Figure 2. Comparison of endogenous TSNA levels to cigarette smoke TSNA yields for 2002 Burley samples

The data implies more than just transfer of endogenous TSNA to mainstream smoke (MSS). It is likely explained by pyro-synthesis. Pyro-synthesis could explain the reported higher 'transfer efficiency' of endogenous TSNA into MSS for burley tobaccos [2].

Pyrolysis Yields versus Endogenous Levels for Burley. To better determine the extent to which each TSNA is formed by pyro-synthesis, the pyrolysis yields were compared with the endogenous yields per gram of tobacco for 2002-2003 burley samples. NNN and NAT (the major TSNA from burley) seemed to converge to a point where pyrolysis yields approximately equaled endogenous levels, even though for most samples, pyrolysis yields exceeded endogenous yields. For NAB, the pyrolysis yields were always much higher than the endogenous levels, indicating a greater propensity for pyrosynthesis during heating. NNK also always produced a higher pyrolytic yield than the endogenous level.

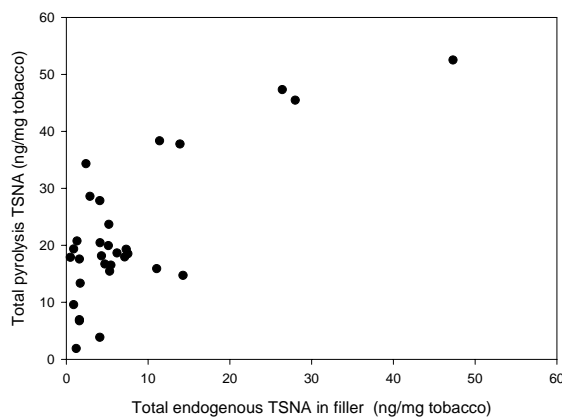


Figure 3. Comparison of pyrolytic TSNA yields and endogenous TSNA levels for Burley tobacco samples

The data for combined total TSNA for pyrolysis versus endogenous is shown in Figures 3. A diagonal line across the graph would represent a one-to-one correspondence of pyrolytic yield to endogenous levels. Some points lie on the line, which indicate equal pyrolysis and endogenous levels. In most cases, these samples had significantly more pyrolytic TSNA than endogenous TSNA.

Pyrolysis Yields versus MS Smoke Yields. Figure 4a shows how pyrolysis results correlate with smoking results for the burley tobacco samples. This figure shows the total TSNA yields for pyrolysis (ng/mg tobacco) and MS smoke (ng/mg TPM) for the burley samples. The linear regression correlation fitted to this data is 0.89. For the individual TSNA, the fitted linear correlations went through the origin and had slopes of 0.15 - 0.18. This suggests that pyrolysis may be a direct method for predicting smoke results. Since approximately 15% of tobacco is converted into TPM during smoking (as well as the pyrolysis experiments of this study), it is not surprising that the correlation between ng/mg of tobacco from pyrolysis and ng/mg of TPM from smoking would be roughly the same value. There are some differences in TPM between different types of tobacco.

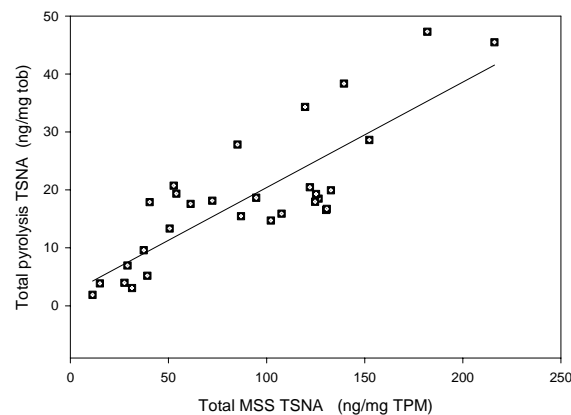


Figure 4a. Comparison of TSNA yields for pyrolysis and smoking

NNK has a tighter correlation when compared to the more abundant NNN and NAT, as is shown in Figure 4b. A possible explanation of this result is the inherent variability in pyrosynthesis (which occurs significantly in many samples for NNN and NAT) compared to the smaller variability of pyro-release of pre-formed levels; which we believe is more dominate for NNK.

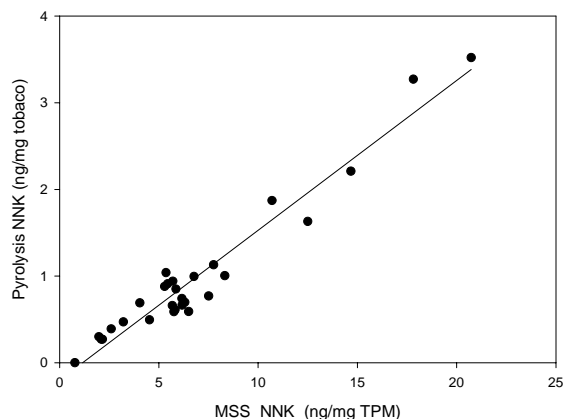


Figure 4b. Comparison of NNK yields for pyrolysis and smoking

Table 1 compares the yields of TSNA from pyrolysis of 2R4F blend tobacco, per mg of tobacco and per mg of TPM, for cigarette rods and ground tobacco filler with TSNA yields from cigarette smoke per mg of TPM. When compared on a per TPM basis, the pyrolysis yields and the smoking yields show good agreement. This indicates we should be able to use the pyrolysis method to follow potential smoke yields through tobacco curing and processing. Using cigarette rods or ground filler did not seem to make a significant difference.

Table 1. Comparison of TSNA Yields from Pyrolysis and Smoking for 2R4F Blend Tobacco

2R4F blend	NNN ng/mg	NNK ng/mg	NAT ng/mg	NAB ng/mg	TSNA ng/mg
Pyrolysis Cigarette rod per tobacco wt.	2.34 ±0.10	2.17 ± 0.21	1.77 ± 0.17	0.27 ± 0.02	6.55 ± 0.50
Pyrolysis Ground filler per tobacco wt.	2.58 ± 0.3	2.24 ± 0.06	2.18 ± 0.06	0.27 ± 0.02	7.27 ± 0.45
Pyrolysis Cigarette rod per TPM	15.76 ± 1.26	14.63 ± 1.66	11.97 ± 1.03	1.80 ± 0.12	44.16 ± 4.07
Pyrolysis Ground filler per TPM	16.54 ± 2.31	14.32 ± 0.53	13.98 ± 0.46	1.75 ± 0.11	46.59 ± 3.41
Cigarette Smoke per TPM	14.4 - 16.0	12.6 - 14.1	12.1 - 12.3	1.47 - 1.52	42.1 - 43.1

Effects of Pyrolysis Conditions. To determine the temperature at which TSNA evolve from tobacco, two burley samples were heated at a rate of 30 °C/min with the filter pads changed at 20 °C increments to determine temperature dependence of TSNA evolution. The results are shown in Figure 5. Samples of high (14 ng/mg) and low (5 ng/mg) endogenous TSNA burley gave similar results for total TSNA yield at slow heating rate (30°C/min up to 400°C), which were consistent with the 400 °C higher heating rate experiments (heating rate ~ 200-300 °C/min when

using pre-set 400 °C furnace). However, the total yields at 30 °C/min were slightly less (about 15-20%) than at the higher heating rate (200-300 °C/min). A slight heating rate dependence suggests residence time in the solid matrix may allow more time for precursors to react with other species or pre-formed TSNA to decompose. TSNA evolve over the same general range of about 150–300 °C, whether we are observing primarily vaporization or pyro-synthesis.

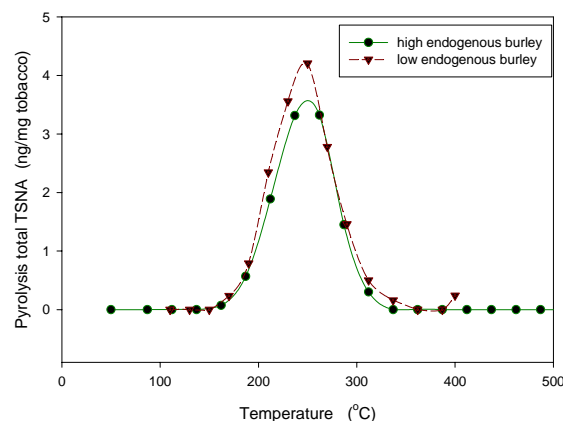


Figure 5. Evolution of TSNA from Burley Tobacco at a heating rate of 30 °C/min

Figure 6 shows the temperature evolution for the four individual TSNA. NNN and NAT, which are the primary TSNA from burley, show a slightly lower peak temperature of evolution than the NNK and NAB. The slightly higher temperature evolution for NNK and NAB we believe are consistent with their greater likelihood of pyro-synthesis and pyro-release.

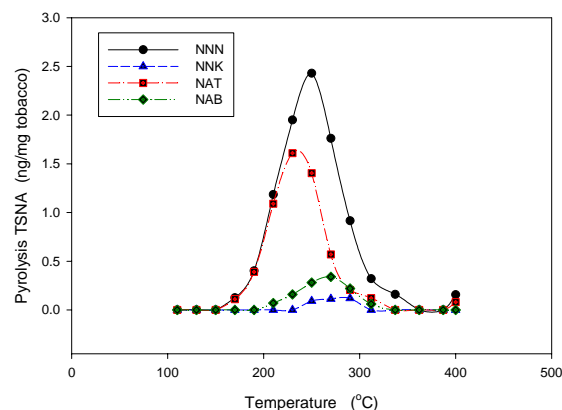


Figure 6. Evolution of individual TSNA from high endogenous burley at a heating rate of 30 °C/min

TSNA yields were determined for the reference 2R4F blend tobacco over a range of pre-set furnace temperatures from 250 – 600 °C. TPM production from tobacco peaks from 300-400 °C and ends by about 500 °C. Above 500 °C the tobacco continues to lose weight by formation of non-TPM volatiles (CO, CO₂, CH₄, H₂ etc.). Pre-set fixed pyrolysis temperatures between 300 and 500 °C gave approximately the same TSNA yield, within experimental error. Yields at 250 °C were about 85% of the maximum yield and

600 °C gave about 65% of the maximum yield. Below 300 °C, not all of the TSNA are evolved, and above 500 °C, one observes the apparent decomposition of TSNA in the gas stream, even at short residence times. Temperatures of at least 250 – 300 °C are required to evolve all TSNA from the tobacco on a time scale of minutes. For a very long time scale, TSNA evolution and decomposition may occur at lower temperatures.

Oxygen Studies. Table 2 summarizes the results from pyrolysis of 2R4F tobacco in helium and in 5 and 10 % O₂ in helium. It is concluded from these experiments that the presence of O₂ did not significantly alter TSNA yields.

Table 2. Effects of O₂ during 400 °C Pyrolysis - Relative TSNA Yields from 2R4F Normalized to Helium Control

Carrier Gas	NNN	NNK	NAT	NAB	Total TSNA
Helium	1.0	1.0	1.0	1.0	1.0 ± 0.13
5 % O ₂	0.91	0.90	0.85	0.90	0.89 ± 0.09
10 % O ₂	0.85	0.97	0.94	1.03	0.92 ± 0.10

Extraction of Tobacco and Bound TSNA. A sample of 2R4F blend tobacco and two burley tobaccos (high and low endogenous TSNA levels) were extracted with aqueous ammonium acetate (used for determining the endogenous TSNA levels) and then were pyrolyzed after extraction. TSNA yields were normalized back to the controls per unit weight of un-extracted tobacco. This data is summarized in Table 3. The major finding here is that a significant portion of the NNK remains after extraction, whereas the other three TSNA are essentially completely removed. If the endogenous level are added to the pyro-release NNK yields for the two extracted burley samples, they essentially add up to the total pyrolytic yields for the starting tobacco; suggesting pyro-release as a major mechanism. This would suggest, at least for these burley samples, that NNK is primarily pre-formed, but a significant amount is bound (un-extractable) in the tobacco matrix and only released upon heating. Consequently NNK differs distinctly in this regard from the other three TSNA as being pyro-released rather than pyro-synthesized.

Table 3. Relative Ratio of Pyrolysis TSNA Yield from Aqueous Ammonium Acetate Extracted Tobacco Normalized to Control Starting Tobacco Weight Basis

sample	NNN	NNK	NAT	NAB
2R4F	0.05	0.72	0.04	ND
low burley	0.01	0.72	0.01	ND
high burley	0.03	0.58	0.04	0.03

ND = not detected

Precursors for Pyro-synthesis. Figure 7 shows TSNA yields from 2004 burley samples with different nitrate fertilizer levels. A general increase in TSNA is observed with increasing nitrate fertilizer level. The nitrate/nitrite in tobacco is considered the main source of nitrosation or nitrosating agent.

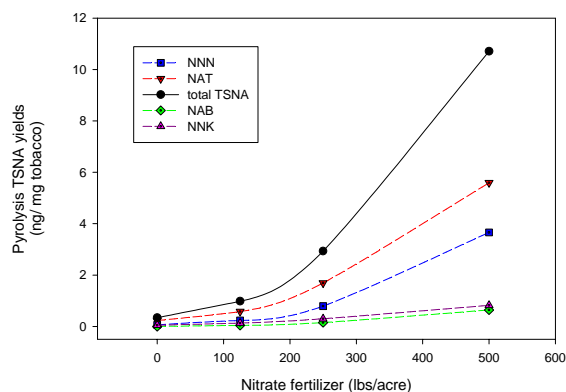


Figure 7. Effect of nitrate fertilizer levels on TSNA yields at 400 °C

NO Studies. Is the nitrosation of the tobacco alkaloids during heating or smoking (i.e., during pyro-synthesis) a gas/solid or gas phase reaction? To answer that question, the decomposition of nitrate or nitrite salts and their ability to produce NO_x in the temperature range where TSNA are formed must be determined. TG/MS (thermogravimetry /mass spectrometer) experiments were performed with KNO₂ and KNO₃ mixed with cellulose powder (Avicel). During the major decomposition of nitrate and nitrite, NO is released (a small amount of NO₂ with nitrate). For the pure salts, the decomposition does not begin until the temperature is about 500 – 600 °C. In the presence of a biomass matrix (cellulose), nitrate salts decompose over the range of 300 – 350 °C (in conjunction with the cellulose); while nitrite salts in the presence of cellulose decompose at temperatures as low as 220 °C. This would suggest that nitrite could decompose in the presence of an organic matrix over the same temperature range as TSNA are formed or evolved.

The effects of NO in the gas stream were studied to determine if TSNA yields increased, and if so, at what temperatures. It has been reported that TSNA can form presumably from reaction with NO_x and alkaloids on the TPM filter pad during smoking [10]. Table 4 shows data with and without 0.4% NO under our pyrolysis conditions of 400 °C for 5 minutes for 2R4F blend and a burley sample. The concentration of NO used is a considerably higher than tobacco would encounter in a cigarette under smoking conditions (about 0.02-0.04%). Oxides of nitrogen in fresh smoke are essentially all NO [11]. From Table 4 it appears that NO did not produce an increase in TSNA yields.

Table 4. TSNA Yields from 400 °C Pyrolysis of 2R4F and a Burley Sample with/without 0.4 % NO – Normalized to Helium Control

Sample	NNN	NNK	NAT	NAB	Total TSNA
2R4F helium	1.0 ± 0.15	1.0 ± 0.06	1.0 ± 0.10	1.0 ± 0.12	1.0 ± 0.11
2R4F 0.4% NO	0.89 ± 0.08	0.87 ± 0.06	1.11 ± 0.17	1.02 ± 0.16	0.96 ± 0.10
burley helium	1.0 ± 0.07	1.0 ± 0.07	1.0 ± 0.08	1.0 ± 0.06	1.0 ± 0.07
burley 0.4%NO	0.75 ± 0.04	0.84 ± 0.04	0.82 ± 0.03	0.79 ± 0.09	0.79 ± 0.04

These preliminary results suggest that solid/liquid phase pyro-synthesis reactions are more likely the mechanism of pyro-synthetic TSNA in smoke than gas/solid reactions. At low heating rates there is more residence time for gas/solid reactions, whereas at higher heating rates, the pyrolysis reactions occur too fast for interaction with NO at the temperatures of TSNA evolution. The heating rates during cigarette smoking can be as high as 500 °C/sec during puffing [12]. A small effect of heating rate on pyrolysis in helium (30 °C/min compared to 200-300 °C/min) was seen - an apparent decrease in TSNA yield of about 15-20 % at the slower heating rate. However, this is a small difference for pyrolysis experiments, and suggests that heating rate is not a critical factor in understanding TSNA evolution, even though heating rates equal to cigarette puffing conditions have not been investigated in this study.

Alkaloid and Nitrate/Nitrite Precursor Studies. Samples of tobacco alkaloids with KNO₃ and KNO₂ on a cellulose substrate were pyrolyzed using the fixed temperature 400 °C pyrolysis method. Samples were made from nicotine (N), nicotine tartrate (NT), nornicotine (NN) and anabasine (AB), mixed with either KNO₃ or KNO₂ and Avicel microcrystalline cellulose powder. The results are summarized in Table 5. These preliminary studies show that it is possible to pyro-synthesize NNN and NNK from nicotine, but the relative amounts and ratios depend on whether the nicotine was in its un-protonated form or a salt. Un-protonated nicotine favored NNK and nicotine tartrate favored NNN. NNN and NAB can pyro-synthesize from nornicotine and anabasine, respectively, when in the presence of nitrite or nitrate. Yields were much higher in the presence of nitrite. These conversion yields would more than account for TSNA yields from the tobacco.

Table 5 Relative Conversion of Tobacco Alkaloids to TSNA by Pyrolysis at 400 °C on a Cellulose Matrix with added KNO₂ and KNO₃

2.5 % alkaloid excess NO ₃ /NO ₂	Conversion efficiency to NNN (%)	Conversion to NNK (%)	Conversion to NAB (%)
NT + NO ₃	0.58	0.007	
NT + NO ₂	0.02	0.04	
N + NO ₃	0.0008	0.001	
N + NO ₂	0.08	0.19	
NN + NO ₃	0.05		
NN + NO ₂	2.94		
AB + NO ₃			0.08
AB + NO ₂			5.51

Conclusions

Smoking and pyrolysis results are consistent. Higher yields of TSNA have been measured than can be accounted for by endogenous levels for many burley samples indicating that pyro-synthesis/pyro-release during heating/smoking of tobacco can be a significant source of TSNA. Monitoring the endogenous TSNA levels in tobacco during curing/aging may not give a reliable indication of potential smoke deliveries from the tobacco at that point in the curing/aging process. Total TSNA yield is proportional to endogenous plus available pyrosynthesis and pyro-release.

TSNAs evolve primarily over the temperature range of 150 – 300 °C from tobacco. NNK and NAB peak at slightly higher

temperatures, consistent with other observations that they are more likely to be pyro-synthesized or pyro-released. However, they usually account for only a small portion of the total TSNA in burley tobacco. NNN and NAT can be pyro-synthesized, or depending upon curing, be essentially be released through a vaporization process. NAB appears to be significantly pyrosynthesized in all samples we have observed. A significant portion of NNK may be bound in the filler matrix and not accounted for by extraction methods. Hence, apparent pyro-synthesis of NNK is likely pyro-release of pre-formed NNK (or precursor) bound in the tobacco cell wall material.

Pyrolysis in 10 % O₂ did not significantly alter the TSNA yields. Therefore, pyrolysis in an inert atmosphere should be sufficient for correlating with smoke. Pyrolysis in 0.4% NO at 400 °C did not increase TSNA yields, suggesting that a gas/solid pyrosynthesis reaction is not likely the mechanism in a cigarette.

Pyrolysis of tobacco alkaloids with nitrite and nitrate, in a cellulose matrix, yielded TSNA. Nicotine yielded NNN and NNK; relative yields depended on whether it was in a salt form or not. Nornicotine and anabasine yielded NNN and NAB, respectively; with much greater yields in the presence of nitrite.

Acknowledgements. The authors would like to thank Diane Gee and Joseph Banyasz for their support and Shirley Ha and Michael Maher for technical assistance, analytical data and the burley tobacco samples.

References

- [1] R.R. Baker, in *Tobacco-Production, Chemistry and Technology*, edited by D.L. Davis and M.T. Nielsen, Blackwell Science, (1999) p.425-426 and references therein.
- [2] S. d'Andres, R. Boudoux, J-M. Renoud and J. Zuber, *Beitr. Tabakforsch. Int.* Vol. 20 No. 5 (2003) 331-339.
- [3] K.D. Brunnemann and D. Hoffmann, *Rec. Adv. Tob. Sci.*, 17 (1991) 71-112.
- [4] A. Wiernik, A. Christakopoulos, L. Johansson and I. Wahlberg, *Rec. Adv. Tob. Sci.*, 21 (1995) 39-80.
- [5] S. Fisher, B. Spiegelhalder, J. Eisenbarth and R. Preussmann, *Carcinogenesis*, 11 (1990) 723-730.
- [6] D. Hoffmann, M. Dong and S.S. Hecht, *J. Natl. Cancer Inst.*, 58 (1977) 1841-1844.
- [7] J.D. Adams, S.J. Lee and N. Vinchkoski, *Cancer Lett.*, 17 (1983) 336-346.
- [8] L.L. Parsons, M.S. Smith, J.L. Hamilton and C.T. Mackown, *Tob. Sci.*, 30 (1986) 100-103.
- [9] M.F. Borgerding, T.A. Perfetti and S. Ralapati, in *Analytical Determination of Nicotine and Related Compounds and Their Metabolites*, edited by J.W. Gorrod and P. Jacob, 1999, p.285, 314, 318-319, 327-329, 344-351.
- [10] W.S. Caldwell and J.M. Conner, *J. Assoc. Off. Anal. Chem.*, 73 (1990) 5-31.
- [11] M. Parish, Philip Morris USA, *unpublished data*, (2004).
- [12] R.R. Baker, *High Temp. Sci.*, 7 (1975) 236-247.

LOW TEMPERATURE BENZO[A]PYRENE YIELDS FROM TOBACCO COMPONENTS

T. E. McGrath¹, Y. Bezjak², A. P. Brown², S. A. Haut¹
and W. G. Chan¹

¹ Philip Morris USA Research Center, 4201 Commerce Road,
Richmond VA 23234.

² Lancaster Laboratories, c/o Philip Morris USA Research Center,
4201 Commerce Rd, Richmond VA 23234.

Introduction

The formation of polycyclic aromatic hydrocarbons (PAHs) from tobacco has been extensively studied over the past four decades. Benzo[a]pyrene (B[a]P), a 5-ring PAH is a well known carcinogen and as such its formation has received much attention. Of the many individual component classes in tobacco (alkaloids, reducing sugars, cellulosic materials, long-chain hydrocarbon waxes, amino acids, proteins, etc.), lipophilic tobacco components such as phytosterols, saturated aliphatic hydrocarbons, and terpenoid compounds were believed to be the major precursors of PAHs formed from a burning cigarette(1). Most of the data put forth in the literature to support the proposed precursor pools was obtained from pyrolysis experiments carried out on tobacco, selective tobacco extracts, and individual tobacco components at temperatures > 700 °C and at gas phase residence times on the order of seconds to 10's of seconds(2-4). The recently reported formation of 2 to 5 ring PAHs at pyrolysis temperatures below 600 °C in µg/g quantities from tobacco and carbohydrate samples such as cellulose, glucose, and sucrose highlights a low temperature mechanism for PAH formation(5,6). In this study a number of solvent extracted tobaccos and individual tobacco components such as sterols, long-chain hydrocarbons, fatty acids, carbohydrates and polyphenols have been pyrolyzed at 600 °C in an effort to identify low temperature B[a]P precursors. The yield of B[a]P obtained per gram of sample pyrolyzed has been normalized to the amount of each component present in tobacco. The B[a]P yield from a mixture of selected lipophilic and cell wall components in tobacco has also been investigated.

Experimental

Materials

Tobacco Samples. Bright (flue cured) lamina and bright lamina extracted with hexane, ethyl acetate and water were ground (10 - 150 µm particle size) prior to pyrolysis. The hexane and ethyl acetate extracted samples were prepared using a Soxhlet extraction setup. The water extracted sample was prepared by extracting a sample of bright lamina packed in a column with a continuous stream of deionized water totaling 20 L at room temperature. The extraction process in hexane, ethyl acetate and water leads to about a 4, 16 and 50% reduction in sample weight, respectively.

Fatty Acids, Sterols, Isoprenoids, and Polyphenols. Oleic acid (99+%), linoleic acid(99%), stigmasterol (93%), chlorogenic acid, (95+%) solanesol (90+% from tobacco leaves) and cholesterol (99+%) were purchased from Sigma-Aldrich. Linolenic acid (90%, remainder linoleic acid) and D(+)-proline (99+%) were purchased from Acros. A lipid mixture of oleic acid (1mg/g), linoleic acid(2 mg/g), linolenic acid (3.5 mg/g), stigmasterol (0.8 mg/g), chlorogenic acid (8 mg/g) and solanesol (15 mg/g) was prepared in methanol and added to a mixture of carbohydrates and lignin.

Model Tobacco Cell Wall Components. Avicel cellulose, xylan from birch wood, pectin from citrus fruits, and hydrolytic lignin were used as model tobacco cell wall components. The Avicel cellulose sample was obtained from FCI and is a microcrystalline purified and depolymerized alpha-cellulose derived from fibrous plants (Avicel

PH-102, ash content < 0.007%). The birchwood xylan (≥95% xylose) sample was obtained from Fluka. The lignin and pectin (galacturonic and methoxy content of 81% and 8.6%) samples were obtained from Sigma-Aldrich. D-glucose, used as a model for reducing sugars in tobacco, was obtained from Acros and is 99+% reagent grade.

A mixture of cellulose, hemicellulose, pectin, glucose, and lignin was prepared with the following component ratios of 1:1:1:1:0.3, respectively. The resulting mixture is designated as Carbo-Lig Mix throughout the rest of the text. The major cation present in the pectin, hemicellulose and lignin samples, determined by ICP-MS, was sodium. The samples also contained smaller amounts of Ca.

Pyrolysis Setup. The pyrolysis setup used has been described previously(6). A 2.5 cm i.d. quartz tube is placed inside a 30 cm long heated Carbolite furnace having an isothermal length of ca. 7 cm at a temperature of 600 °C. Helium was used as the carrier gas at a flow rate of 120 cm³/min. The residence time of gas phase pyrolysis products in the isothermal section of the reactor was calculated to be approximately 4 s at a furnace temperature of 600 °C. A fiber-glass filter placed in a housing assembly immediately at the end of the quartz tube on the exit side of the furnace was used to collect the product tar condensate. The temperature of the sample in the heated quartz tube was measured using a chromel/alumel (K type) thermocouple. The thermocouple was also used to transport the ceramic boat containing the samples to and from the heated isothermal region of the quartz tube.

A sample of tobacco or model tobacco compound to be pyrolyzed was placed in a ceramic boat that initially rested in an unheated section of the quartz tube outside of the heated furnace. A trap assembly for the pyrolysis tar was placed on the exit side of the furnace. After the furnace had reached the desired set temperature, for example, 600 °C, the sample was pushed into the isothermal region in the furnace and pyrolyzed for a total of 10 minutes. The boat was then pulled back to the unheated section of the quartz tube and the remaining solid residue was allowed to cool to room temperature. The fiber-glass filter was removed, placed in an amber screw capped vial, and the trap assembly was washed with methanol. The washings from the housing assembly were added to the sample vial. A total solvent level of 5 mL of methanol was used and the vial was left to stir overnight on a shaker. At the end of each run, the quartz tube was cleaned in air at a temperature of 650 °C.

The extracted tar samples were analyzed by GC-MS using an Agilent 6890 GC equipped with an Agilent 5973 quadrupole MSD analyzer operating in the selected ion mode (SIM). Although this paper only focuses on the formation of B[a]P other PAHs such as acenaphthylene, fluorene, phenanthrene, anthracene, fluoranthene, pyrene, benz[a]anthracene, chrysene, benzo[k]fluoranthene, benzo[b]fluoranthene, indeno[1,2,3,-cd]pyrene, and benzo[ghi]perylene were also monitored. The yield of B[a]P was calculated using a calibration curve obtained from the analysis of standard solutions of B[a]P ranging from 10 to 1000 ng/ml. The yield of B[a]P reported is the average of three independent experiments.

Results and Discussion

Solvent Extracted Tobacco Samples. Solvents with varying polarities were used to extract the bright tobacco lamina sample and the yields of B[a]P formed at 600 °C in He from the resulting extracted lamina are given in Figure 1.

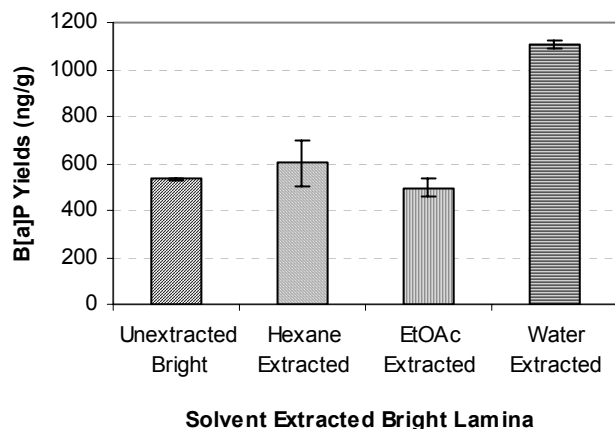


Figure 1. B[a]P yields from solvent extracted bright tobacco pyrolyzed at 600 °C in He. (120 ml/min flow rate, 600 °C/min heating rate, 10 min).

Extraction of bright tobacco lamina with either hexane or ethyl acetate did not significantly affect the yield B[a]P formed compared to an unextracted control. The result suggests that non-polar tobacco components such as long-chain hydrocarbons and fatty acids which are readily removed by these solvents are not significant low temperature B[a]P precursors in tobacco. The water extracted sample gave a 107% increase in B[a]P. Extraction with water removes alkaloids, amino acids, pectin, sugars, organic acids, and phenolics from the original lamina. The water extraction process appears to remove non-forming low temperature PAH precursors but concentrates instead (on a per unit weight basis) PAH forming precursors.

Individual Tobacco Components. The yields of B[a]P obtained from the pyrolysis of 11 individual components at 600 °C in He for a total heating time of 10 min are give in Table 1. B[a]P yields reported in Table 1 for some of the cell wall components are similar to those previously reported for the same components at a slightly higher pyrolysis temperature of 650 °C(7). Stigmasterol, cellulose, hemicellulose, glucose and lignin gave the highest yields of B[a]P on a ng/g basis. The formation of B[a]P from the pyrolysis of fatty acids appears to increase with the number of double bonds in the structure, i.e. oleic < linoleic < linolenic acid. When the yields of B[a]P are normalized to the amount of each component in tobacco, cellulose, hemicellulose, glucose and lignin contributed significantly to B[a]P yields.

Carbohydrate + Lignin Mixture. A carbohydrate + lignin mixture (Carbo-Lig mix) was pyrolyzed by itself, as well as in the presence of an amino acid (proline) and a mixture of tobacco lipid components. D(+)-proline (0.4% w/w) was physically mixed with the Carbo-Lig mix and the lipid mixture was added as a methanol solution. The amounts of amino acid and lipids added are proportional with the amount of each component present in bright tobacco(1). As shown in Fig. 2, neither the addition of an amino acid (at 0.4% w/w) nor doubling the concentration of lipids (oleic acid, linoleic acid, linolenic acid, stigmasterol, chlorogenic acid, and solanesol) significantly affected the yield of B[a]P formed from the Carbo-Lig mix.

Table 1. 600 °C Pyrolysis B[a]P Yields for Tobacco Components

Tobacco Component	B[a]P Yields at 600 °C	^a Norm. B[a]P Yield
Sterols	(ng/g)	(ng/g)
Stigmasterol ^b (~ 0.8 mg/g)	1200	0.9
Isoprenoid		
Solanesol (20-40 mg/g)	ND	
Fatty Acids		
Oleic acid (~ 1 mg/g)	80	0.08
Linoleic acid (~ 2 mg/g)	175	0.35
Linolenic acid (~ 4 mg/g)	335	1.34
Carbohydrates		
Cellulose (~ 100 mg/g)	970	60
Hemicellulose (~ 100 mg/g)	976	60
Pectin (~ 100 mg/g)	100	10
Glucose (~ 140 mg/g)	786	98
Polyphenols		
Lignin (~ 40 mg/g)	934	18
Chlorogenic acid (~ 8 mg/g)	ND	

ND = not detected.

a = BaP yield normalized to the amount of the component present in bright tobacco

b = approximate amounts reported to be present in bright tobacco

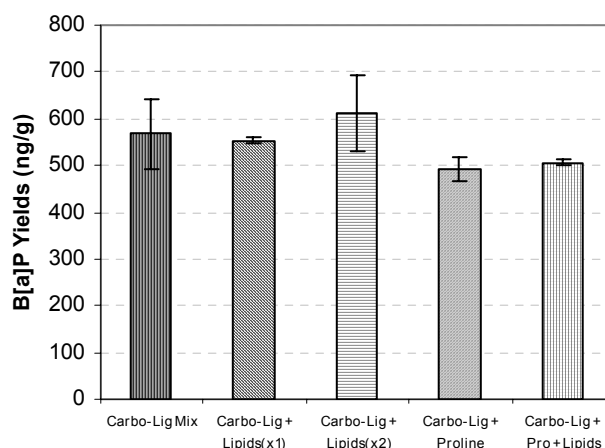


Figure 2. Effect of Proline (0.4% w/w) and Lipids on the yield of B[a]P from the 600 °C pyrolysis of a carbohydrate + lignin mixture. (120 ml/min flow rate, 600 °C/min heating rate, 10 min).

Conclusions

Extraction of bright tobacco lamina with hexane and ethyl acetate removes certain lipophilic components of tobacco but does not lead to a decrease in B[a]P formed. The addition of selected lipids to a carbohydrate-lignin mixture also does not increase B[a]P yields. Extraction with water appears to concentrate B[a]P precursors on a per gram of material basis. From the individual tobacco components pyrolyzed at 600 °C, only the tobacco carbohydrates and cell wall components such as glucose, cellulose, hemicellulose and lignin appear to contribute significantly to the formation of B[a]P.

Acknowledgement. The authors would like to thank Gail Yoss, Littycia Clay and Jennifer Ricketts for their technical assistance.

References

- (1) Chortyk, O. T. and Schlotzhauer W. S., *Beitr. Tabakforsch.*, 7, 3, **1973**, 165–178.
- (2) Rodgman, A. Smith, C. J. and Perfetti, T. A. ,*Human and Experimental Toxicology*, 19, **2000**, 573-595.
- (3) Baker, R. R. and Proctor, C. J., **CORESTA 2001**
- (4) Severson, R. F., Schlotzhauer, W. S., Chortyk, O. T., Arrendale, R. F and Snook, M. E., in *Polynuclear Aromatic Hydrocarbons*, Edited Jones, P. W. and Leber, P. Ann Arbor Science Publishers, Inc., Ann Arbor, MI, **1979**, 277-298.
- (5) McGrath, T. E., Chan, W. G., Hajaligol, M. R., *submitted for publication*, **2004**.
- (6) McGrath, T. E., Chan, W. G., Hajaligol, M. R., *J. Anal. Appl. Pyrol.*, 66, **2003**, 51-70.
- (7) Gilbert, J. A. S. and Lindsey, A. J. ,*Brit. J. Cancer*, 11, **1957**, 398-402.

SEPARATING GAS PHASE FROM SOLID PHASE CHEMISTRY AND IDENTIFYING THE REACTIVE INTERMEDIATES INVOLVED IN THE PYROLYSIS OF BIOMASS CHARS.

Andrew M. Herring, J. Thomas McKinnon, Joshua G. Lee, Ryan A. Pavelka, Matthew S. Kirchner, and Eun-Jae Shin.

Department of Chemical Engineering
Colorado School of Mines
Golden, CO 80401-1887

Introduction

Cellulose is a major component of biomass, along with hemicellulose and lignin, and is a useful model for thermo-chemical conversion of biomass. The conversion of biomass via pyrolysis has important applications in the development of new renewable chemicals and bio-carbons, as well as combustion processes leading to combined heat and power, forest fires and cigarette smoking. Tobacco is a very interesting model biomass for pyrolysis studies, as a lot of the chemistry of the plant is well understood. Obviously the pyrolysis of tobacco involves a huge number of compounds, many of which are unique and the reduction of PAH from the pyrolysis of this biomass is particularly challenging. The process of cellulose, tobacco and the pyrolysis of their chars is still not fully understood despite rapid progress in the last couple of decades.¹⁻³ The influence of metal salts on charring and subsequent pyrolysis has long been known to alter the chemistry of these processes.^{1,4} Metal cations occur naturally in biomass particularly in the hemicellulose, they may also be added to the growing plant in the form of fertilizer. In general inorganic materials in the form of ash are considered a problem that must be mitigated against in the pyrolysis and combustion of biomass.⁵ However, metal cations may be deliberately added to the biomass to alter its pyrolysis chemistry in a favorable way to reduce the formation of polycyclic hydrocarbons, PAH, or in the synthesis of new bio-carbons.⁶

In order to more fully understand the effect of metal doping on cellulose and tobacco pyrolysis chemistry we have doped Avicel cellulose with a series of mono- and di-valent cations. Both main group (for cellulose) and transition metals (for tobacco and cellulose) were chosen in order to probe both the effects of promoting ionic pathways and possible catalytic pathways in the charring and pyrolysis chemistry. We chose to dope cellulose and tobacco with metal acetates as not only is the acetate anion relatively inert but all of these metal acetates decompose below the charring temperature of 375 °C. The chars were characterized primarily by DRIFTS, TGA and NMR. The char structure and pyrolysis chemistry at very short times, several ms was studied by laser pyrolysis molecular beam mass spectroscopy, LP-MBMS.^{7,8} We also sampled the product gases and trapped the free radicals produced using cold and chemical trapping at slightly longer times, several 100 ms. Additional data analysis was performed via multivariate factor analysis, MVFA.⁹

Experimental

Avicel cellulose (5 g) was doped at 1mol% with Na, K, Mg, Ca, Pd, Cu, Co, Ni or Zn (and for Bright or Burley tobacco, Zn, Cu, or Pd) acetates by the incipient wetness technique using aqueous solutions of the as received metal acetates. The doped cellulose samples were dried in an oven at 115 °C overnight pressed into a 1" diameter pellet at 10,000 psi in a Carver press and charred under Ar(g) at 375 °C for ½ h. The same procedure was adopted for tobacco, except that the tobacco was slightly rewetted after oven drying to allow for adhesion of the pellet.

For the DRIFTS experiments the chars were ground in air and placed in a Harrick Scientific, heatable variable atmosphere chamber in a Harrick Scientific Praying Mantis Diffuse Reflectance attachment. The chars were heated under dry He(g) for 10 mins at 400 °C and then cooled to room temperature at which point the DRIFTS was recorded using a Thermo-Nicolet Nexus 670 FT-IR spectrometer equipped with a N_{2(l)} cooled MCT detector. The data was treated with a Kubelka-Munk transformation to enable its quantitative interpretation.

TGA analysis was performed using a Seiko TGA balance, sample size 10 mg at a heating rate of 10 °C min⁻¹ from ambient to 600 °C.

The details of the LP-MBMS experiment have been described previously.⁸ After cooling, the metal doped cellulose chars samples were transferred under inert gas to a He(g) filled chamber. LP-MBMS experiment performed at 6.5 W for 2 s. The first 0.25 s data corresponding to a temperature between 900 and 1000 °C is reported here.

For the cold-trapping experiments the charred pellet was mounted in the center of a N_{2(l)} cooled brass collection cup, ca. 2 mm from the cold surface. The brass collection cup had been previously coated with Diphenyldisulfide to which a known quantity of chlorobenzene had been added as an internal standard. The charred pellet was irradiated with the CO₂ at 13 W whilst being spun through one revolution. A known amount of Chlorobenzene is used as an internal standard. After the experiment, the cold trap is washed with methylene chloride. The methylene chloride extract is filtered and concentrated by evaporation. The concentrated extract is then injected onto a capillary GC column in a HP 5890 series II GC and the species identified using a HP 5971 MSD.

Results and Discussion

The TGA data for doped cellulose is shown in Figure 1. The Avicel char pellet shows a 20% lower weight loss than powdered Avicel char, not shown. We presume this is because there is restricted diffusion of the pyrolysis vapors from the char pellet. There is no difference between powdered tobacco and the tobacco pellets presumably because this substrate is not very compressible.

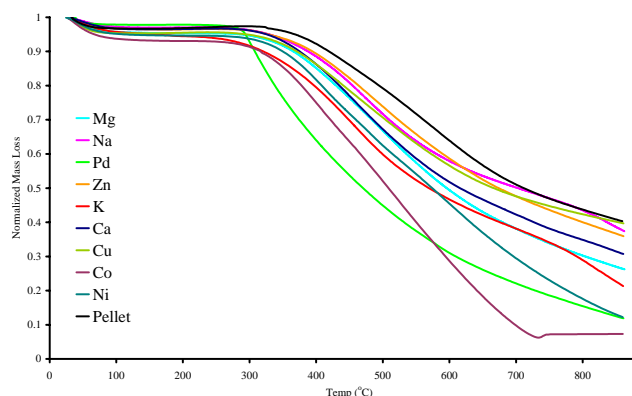


Figure 1. TGA for 1wt% metal acetate doped Avicel charred at 375 °C for 1/2h under Ar(g).

Examination of the data shows that the largest weight losses are observed for Pd and Co doped samples and this is more clearly shown in the MVFA, Figure 2. The onset of weight loss from the Pd doped sample is much earlier than for the other samples indicating that this char is by least stable. The cobalt char is almost only ash by 700 °C. For Bright tobacco, all samples seem to behave similarly. For Burley the Pd doped sample again stands out.

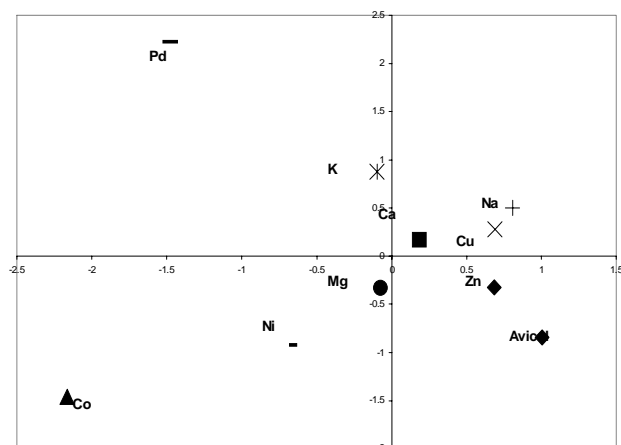


Figure 2. MVFA of 1wt% metal acetate doped Avicel charred at 375 °C for 1/2h under Ar_(g).

The DRIFTS of the doped Bright tobacco chars, Figure 3, show a dramatic change in the ratio of carbonyl to aromatic groups, as defined by the ratio of the band at 1650 to 1400 cm⁻¹ bands. The Zn and Pd chars have very much more carbonyl than the undoped tobacco. Similar results were observed for cellulose and Burley tobacco.

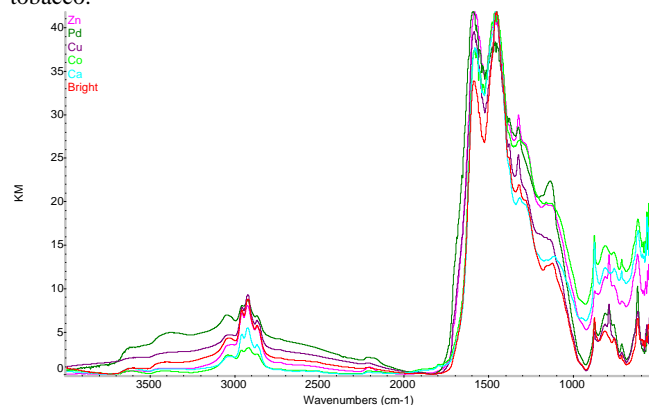


Figure 3. DRIFTS of 1wt% metal acetate Bright tobacco charred at 375 °C for 1/2h under Ar_(g).

The initial slate of reacting molecules formed during pyrolysis may be generated and detected by LP-MBMS. The LP-MBMS of the doped cellulose at 6.5 W shows very little change in the ratios of individual components as the metal is varied. Importantly what does change is the ratio of CO₂, CO, H₂O to small reactive molecules, mostly between m/z 39 and m/z 91 to larger PAH fragments formed during charring. With the most CO₂ formed for Zn doped and the least for Cu and Pd doped chars. Similar results are observed for tobacco chars with the additional observation of a peak at m/z 52, presumed to be cyanogen under certain conditions.

We can arrest the subsequent gas phase reaction at a later time by the use of a cold trap coated with a radical trap such as diphenyl disulfide. With all chars the ratio of the smaller organic molecules is skewed toward two and three ring aromatic as opposed to one ring aromatics in the LP-MBMS experiment. The largest yield of two and three ring aromatics occur for Pd and Cu doped chars. Radicals trapped include H, Me, vinylbenzyl, isopropyl, phenyl and methylnaphthyl. The largest yield of radicals occurs for the Zn doped char.

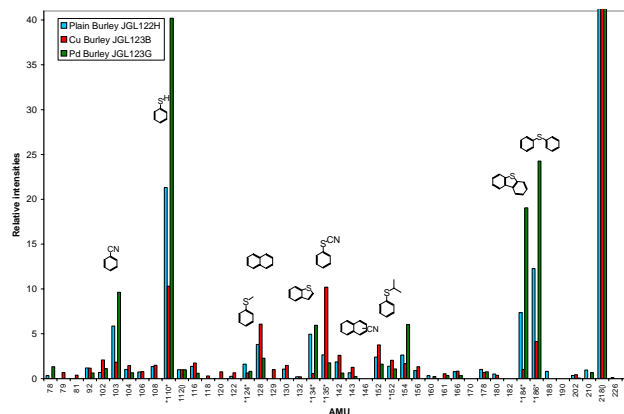


Figure 4. Cold trapped species for Burley and 1wt% Cu and Pd doped Burley charred at 375 °C for 1/2h under Ar_(g).

The tobacco char pyrolyzate is dominated by radicals, for example for Burley, Figure 4, a large amount of H and phenyl are observed as well as all the species seen in the cellulose case. Interestingly we know observe significant amounts of CN and benzo- and naphthyl-nitrile. Cu doped Burley produces the most CN and less radicals than the undoped chars, Pd doped Burley tobacco produces a large amount of H, and phenyl. Exactly the same results are observed for Bright tobacco.

Conclusions

We can begin to correlate char chemistry with the chemistry of the reacting gas phase species. Metal doping appears to perform the primary role of altering the ratio of fixed gasses to reactive intermediates to PAH precursors formed in the char. Clearly Pd doped chars are unique, generally more unstable, but with more residual carbohydrate character. Pd chars give rise to more reactive intermediates than other chars whilst minimizing CN in pyrolysis of tobacco chars. From preliminary work it would appear that Co and Cu may have similar equally profound but different effects.

Acknowledgement. We would like to thank Philip Morris, USA, for support and Dr. Robert Evans for extensive discussions.

References

- (1)Evans, R. J.; Milne, T. A. *Energy & Fuels* 1, (1987), 123.
- (2)Antal Jr., M. J.; Grnli, M. *Ind. Eng. Chem. Res.* 42, (2003), 1619
- (3)Shafizadeh, F. *Journal of Analytical and Applied Pyrolysis* 3, (1982), 283.
- (4)Sekiguchi, Y.; Shafizadeh, F. *Combustion and Flame* 29, (1984), 1267.
- (5)Davidsson, K. O.; Stojkova, B. J.; Pettersson, J. B. C. *Energy Fuels* 16, (2002), 1033
- (6)Herring, A. M.; McKinnon, J. T.; McCloskey, B. D.; Filley, J.; Gneshin, K. W.; Pavelka, R. A.; Kleebe, H.-J.; Aldrich, D. J. *Journal of the American Chemical Society* 125, (2003), 9916
- (7)Herring, A. M.; Thomas McKinnon, J.; Gneshin, K. W.; Pavelka, R.; Petrick, D. E.; McCloskey, B. D.; Filley, J. *Fuel In Press, Corrected Proof*, (2004).
- (8)Herring, A. M.; McKinnon, J. T.; Petrick, D. E.; Gneshin, K. W.; Filley, J.; McCloskey, B. D. *Journal of Analytical and Applied Pyrolysis* 66, (2003), 165.
- (9)Windig, W.; Meuzelaar, H. L. C. *Anal. Chem.* 56, (1984), 2297

TIME-RESOLVED KINETIC ANALYSIS OF THE DIRECT FORMATION OF NITROGEN-CONTAINING AROMATICS FROM BIOMASS CHARS

Robert J. Evans and Mark R. Nimlos

National Renewable Energy Laboratory
Golden, Colorado 80401

Introduction

Empirical models of biomass pyrolysis¹ do not account for possible competing parallel and sequential reactions leading to altered solids and vapor product slates and are therefore unable to fully utilize fundamental understanding of the chemistry in prediction and control of product composition. By use of appropriate experiments, methods of chemical analysis, and data reduction², this gap between empirical studies and molecular details can be closed. In this work, we study the interactions of amino acids and proteins with carbohydrates and the formation of N-aromatics, such as indole derivatives.³ By using time resolved molecular beam mass spectrometry (MBMS) and self-modeling factor analysis⁴, the rates of formation can be followed as a function of reaction conditions.

The fate of nitrogen during pyrolysis or combustion is an important consideration in the utilization of biomass. Nitrogen oxide emissions from biomass combustion are thought to arise primarily from fuel-bound nitrogen⁵ and an understanding of the chemical transformations involving nitrogen may lead to improvements in these emissions. An important source of nitrogen in biomass is proteins and amino acids, which can react catalytically with the carbohydrates by reactions generally characterized as Maillard chemistry⁶. This chemistry produces complex mixtures of products and has been the subject of numerous studies. However, less is known about the role that this chemistry plays in the formation of char. The partitioning of nitrogen into char or gas phase products will be critical towards determining the routes for converting nitrogen from biopolymers into NO_x emissions.

Of particular interest in the char formation are effects due to the Maillard chemistry involving proline. We have shown that proline is more reactive in Maillard chemistry than other amino acids³, which is consistent with literature reports of proline as a catalyst for asymmetric aldol condensations.⁷ Specifically, we would like to investigate how proline affects the maturation of char.

Experimental Techniques

As previously described³, experiments were conducted by heating 250 mg samples of proline mixed with cellulose, pectin and glucose in flowing helium in a tubular reactor held at constant temperatures of either 350 or 550 °C. The gas phase products were measured directly using MBMS and mass spectra were recorded every second over the pyrolysis wave. Factor analysis was performed on the individual mass spectra and self-modeling techniques² were used to resolve four subspectra at each temperature.

Results and Discussion

Figure 1 shows the time resolved profiles at 350 and 550 °C of the total ion count and the four subspectra resolved by the self-modeling factor analysis. The four subspectra were qualitatively the same at each temperature although specific distribution of peaks changed. The first products to evolve (F001) were predominantly water and CO₂. The second products (F004) were Amadori products due to the interaction of proline and glucose and dominated by the aliphatic nitrogen heterocycle, 1-(1'pyrrolidinyl)-2-propanone³. The next products (F003) to evolve were typical carbohydrate products. The final products (F002), shown in Figure 2, are nitrogen aromatics.

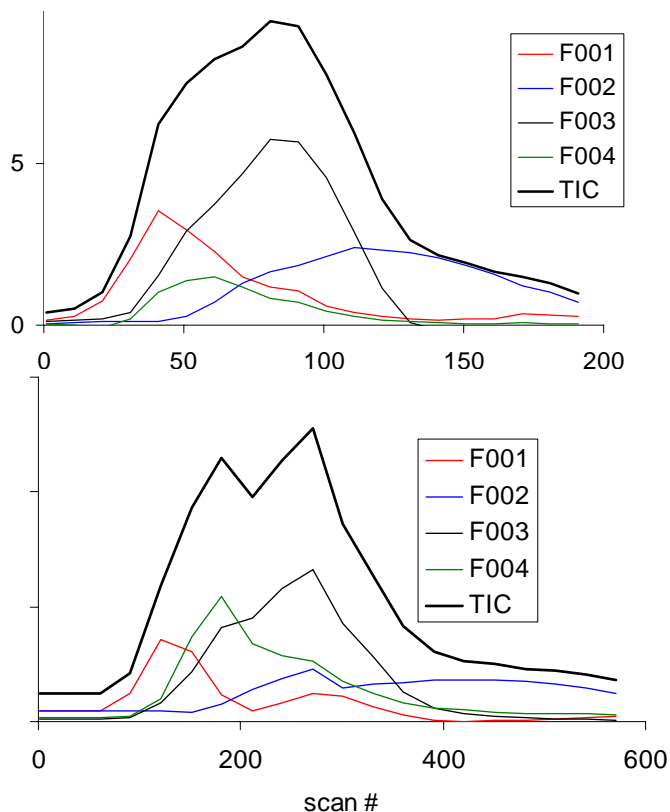


Figure 1. Time-Resolved profiles of sub-spectra identified by factor analysis at 350°C, bottom, and 550°C, top.

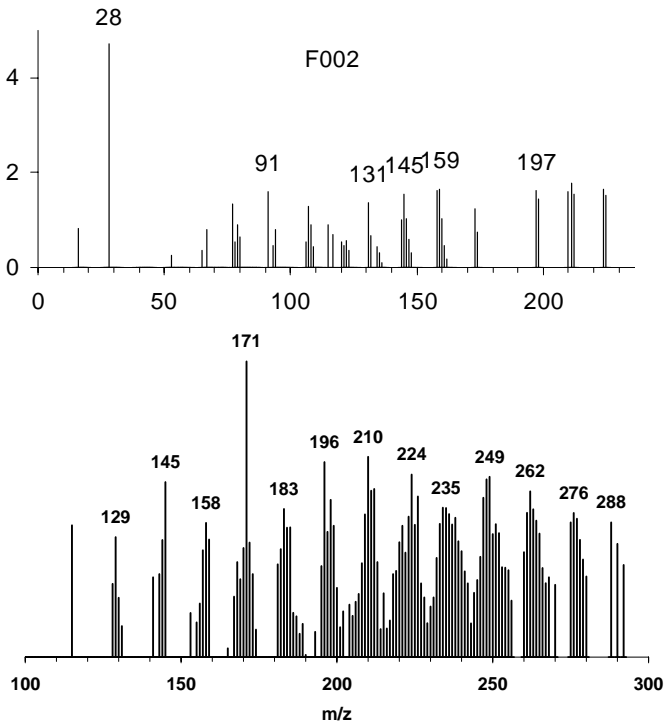


Figure 2. Resolved component spectra for F002, at 350°C, bottom, and 550°C, top.

The F002 component spectrum at 350 °C was higher molecular weight and more complex, but generally reflected the same family of homologous series. The most important is the series of peaks, 131, 145, 159, which are thought to be indole derivatives and representative of the N-aromatics that are formed by the interaction of proline with carbohydrates.

The kinetic profiles of these time-resolved evolution profiles are shown in figure 3 for the F002 factor shown in figure 2.

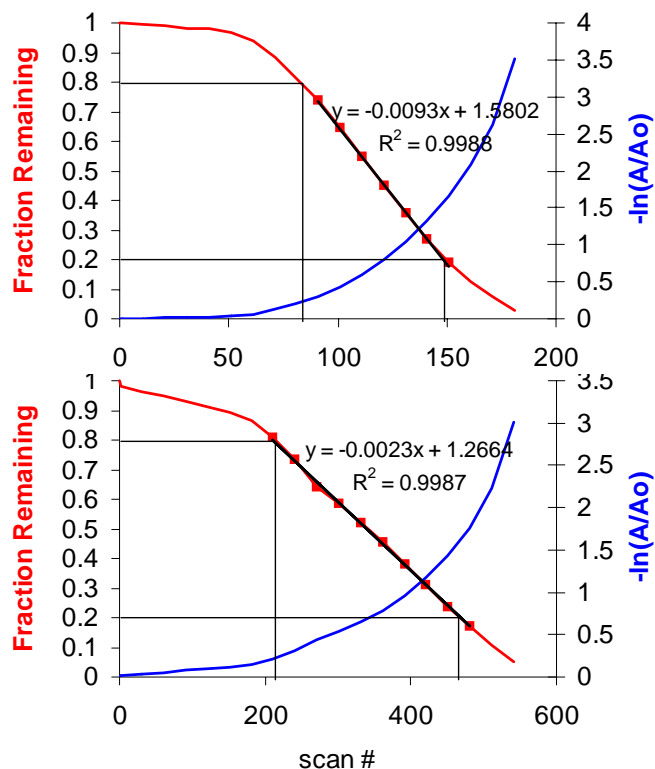


Figure 3. Plot of the integrated evolution profile for F002 as fraction remaining (left axis) and as the first order test, $-\ln(A/A_0)$ (right axis) at 350 °C, top, and 550 °C, bottom.

The fraction remaining is A/A_0 , where A is equal to the amount of starting material remaining as determined indirectly by the volatile matter evolved. The $-\ln(A/A_0)$ will be linear for first order kinetics. In this method the product evolution between 20 and 80% remaining are used to avoid anomalous evolution due to heat and mass transfer. The first two evolving components at both temperatures were linear. For the last two evolving components in figure 1, the $-\ln(A/A_0)$ plots were nonlinear as shown in figure 3 for the nitrogen aromatics (F002 in figure 1). In these cases, the fraction remaining, A/A_0 , was linear which is an indicator of a zero order process. This type of behavior is typical of rate limiting steps due to the effects of catalysis or solid phase reactions.

Conclusions

Related studies of the solid phase over the kinetic regime of interest show that the reactions that occur at low temperature are key to the onset of these N-aromatics when higher temperatures are reached. The formation of volatile aromatics as low as 350 °C is significant. They are accompanied by the accelerated formation of aromatics in the char when proline is present. This has implications

for the char combustion phase when high temperatures can potentially generate even more aromatics from the char.

The use of time-resolved factor analysis and kinetic profiles show behavior consistent with these sequential reaction in the solid phase that give rise to a series of volatile products which show distinct pathways as shown by the relative kinetics of the process.

Acknowledgment

We would like to acknowledge the support of Philip Morris USA, and discussions with Geoffrey Chan and Mohammad R. Hajaligol.

References

1. De Blasi, C., *Fuel*, **1996**, 75(1), 58-66.
2. Shin, E.J.; Nimlos, M.R.; Evans, R. J., *Fuel*, **2001**, 80(12), 1697-1709.
3. Moens, L.; Evans, R. J.; Looker, M. J.; Nimlos, M. R., *Fuel*, **2004**, 83, 1433-1443.
4. Evans, R. J.; Agblevor, F.A.; Chum, H. L.; Wooten, J.B.; Chadwick, D.B.; Baldwin, S.D., Preprint, Div. Fuel Chem. 1991.
5. Brink, A.; Kilpinen, P.; Hupa, M., *Energy Fuels*, **2001**, 15(5), 1094.
6. Labuza, T. P.; Reineccius, G.A.; Monnier, V.M.; O'Brien, J.; Baynes, J. W., ed. *Maillard Reactions in Chemistry, Food and Health*. 1994, Royal Society of Chemistry: Cambridge.
7. Movassaghi, M.; Jacobsen, E.M., *Science*, **2002**, 298(5600), 1904.

AB INITIO MOLECULAR DYNAMICS SIMULATIONS OF β -D-GLUCOSE AND β -D-XYLOSE DEGRADATION MECHANISMS IN ACIDIC AQUEOUS SOLUTION

Xianghong Qian^a, Mark R. Nimlos^b, David K. Johnson^b,
and Michael E. Himmel^b

^aRx-Innovation, Inc., Fort Collins, CO 80525

^bNational Bioenergy Center, National Renewable Energy
Laboratory, Golden, CO 80401

Abstract

Optimizing reaction conditions to minimize sugar loss during pretreatment is one of the primary concerns of the new biorefinery industry. Sugar degradation at different acidity was investigated with first-principles calculation using explicit solvent water molecules included in the simulation. At lower acidity, the rate-limiting step in sugar degradation was found to be the protonation of the hydroxyl groups on the sugar ring. The hydroxyl group with the highest proton affinity will initiate degradation of the sugar molecule leading to formation of the major degradation product. At high acidity, protonation of the hydroxyl groups is rapid. Sugar degradation initiates at multiple hydroxyl groups on the sugar ring leading to multiple products. Furthermore, we found that water molecules play a significant role in the acidic sugar degradation pathways. Firstly, a water molecule competes with the hydroxyl group on the sugar ring for protons. Secondly, water forms hydrogen bonding with the hydroxyl groups on the sugar rings, thus weakening the C-C and C-O bonds (each to a different degree). Note that the reaction pathways could be altered due to the change of the relative stability of the C-C and C-O bonds. Thirdly, sugar hydroxyl hydrogen-bonded water molecules could easily donate or extract a proton from the sugar reaction intermediate, thus terminating the reaction. Indeed, the experimental sugar degradation pathway is complex due to multiple protonation probabilities and the surrounding water structure. Water structure is in turn affected by reaction conditions such as acidity, temperature, the presence of salts and cosolvent, and the flow dynamics of the reactor.

Introduction

Loss of fermentable sugars to acidic degradation is one potential cause of low feedstock yield and high processing cost in lignocellulosic biomass conversion. The decreased yield of β -D-xylose and β -D-glucose during prehydrolysis could significantly affect the economic viability of these processes [1-3]. In order to improve the yields of sugar products, particularly during dilute acid prehydrolysis, understanding the sugar degradation pathways at the molecular level is critical. In addition, acidic sugar degradation products were found to be strongly dependent on the reaction media [4,5]. Previously, we reported acidic β -D-glucose and β -D-xylose degradation mechanisms without considering the reaction media effect [6]. Because there are five and four hydroxyl groups on the β -D-glucose and β -D-xylose molecules, respectively, all probable protonation scenarios of these hydroxyl groups and the ring oxygen were examined. We found that protonation of the C2-OH on β -D-glucose and β -D-xylose, which leads to the formation of major degradation products hydroxymethylfurfural (HMF) and furfural, respectively, was in agreement with the mechanisms proposed earlier by Antal and coworkers [7]. In the current study, the effects of reaction media with explicit water molecules were investigated.

Computational Methods

Ab initio CPMD calculations based on Carr-Parrinello method were employed in this study [8]. Each β -D-glucose and β -D-xylose in our simulation was surrounded by 32 water molecules in a unit cell. In addition, one or more protons were added to the system to mimic the reaction acidity. Periodic boundary conditions were applied. Water density was not normalized to 1 g/cm³ because it is expected to vary with reaction condition. An electron mass of 800 a.u. and a time-step of 0.125 femtosecond (fs) were used in these calculations. The BLYP pseudo-potential with gradient correction was used. Only the energy at the Γ -point was calculated.

Results and Discussion

We have carried out all the probable protonation of the hydroxyl groups and the ring O on the xylose and glucose molecules with explicit solvent water molecules. Here three examples are given to illustrate the effect of reaction media. The first example shows that water actively participates the sugar degradation reaction by extracting a proton from a reaction intermediate. However, water does not alter the reaction pathway. The second example shows that water alters reaction pathway by terminating the ring closure reaction. The third example shows that water structure at higher acidity could change the relative stability of C-C and C-O bond thus changing the sugar degradation mechanism.

Figure 1 shows the β -D-glucose reaction mechanism initiated from C2-OH in aqueous solution with 32 water molecules and a single proton (for degradation). Simulation was carried out at 500K. Water molecules have been removed in order to illustrate the pathways more clearly (only the water molecules involved in the reaction were retained). Sugar degradation was not observed when the proton was initially attached to the hydroxyl groups on the sugar ring. We observed that the proton was transferred to the water molecule after a very short simulation period (< 500 fs). In Figure 1, we show that the protonated C2-OH group (i.e. H₂O) is "pulled away" from the carbon ring initially to a sufficiently large distance (>2 Å) for reaction to occur. We also observed from this simulation that sugar degradation occurs rapidly after the protonated hydroxyl group was separated from the ring carbon C2 atom. Furthermore, a single water molecule

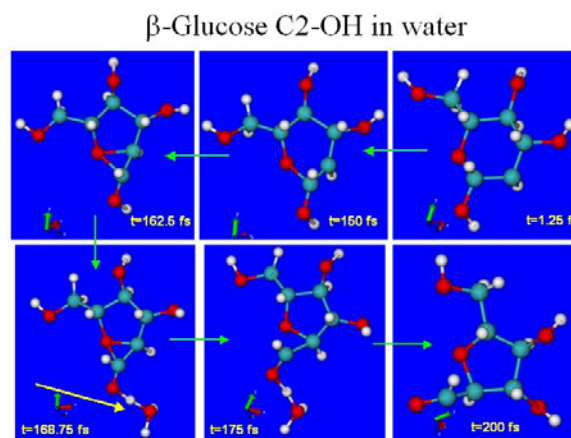


Figure 1. The reaction pathway for β -D-glucose degradation initiated at C2-OH surrounded by 32 water molecules. Solvent water molecules, except one involved in the, reaction were removed from the figure in order to illustrate the pathway more clearly.

participates in the reaction by extracting a proton from the intermediate $\sim\text{C}^+-\text{OH}$ due to hydrogen bond formation between water and the hydroxyl group on the sugar ring. Protonation was found to be the rate-limiting step in very dilute acidic condition.

Figure 2 exhibits the β -D-glucose degradation pathway initiated at the C3-OH. From this figure, it can be seen that the reaction in water is drastically different from that in vacuum [6]. In vacuum, the rearrangement of the carbon cation after the departure of the protonated hydroxyl group leads to the formation of a five-membered ring which could polymerize to form other non-cellulosic materials, including those observed experimentally [9]. With explicit water, the C1-C2 carbon-carbon bond was elongated and eventually broken after the formation of C3^+ carbon cation. Due to the presence of C1-OH hydrogen bonded water molecule, a proton was extracted to form the CHO end group. A C=C double bond was also formed between the C2 (anion) and C3 (cation) carbon atoms, thus eliminating the possibility of 5-member ring closure, as in the C2-OH protonation case, and the corresponding vacuum case. It is shown in Figure 2

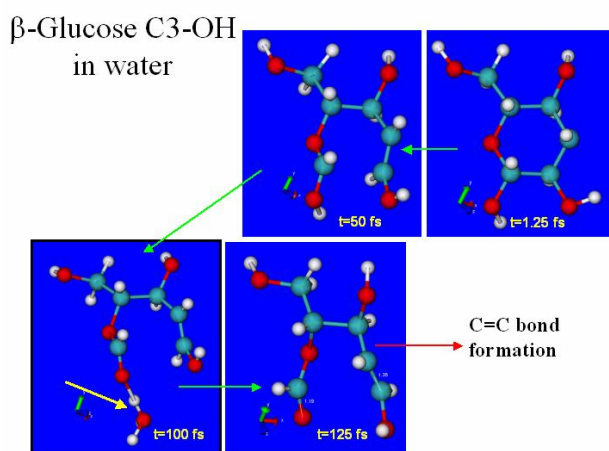


Figure 2. Reaction pathway for β -D-glucose degradation initiated at C3-OH surrounded by 32 water molecules. Solvent water molecules except one involved in reaction were removed in the figure in order to illustrate the pathway more clearly.

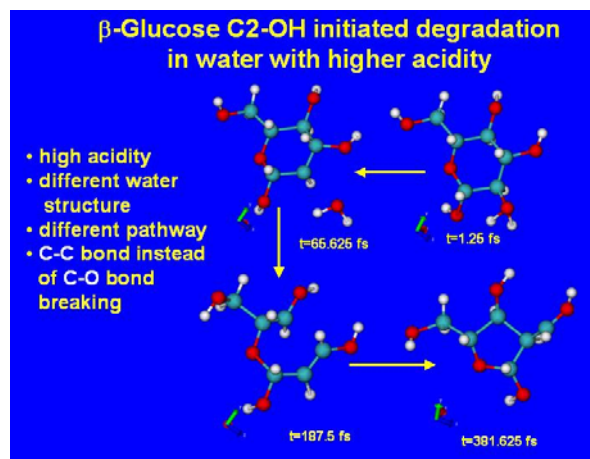


Figure 3. C2-OH initiated glucose degradation in water with higher acidity

that water structure plays a significant role in sugar degradation pathways due to hydrogen bonding interaction between water and the sugar molecules. Water readily accepts and donates a proton depending on the specific reaction condition.

Figure 3 shows β -D-glucose degradation at higher acidity. This time, the β -D-glucose molecule was surrounded by 32 water molecules and 4 protons in each unit cell. These simulation results show that protonation is no longer the rate-limiting step. In addition, a different reaction pathway was observed at higher acidity than that of the lower acidity case, where the C3-C4 bond breaks after C2^+ cation formation. At lower acidity and in vacuum, the O5-C1 bond breaks to form the O5-C2 bond. The reason for such a different mechanism is most likely due to the hydrogen bonding interaction between the solvent water molecule and the hydroxyl groups and the ring oxygen on the sugar molecule. Since the bonding energies for C-C and C-O single bonds are 348 and 360 kJ/mol, respectively, and very close to each other, it is thus possible to break either one of these bonds. Hydrogen bonding interaction weakens the C-C and C-O bonds (each to a different degree) and could well upset the relative stability of the C-C and C-O bonds, thus altering the reaction pathway as shown in Figure 3.

Acknowledgement. The U.S. Department of Energy Office of The Biomass Program supported this work. Portions of this work were done under subcontract No. ACO-4-33101-01 from the National Renewable Energy Laboratory.

References

1. Wyman, C.E.; Bain, R.L.; Hinman, N.D.; Stevens, D.J. *Renewable Energy: Sources for Fuels and Electricity*, Island Press: Washington, D. C., 1993.
2. Sheehan, J.J. Bioconversion for Production of Renewable Transportation Fuels in the United States: A Strategic Perspective. In *Enzymatic Conversion of Biomass for Fuels Production*. Himmel, M.E.; Baker, J.O.; Overend, R.P., Eds., Vol. 566, American Chemical Society: Washington, D.C., 1994; pp. 1-52.
3. Bergeron, P. Bioethanol Market Forces. In *Handbook on Bioethanol*. Wyman, C.E., Ed., Taylor & Francis: Washington, D.C., 1996; pp. 179-195.
4. Torget, R.W.; Kim, J.S.; Lee, Y.Y. (2000), *Ind. Eng. Chem. Res.* 39, 2817-2825.
5. Lee, Y.Y.; Kim, J.-S.; Xiang, D.Q.; Kim, T.-H. (2001), *Enhancement of Dilute-Acid Total-Hydrolysis Process for High-Yield Saacharification of Cellulosic Biomass*, Subcontract Final Report.
6. Qian, X.; Nimlos, M.R.; Johnson, D.K.; and Himmel, M.E. *Applied Biochemistry and Biotechnology* (accepted).
7. Antal, M.J.; Leesomboon, T.; Mok, W.S.; and Richards, G.N. (1991), *Carbohydrate Research* 217, 71-85;
8. CPMD3.7, copyrighted jointly by IBM Corp and by Max-Planck Institute, Stuttgart; <http://www.cpmd.org>.
9. Johnson, D.K.; Davis, M. (2003), *Identify Reaction Pathways in Dilute Cellulose Hydrolysis to Improve Mass Balance Closure at High Conversions*, NREL Biomass Program P-Milestone Completion Report.

ELECTRONIC STRUCTURE CALCULATIONS OF THE DECOMPOSITION OF XYLOSE DURING ACID PRETREATMENT OF BIOMASS

Mark R. Nimlos, Xianghong Qian, David Johnson, Michael E. Himmel

National Renewable Energy Laboratory, Golden, CO 80401

Abstract

We have used electronic structure techniques to study the preliminary chemical processes that occur during the decomposition of protonated xylose. This serves as a model of the decomposition of xylose during the acid pretreatment of biomass. We have determined the proton affinities of all five of the oxygen atoms on xylose and have calculated the reaction barriers for all protonated species. Using Transition State Theory, we obtained rate constants for decomposition at ambient temperature and at 200 °C.

Introduction

Dilute acid pretreatment of biomass is an effective tool for converting hemicellulose and amorphous cellulose into their constituent sugars and exposing crystalline cellulose to enzymatic hydrolysis. The resulting sugars provide a platform for chemical and biological processes to produce renewable fuels and chemicals. Unfortunately, typical acid pretreatment conditions (1 – 2 % acid, 150 – 200 °C) can also lead to the decomposition of sugars and the formation of products that inhibit enzymatic hydrolysis or fermentation. For instance, acid pretreatment of xylan will form xylose, a fermentable sugar. However, xylose can also decompose into furfural,^{1,2} which may be toxic to fermentation organisms. Furthermore, furfural can polymerize, which may block access to the cellulose. Although the decomposition of xylose is important, the mechanisms and rates of its degradation are still unclear.

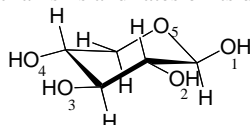


Figure 1. Xylose oxygen atom numbering.

We have started an investigation of xylose decomposition using quantum mechanical modeling. In another study, we have used quantum mechanical molecular dynamics modeling³ (CPMD) to identify likely conformers and reaction pathways. In this study, we use static modeling to obtain activation energies and rate constants for reactions of protonated xylose. We found transition states for the dehydration of xylose protonated at each of the four OH groups. Except for the OH group at O1, dehydration at each of the OH groups is accompanied by a concerted rearrangement. Protonation at the O5, the bridge O atom, results in ring opening.

Computational Methods

We use the Gaussian03 software suite to optimize molecular geometries, in vacuum, of reactants, products and transition states. Initial geometries of xylose and protonated xylose were obtained from CPMD simulations. For transition states, initial geometries were primarily obtained using relaxed Potential Energy Scans, PES, in which the C-O bonds were systematically lengthened while all other internal coordinates were allowed to relax. Initial geometries for the transition states were selected at the potential energy maximum. Transition states geometries were optimized using the Berney algorithm and had exactly one imaginary frequency. Transition states were confirmed by visually examining the

imaginary frequency and by conducting Intrinsic Reaction Coordinate, IRC, calculations. Initial geometry optimizations, PES calculations and IRC calculations were conducted using density functional theory, B3LYP, and a split valance basis set, 6-31G(d). The uncertainty for this level of theory is ± 7.9 kcal mol⁻¹, as estimated by comparison to the G2 set of molecules.⁴ Transition states at this level of theory have often been found to be lower than the experimental transition states⁵ by about 5 kcal mol⁻¹. To improve the calculated energies, we have also calculated energies using the complete basis set method,⁶ CBS-QB3. With this technique, geometries are optimized using B3LYP/6-311G(d,p) and extrapolated to the complete basis set limit using QCISD(T). This technique has a quoted RMS error of 2.1 kcal mol⁻¹ by comparison to the G2 molecule set. We have also found that this technique accurately predicts transition state energies.^{7,8}

Results and Discussion

Proton Affinities. The first step in the proton-assisted decomposition of xylose will be addition of a proton to the oxygen atoms on the sugar. Proton addition is typically a barrier-less process and is characterized by the proton affinity, *PA*, or the standard enthalpy of abstraction of H⁺ from the protonated molecule. Table 1 presents the *PA*s calculated using CBS-QB3. By comparison, we calculated the proton affinity of H₂O, *PA* = 162.5 kcal mol⁻¹ using CBS-QB3, which compares well with the experimental value⁹ of 165 kcal mol⁻¹. As can be seen from the table, the O2 has the largest proton affinity, 191.3 kcal mol⁻¹ and this oxygen atom is most likely site for addition. Protonation at the O1 is least likely because the *PA* at this site is the lowest.

Table 1. Calculated Proton Affinities (PA) and Kinetic Parameters for Decomposition of Xylose

oxygen atom	<i>PA</i> ^a	<i>E_a</i> ^b	<i>A</i> ^c	<i>k</i> _{23°C} ^d	<i>k</i> _{200°C} ^d
O1	186.7	4.4	2.5	1.4×10^{10}	2.3×10^{11}
O2	191.3	16.9	41.1	1.3×10^2	6.1×10^6
O3	188.8	13.9	45.8	2.7×10^4	1.8×10^8
O4	187.2	12.5	31.3	1.8×10^5	5.2×10^8
O5	189.5	9.9	8.8	4.5×10^6	2.4×10^9

^aProton affinities in kcal mol⁻¹ from CBS-QB3 ^bActivation energies in kcal mol⁻¹ (CBS-QB3) for dehydration, except O5, which is ring opening, ^cPre-exponential factors in 10¹³ s⁻¹, ^dTST rate constants in s⁻¹

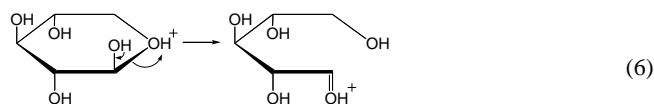
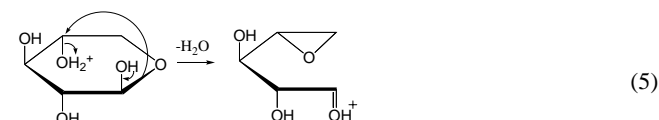
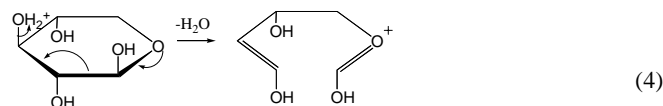
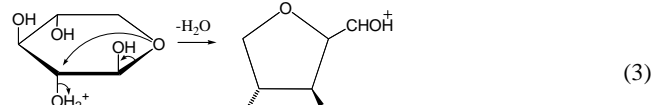
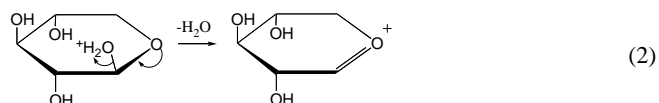
Rate Constants. A likely reaction of the protonated OH groups on xylose is dehydration, while addition of a proton to the O5, the bridge oxygen, should lead to ring opening. For each protonated xylose isomer, we located transition states for these reactions and calculated the energy using CBS-QB3. The activation energies, *E_a*, for each isomer is also collected in Table 1. This energy is the zero-point energy difference between the transition state and the reactant, the protonated xylose. As can be seen, loss of water from xylose protonated at O1 has the lowest activation energy, *E_a* = 4.4 kcal mol⁻¹, followed by ring opening from xylose protonated at O5, *E_a* = 9.9 kcal mol⁻¹. All of the reactions have activation energies lower than 17 kcal mol⁻¹, which suggests that all reactions are possible under pretreatment conditions.

Rate constants for these reactions can also be determined from the electronic structure calculations using Transition State Theory, TST. Pre-exponential factors were determined from the difference in entropy between the transition state and the reactant, ΔS^\ddagger , using the following

$$A = \sigma \left(\frac{k_B T}{h} \right) \left(\frac{1}{RT} \right)^{-\Delta n} \exp(1 + \Delta n) \exp(\Delta S / R) \quad (1)$$

where σ is a symmetry factor, k_B is Boltzman's constant, h is Plank's constant, T is the temperature in K, R is the gas constant and Δn is the molar difference between the transition state and the reactants. Here $\Delta n = 0$. Rate constants for the reactions of the protonated xylose at ambient temperature, 23 °C, and pretreatment temperature, 200 °C are shown in Table 1. As can be seen, at 200 °C, dehydration of the O1 hydroxyl group has the highest rate constant. However, the low proton affinity for this group may make this reaction less likely. The high rate constant and high PA for protonation of O3, O4 and O5 make reactions at these sites most likely.

Mechanisms. The mechanisms for these reactions are shown in (2) to (6). Dehydration of xylose protonated at the O1, reaction (2), results in the formation of an oxonium ion. The stability of this ion results in the calculated low barrier for this reaction, but may prevent further reaction. Addition of water to reform xylose is possible, resulting in no net reaction. Loss of water from protonation at O2, reaction (3), is accompanied by addition of O5 to C2 forming a furanyl compound. This mechanism has been proposed for the formation of furfural from xylose¹. Dehydration of the xylose protonated at O3, reaction (4), results in breaking of the C1–C2 bond. Subsequent reaction may involve loss of formic acid. For the xylose protonated at O4, dehydration, reaction (5), occurs with the formation of an epoxide. Protonation at the bridge oxygen atom results in ring opening as shown in reaction (6). The resulting compound may undergo subsequent dehydration and cyclization to form furfural as proposed elsewhere².



Subsequent reaction of the products in reactions (2) to (6) could lead to the formation of products observed from the decomposition of xylose.¹ It appears likely that different products will result from protonation at the different oxygen atoms in xylose. Protonation at O1 could lead to no net reaction. Dehydration of the furan from reaction (3) could lead to the formation of furfural, which has been reported on numerous occasion in the literature. It is unlikely that the product from dehydration of the OH group at O3, reaction (4), will also lead to furfural formation. Likewise dehydration of the O4 OH group, reaction (5), does not appear to be headed down the pathway to furfural formation. The ring opening reaction (6) may lead to furfural formation, but may also lead to other products.

We plan to conduct additional calculations to determine reaction pathways for the product of reaction (2) to (6) and validate these calculations with experimental measurements. These results should improve our understanding of sugar decomposition and help optimize reaction conditions to minimize it.

Acknowledgement. We would like to acknowledge the financial support of the Office of the Biomass Program of the U. S. Department of Energy.

References

- (1) Antal, Jr., M. J.; Leesomboon, T.; Mok, W. S.; Richards, G. N. *Carbohydrate Res.* **1991**, 217, 71.
- (2) van Dam, H. E.; Kieboom, A. P. G.; van Bekkum, H. *Starch* **1986**, 3, 95.
- (3) Qian, X.; Nimlos, M. R.; Johnson, D. K. Himmel, M. E. *Applied Biochemistry and Biotechnology* Accepted.
- (4) Foresman, J. B.; Frisch, A. E. "Exploring Chemistry with Electronic Structure Methods," 2nd Ed., Gaussian Inc., Pittsburgh, PA, 1995.
- (5) References in Nimlos, M. R.; Blanksby, S. J.; Ellison, G. B.; Evans, R. J. "Enhancement of 1,2-Dehydration of Alcohols by Alkali Cations and Protons: A Model for Dehydration of Carbohydrates", *J. Anal. and Appl.* **2003**, 66, 3.
- (6) Montgomery, J. A., Jr.; Frisch, M. J.; Ochterski, J. W.; Petersson, G. A. *J. Chem. Phys.* **1999**, 110, 2822.
- (7) Nimlos, M. R.; Blanksby, S. J.; Ellison, G. B.; Evans, R. J. *J. Anal. and Appl.* **2003**, 66, 3.
- (8) Hodgson, D.; Zhang, H.-Y.; Nimlos, M. R.; McKinnon, J. T. *J. of Phys. Chem.* **2001**, 105, 4316.
- (9) Hunter, E.P.; Lias, S.G. *J. Phys. Chem. Ref. Data*, **1998**, 27, 413.

IMPACT OF INTRAMOLECULAR HYDROGEN BONDING ON C-O HOMOLYSIS OF LIGNIN MODEL COMPOUNDS: A THEORETICAL STUDY

Phillip F. Britt,¹ Bobby G. Sumpter,² and A. C. Buchanan, III¹

¹Chemical Sciences Division

²Computer Science and Mathematics Division

Oak Ridge National Laboratory

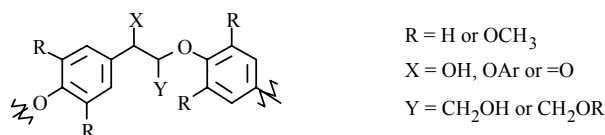
Bethel Valley Road

Oak Ridge, TN 37831

Introduction

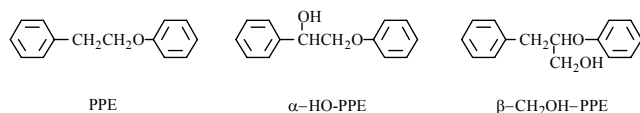
There is a significant amount of interest in the conversion of renewable resources, such as lignin, into higher value products. Lignin, the second most abundant naturally occurring biopolymer and a byproduct of the pulping process, is a source of phenolics, and specialty chemicals and polymers.¹ However, despite the extensive research into the pyrolysis of lignin, the underlying chemical reactions that lead to product formation are poorly understood. Detailed mechanistic studies on the pyrolysis of biomass and lignin under conditions relevant to current process conditions could provide insight into utilizing these renewable resources.

We have undertaken a systematic study of the pyrolysis of lignin model compounds to provide insight into the reaction pathways of lignin.^{ii,iii,iv,v} Since the dominant interunit linkage in lignin is the arylglycerol- β -aryl ether linkage, commonly referred to as the β -O-4 linkage, which accounts for approximately 48-60% of the total interunit linkages,ⁱ we have initially focused our studies on the impact of substituents on the thermal degradation of the β -O-4 linkage (see below). The simplest model of the β -O-4 linkage is



phenethyl phenyl ether (PPE, $R=X=Y=H$). The gas phase and solution phase pyrolysis of PPE was studied to resolve whether the decomposition occurs by a free radical pathway or a concerted retroene reaction.^{ii,iv} At low temperatures (375 °C) and high concentrations, the reaction proceeds by a free radical chain reaction, but at high temperatures (500 °C) and low pressures (flash vacuum pyrolysis (FVP) conditions), the product distribution is dominated by C-O homolysis and unimolecular reactions. It has been found that methoxy groups on the phenolic ring ($R = OCH_3$) enhance C-O homolysis, and under FVP conditions, a wide variety of products were found to arise from intramolecular hydrogen abstraction and rearrangement reactions of the methoxy substituted phenoxy radicals.^{iv}

The impact of hydroxy functional groups ($X=OH$, and $Y=CH_2OH$, see below) on the homolysis of the β -O-4 linkage has also been investigated.^v Surprisingly, the hydroxy substituents



increased the conversion ca. 25-fold compared to PPE even though the substituent is two bonds removed from the breaking C-O bond. The average % conversion (without dehydration) for the FVP of PPE,

α -HO-PPE and β -CH₂OH-PPE at 500 °C was 0.9%, 23.4%, and 22.4%, respectively. This rate enhancement at 500 °C corresponds to a 4.9 kcal mol⁻¹ weakening of the C-O bond (assuming the preexponential factors are the same and that all products result from C-O homolysis). Thermochemical estimates only predict a small effect (ca. 1-4 fold rate enhancement) of the hydroxy group on C-O homolysis.^{vi} Since methylation of the hydroxy groups (to form α -CH₃O-PPE and β -CH₂OCH₃-PPE) decreased the conversion of α -HO-PPE and β -CH₂OH-PPE to 1.3% and 4.0%, respectively, it was proposed that the rate enhancement was a consequence of intramolecular hydrogen bonding. Suryan et al. reported that the C-O bond dissociation energy for *o*-hydroxyanisole was ca. 4.7 kcal mol⁻¹ lower than that of the *p*-hydroxyanisole as a consequence of intramolecular hydrogen bonding.^{vii} Additionally, King and Stock have reported that hydrogen bonding, by phenols or benzoic acid, enhances the rate of decomposition of benzyl phenyl ether and dibenzyl ether.^{viii} However, it is still remarkable that weak hydrogen bonding interactions have such a dramatic influence on the reaction chemistry at high temperatures. Thus, to gain more insight into the impact hydroxy substituents and the role of hydrogen bonding on the homolysis of the β -O-4 linkage, we are using theoretical methods coupled to experimental data to probe the reaction pathways.

Traditionally, it has been difficult to study radicals by theoretical methods due to the highly delocalized, extensively correlated nature of radicals. The phenoxy radical has historically been a very difficult case for theoretical calculations as a consequence of the possibilities of spin contamination of the wave functions and strong nondynamical correlation effects in the pi system, which leads to a broad range of calculated C-O bond distances. By combining experimental FVP studies of hydroxy substituted lignin model compounds with computational quantum chemistry, we will be able to develop a new mechanistic understanding of the role of hydrogen bonding on the reaction pathways. In this investigation, our initial computational results indicate that hydrogen bonding stabilizes the transition state for C-O dissociation of the ether linkage in α -HO-PPE by ca. 3 kcal mol⁻¹ compared to PPE.

Experimental

The synthesis of PPE,ⁱⁱ α -HO-PPE,^v β -CH₂OH-PPE^v has been previously described. The methyl ethers were prepared by reaction of the alcohol with NaH in THF followed by the addition of CH₃I.

The FVP apparatus has been previously described.^{iv} FVP experiments were run at low pressures (typically 10⁻⁴ Torr) in which the concentration of reactants, intermediates, and products are kept low (10⁻⁸ - 10⁻⁹ M) so that only unimolecular reactions can occur and fast bimolecular reactions, such as radical couplings. Contact times were estimated to be between 0.2 and 0.4 s (by pyrolysis of phenethyl acetate) and products were rapidly quenched in a cold trap (at 77 K) so that reactive intermediates could be isolated. Products were analyzed by GC-MS and quantitated by GC-FID as previously described.^{iv}

Computational Methods. We used many-body (MBPT) electronic structure and density functional theory (DFT) to study the homolysis of hydroxy substituted phenethyl phenyl ethers (PPE). For the majority of the calculations, a polarized double and triple zeta basis set with and without diffuse functions (6-31G**, 6-311G**, 6-311+G*, 6-311++G**) was used for both types of quantum calculations. Computations using DFT were performed within the local-density and generalized-gradient approximations (LDA and GGA). The Vosko-Wilk-Nusair parameterization^{ix} was adopted for LDA, and the PW91^x, PBE96^{xi}, and hybrid B3LYP^{xii} exchange-correlation functionals for GGA. We also have examined

more extensive basis sets (Dunning's correlation consistent basis functions aug-cc-pVDZ and aug-cc-pVTZ)^{xiii} and higher levels of theory, CASSCF (complete active-space multiconfiguration SCF, active space of 6 electrons and 4 orbitals along with the Pople type basis sets), and CCSD (coupled cluster singles and doubles). The homolysis of α -HO-PPE was examined by first performing a full geometry DFT or Moller Plesset 2nd order perturbation theory (MP2) optimization followed by optimization along an increasing C-O bond length (from the equilibrium value to a displacement large enough that there was approximate asymptotic convergence in the energy). This procedure can give a good estimate of the reaction coordinate. The approximate transition state, provided that one exists, can be located by examining the computed energy profile and performing a saddle point search at the geometry corresponding to an energy barrier (see Figure 1 below). All quantum chemistry calculations were performed using the NWChem software package.^{xiv}

Results and Discussion

Figure 1 shows an energy profile (difference between the equilibrium energy and the energy at specific C-O bond lengths) for α -HO-PPE as determined by using unrestricted MP2 (UMP2)^{xv} with the 6-31G** basis set (corrected for basis set superposition error, BSSE, by using the counterpoise method^{xvi}). At a C-O bond distance of 2.1 angstroms the energy barrier is 57 kcal mol⁻¹, and a saddle

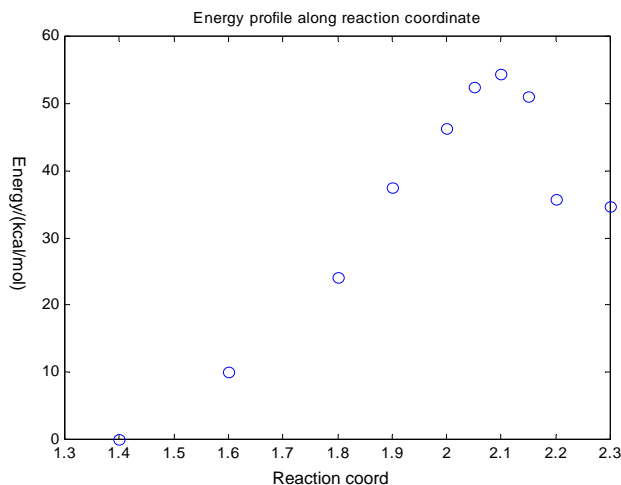


Figure 1. Energy profile along the reaction coordinate for homolysis of α -OH PPE (C-O bond). The UMP2/6-31G** computed barrier height is 57 kcal mol⁻¹.

point search starting from this configuration confirms this to be a transition state. The geometry and electrostatic isosurface of the UMP2/6-31G** determined transition state is shown in Figure 2. It is clear from examining the total charge density that the hydrogen atom on the α -hydroxy group is strongly interacting with the phenoxy radical, and it is in fact forming a weak hydrogen bond. Comparing this result to that determined for PPE, there is a difference of ca. 3 kcal mol⁻¹. This small energy difference is enough to result in a reaction rate, as computed from Transition State Theory, that is ~ 10 times faster than PPE. These computational results are in very good agreement with the experimental results. However, it is interesting to note that the calculated activation energy for C-O homolysis for PPE (60 kcal mol⁻¹) is lower than that estimated by group additivity methods (65 kcal mol⁻¹).^{iv} It was determined that larger basis sets do tend to effect the position of the

transition state but the activation energy trends (difference between hydroxyl substituted and un-substituted PPE) are reasonably consistent. We are currently investigating other computational methods to determine the best method to describe hydrogen bonding to radicals, and we are investigating other lignin model compounds such as β -CH₂OH-PPE and α -HO- β -CH₂OH-PPE to determine the impact of hydrogen bonding on C-O homolysis.

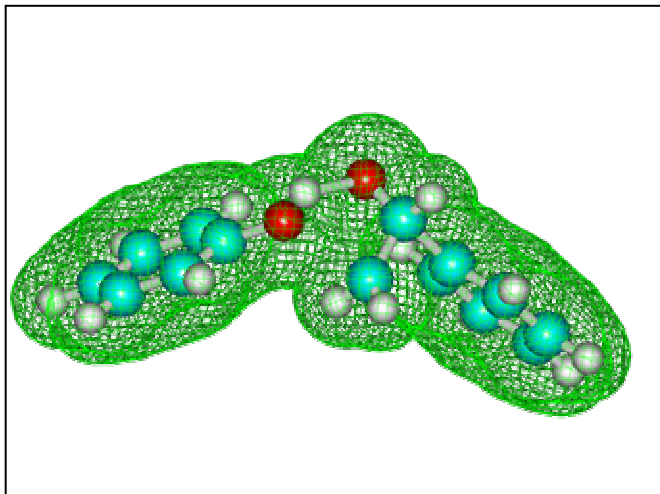


Figure 2. Electrostatic isosurface for the transition state of α -hydroxy PPE.

Acknowledgment

This research was sponsored by the Division of Chemical Sciences, Geosciences and Biosciences, Office of Basic Energy Sciences, U.S. Department of Energy, under contract DE-AC05-00OR22725 with Oak Ridge National Laboratory, managed and operated by UT-Battelle, LLC.

References

- (i) *Lignin: Historical, Biological, and Materials Perspectives*; Glasser, W. G.; Northey, R. A.; Schultz, T. P., Eds.; ACS Symposium Series 742; American Chemical Society: Washington, DC, 2000.
- (ii) Britt, P. F.; Buchanan, A. C., III; Malcolm, E. A. *J. Org. Chem.* **1995**, 60, 6523.
- (iii) Britt, P. F.; Buchanan, A. C., III; Thomas, K. B.; Lee, S.-K. *J. Anal. Appl. Pyrolysis* **1995**, 33, 1.
- (iv) Britt, P. F.; Buchanan, A. C., III; Cooney, M. J.; Martineau, D. R. *J. Org. Chem.* **2000**, 65, 1376.
- (v) Cooney, M. J.; Britt, P. F.; Buchanan, A. C., III *Prepr. Pap.-Am. Chem. Soc., Div. Fuel Chem.* **1997**, 42(1), 89.
- (vi) Benson, S. W. *Thermochemical Kinetics*, 2nd ed.; Wiley & Sons: New York, 1976.
- (vii) Suryan, M. M.; Kafafi, S. A.; Stein, S. E. *J. Am. Chem. Soc.* **1989**, 111, 1423.
- (viii) King, H.-H.; Stock, L. M. *Fuel* **1984**, 63, 810.
- (ix) Vosko, S. H.; Wilk, L. Nusair, M. *Can. J. Phys.* **1980**, 58, 200.
- (x) (a) Perdew, J. P.; Burke, K.; Wang, Y. *Phys. Rev. B.* **1996**, 54, 16533; (b) Burke, K.; Perdew, J. P.; Wang, Y. in *Electronic Density Functional Theory: Recent Progress and New Directions*; Dobson, J. F.; Vignale, G.; Das, M. P., Eds.; Plenum: New York, 1998.
- (xi) Perdew, J. P.; Burke, K.; Enzerhof, M. *Phys. Rev. Lett.*, **1996**, 77 (18), 3865.
- (xii) Beke, A. D. *J. Chem. Phys.* **1993**, 98, 5648.

-
- (xiii) (a) Dunning, T. H., Jr.; *J. Chem. Phys.* **1989**, *90*, 1007; (b) Kendall, R. A.; Dunning, T. H., Harrison, R. J. *J. Chem. Phys.* **1992**, *96*, 6796.
- (xiv) (a) Straatsma, T. P.; Aprà, E.; Windus, T. L.; Bylaska, E. J.; de Jong, W.; Hirata, S.; Valiev, M.; Hackler, M.; Pollack, L.; Harrison, R.; Dupuis, M.; Smith, D. M. A.; Nieplocha, J.; Tipparaju V.; Krishnan, M.; Auer, A. A.; Brown, E.; Cisneros, G.; Fann, G.; Früchtl, H.; Garza, J.; Hirao, K.; Kendall, R.; Nichols, J.; Tsemekhman, K.; Wolinski, K.; Anchell, J.; Bernholdt, D.; Borowski, P.; Clark, T.; Clerc, D.; Dachsel, H.; Deegan, M.; Dylla, K.; Elwood, D.; Glendening, E.; Gutowski, M.; Hess, A.; Jaffe, J.; Johnson, B.; Ju, J.; Kobayashi, R.; Kutteh, R.; Lin, Z.; Littlefield, R.; Long, X.; Meng, B.; Nakajima, T.; Niu, S.; Rosing, M.; Sandrone, G.; Stave, M.; Taylor, H.; Thomas, G.; van Lenthe, J.; Wong, A.; Zhang, Z.; *NWChem, A Computational Chemistry Package for Parallel Computers, Version 4.6* (2004), Pacific Northwest National Laboratory, Richland, Washington 99352-0999, USA. *High Performance Computational Chemistry: an Overview of NWChem a Distributed Parallel Application*, (b) Kendall, R. A.; Aprà, E.; Bernholdt, D. E.; Bylaska, E. J.; Dupuis, M.; Fann, G. I.; Harrison, R. J.; Ju, J.; Nichols, J. A.; Nieplocha, J.; Straatsma, T. P.; Windus, T. L.; Wong, A. T. *Computer Phys. Comm.*, **2000**, *128*, 260-283 .
- (xv) Moller, C.; Plesset, M. S. *Phys. Rev.* **1934**, *46*, 618.
- (xvi) Boys, S. F.; Bernardi, F. *Mol. Phys.* **1970**, *19*, 553.

PYROLYSIS OF BENZYL PHENYL ETHER CONFINED IN MESOPOROUS SILICAS

A. C. Buchanan, III, Michelle K. Kidder, and Phillip F. Britt

Oak Ridge National Laboratory
Chemical Sciences Division
Bethel Valley Road
P.O. Box 2008, MS-6197
Oak Ridge, Tennessee 37831-6197

Introduction

Our prior research on the impact of restricted mass transport during the pyrolysis of fuel model compounds has focused on molecules attached to the surface of nonporous silica nanoparticles.¹ Recently, we began examining the influence of pore confinement and pore size on the pyrolysis of fuel model compounds through the use of ordered mesoporous silicas such as SBA-15 and MCM-41.² These mesoporous silicas are being widely investigated for many potential applications in catalysis, separations, and the synthesis of nanostructured materials.³⁻⁶ In a recent communication, we reported that the pyrolysis of 1,3-diphenylpropane (DPP) confined in mesoporous silicas resulted in altered reaction rates and product selectivities compared with confinement on the nonporous silica, Cabosil.² In particular, the pyrolysis rate is enhanced in the mesoporous silicas and appears to increase as the pore size decreases (varied from 5.6 to 1.7 nm). Further analysis at similar DPP surface densities on MCM-41 and Cabosil indicates a rate enhancement of 4-5 at 375°C.⁷ The DPP reaction is a radical chain process whose rate is controlled by bimolecular hydrogen transfer steps. Pore confinement enhances the rate of these steps through enhanced encounter frequencies and, perhaps, improved geometries for hydrogen transfer on the surface. We have recently demonstrated that improved orientations for hydrogen transfers on silica surfaces can lead to faster reaction rates in free-radical reactions.^{8,9}

In the current work, we extend these investigations on pore confinement to benzyl phenyl ether (PhCH₂OPh; BPE), which serves as a model for related α -aryl ether linkages in the renewable resource, lignin. In contrast to DPP, the rate of BPE pyrolysis is controlled by the initial unimolecular homolysis of the weak C – O bond.¹⁰ We have now immobilized BPE on the surface of three hexagonal mesoporous MCM-41 silicas having mean pore diameters of 2.7, 2.2, and 1.7 nm. The attachment reaction involves condensation of a phenolic derivative of BPE with the surface silanols of the mesoporous silicas, which establishes a thermally robust Si – O – C_{aryl} linkage to the surface. The pyrolysis rate and product selectivity will be compared with previous results obtained on Cabosil.¹⁰

Experimental

Materials. The MCM-41 silicas were synthesized according to literature procedures.¹¹ Controlled variation in the size of the structure directing template, C_nH_{2n+1}N(CH₃)₃Br [n = 16, 14, 12], produced three structurally related hexagonal mesoporous silicas with mean pore diameters of 2.7, 2.2, and 1.7 nm, respectively. The BET surface areas for these materials were 1150, 1194, and 1285 m² g⁻¹, respectively. The phenol *m*-HOC₆H₄OCH₂C₆H₅ (HOBPE) was synthesized and purified as previously described.¹⁰

Surface-Attachment Reaction. A sample of MCM-41 was dried in an oven at 200 °C for 4 h and then cooled to room temperature in a desiccator prior to use. The silica (1 g, ca. 4.5 mmol SiOH) was slurried with dry benzene (15 mL), excess HOBPE (2.6 g, 13.0 mmol) was added and the mixture stirred for 10 min, and the solvent was removed on a rotary evaporator. The solid was

transferred to a Pyrex glass reaction tube, evacuated overnight, sealed at $< 5 \times 10^{-5}$ Torr, and the attachment reaction was conducted at 200 °C for 1 h in a fluidized sand bath. The sample was transferred to another tube, connected to a dynamic vacuum at 5×10^{-3} Torr, and heated in a tube furnace from 135 – 205 °C in 10 °C steps with 10 min hold periods to remove unattached HOBPE. The solid was then transferred into a fritted funnel and extracted with anhydrous diethyl ether until GC analysis showed no traces of HOBPE in the extract. The resulting solid was dried under vacuum overnight. Surface coverages were determined from carbon elemental analysis (Galbraith Laboratories). These were confirmed by chemical analysis using the same base hydrolysis procedure described below. The materials were stored in a desiccator under vacuum.

Pyrolysis Procedure. A weighed amount of sample (ca. 50 mg) was placed in one end of a T-shaped Pyrex tube, evacuated, and sealed at $< 5 \times 10^{-6}$ Torr. The sample was inserted into a temperature controlled, three zone tube furnace (275 ± 1 °C) fitted with a copper sample holder, and the other end was placed in a liquid nitrogen bath. The gas-phase products were collected in the cold trap, and dissolved in acetone (0.2 – 0.3 mL) containing cumene, 3,4-dimethylphenol, and 4-phenylphenol as standards. These products were analyzed by GC and GC-MS as described previously.¹⁰ The surface-attached products were similarly analyzed following base hydrolysis (1 N NaOH, 30 mL) of the solid residue (30 mg), addition of the two phenolic standards in 1 N NaOH, acidification with HCl, extraction with diethyl ether, drying over MgSO₄, filtration, and solvent evaporation. The products from the residue, which are phenol derivatives, were silylated with *N,O*-bis-(trimethylsilyl)-trifluoroacetamide : pyridine (1:2) prior to GC and GC-MS analysis.

Results and Discussion

BPE was bound to the MCM-41 with 2.7 nm pore diameter at high surface coverage for comparison with the earlier results on Cabosil. The BPE molecules are attached to the pore wall by condensation of the phenolic precursor with the silanols to form Si – O – C_{aryl} linkages (visualized in Figure 1). Higher densities were achieved on the MCM-41 most likely due to the addition of a sublimation step (see Experimental) not employed on Cabosil, which results in a higher efficiency for BPE attachment. This material was characterized by diffuse reflectance FTIR, ¹³C-NMR, and BET (nitrogen) surface analysis.

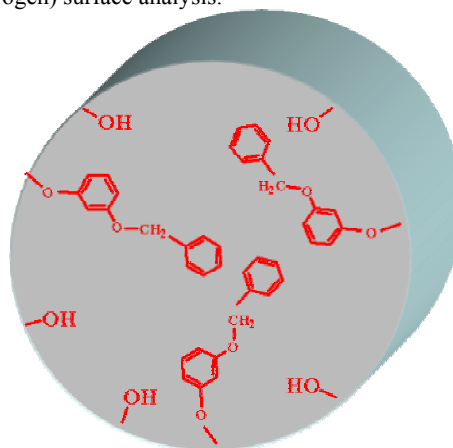


Figure 1. Benzyl phenyl ether immobilized in a mesoporous silica.

Pyrolysis of this material at 275°C gave the same suite of products as identified previously when BPE was immobilized on Cabosil.¹⁰ The initial rate-controlling step is homolysis of the weak

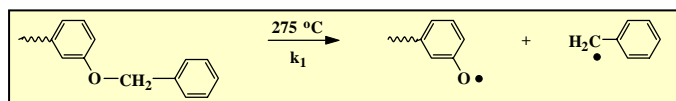


Figure 2. Initial rate-controlling homolysis step in the pyrolysis of BPE in the mesoporous silica. The jagged line denotes position of attachment to the silica surface.

(ca. 52 kcal mol⁻¹) central O – C bond to produce surface-bound phenoxy and gas-phase benzyl radicals as shown in Figure 2. The rate constant for this step can be measured by following the products formed from their reaction. These involve radical recombination at the phenoxy radical ring position to form isomers of surface-bound benzylphenol (Eq. 1), and hydrogen abstraction from BPE to form surface-bound phenol (Eq. 2) and gas-phase toluene (Eq. 3) as shown in Figure 3.

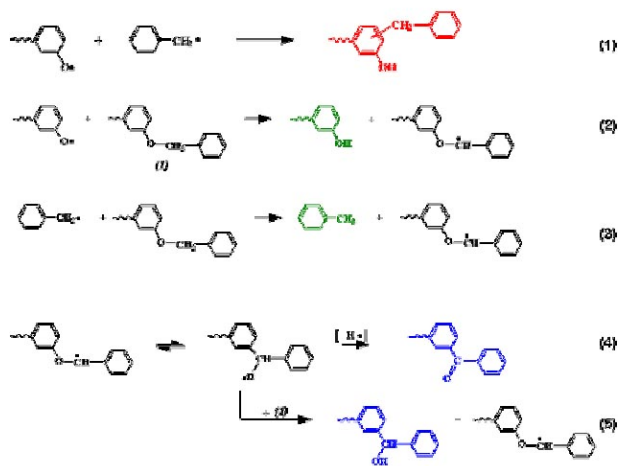


Figure 3. Formation of principal products in the pyrolysis of BPE in mesoporous silica. The jagged line denotes a surface-attached product.

The measured homolysis rate constant (average of 6-runs) is shown in Table 1 along with previously measured values for BPE bound to Cabosil at high surface densities. The value of the first order rate constant should be independent of the surface density of BPE molecules as illustrated for the Cabosil case. The MCM-41 results suggest that pore confinement results in a ca. 3-fold decrease in this rate constant, perhaps a result of a cage effect in the pore. This effect will be examined further through the study of BPE immobilized in the smaller pore size MCM-41's with pore diameters of 2.2 and 1.7 nm.

Table 1. Comparison of Homolysis Rate Constant (275 °C) and Reaction Path Selectivity for BPE bound to MCM-41 and Cabosil

Silica	BPE Surface Density (nm ⁻²)	k ₁ x 10 ³ (s ⁻¹)	Path Selectivity ^a
MCM-41 (2.7 nm pore)	1.14	0.56 ± 0.06	0.77
Cabosil	0.76	1.5 ± 0.1	1.00
Cabosil	0.56	1.4 ± 0.1	1.34

^a Ratio of surface-bound benzylphenols (Eq. 1) to surface bound benzophenone (Eq. 4) plus surface-bound benzhydryl (Eq. 5). Estimated error is ± 5 %.

One of the interesting discoveries in our previous studies of BPE pyrolysis on Cabosil was the emergence of a significant new pathway not previously detected in the gas-phase or liquid-phase pyrolysis of BPE.¹⁰ This pathway (Figure 3, Eqs. 2 – 5) involves the formation of surface-bound benzophenone (Eq. 4) and benzhydryl (Eq. 5) products following an O – C phenyl shift in the intermediate carbon-centered radical shown in the figure. The path selectivity for BPE reaction via radical recombination to form surface-bound benzylphenols (Eq.1) vs. the phenyl shift rearrangement path to form the surface-bound benzophenone and benzhydryl is reported in Table 1. We can see that this selectivity is less than 1.0 and lower for the MCM-41 than for the Cabosil indicating a preference for the phenyl shift path. However, this comparison needs to be made at similar BPE surface densities, since the path selectivity will be dependent on this parameter as previously observed on Cabosil.¹⁰ Hence, future work will not only examine BPE pyrolysis selectivity on the smaller pore size MCM-41s, but also on Cabosil at a higher surface density more comparable with that of the mesoporous silicas.

Conclusions

Pyrolysis of BPE confined in mesoporous MCM-41 with a 2.7 nm pore diameter proceeds to give the same suite of products detected previously on the nonporous Cabosil nanoparticles. However the rate is reduced possibly as a consequence of a cage effect in the porous solid. The rearrangement path involving an O – C phenyl shift producing the benzophenone and benzhydryl products on the surface appears to be more favored than observed previously on Cabosil, but additional studies are required at more comparable surface coverages as indicated above. Future studies will examine the influence of the MCM-41 pore size on the pyrolysis rate and path selectivity.

Acknowledgment. This research was sponsored by the Division of Chemical Sciences, Geosciences, and Biosciences, Office of Basic Energy Sciences, U.S. Department of Energy under contract DE-AC05-00OR22725 with Oak Ridge National Laboratory, managed and operated by UT-Battelle, LLC.

References

- (1) Buchanan, A. C., III; Britt, P. F. *J. Anal. Appl. Pyrolysis* **2000**, *54*, 127.
- (2) Kidder, M. K.; Britt, P. F.; Zhang, Z.; Dai, S.; Buchanan, A. C., III *Chem. Commun.* **2003**, 2804.
- (3) Thomas, J. M.; Johnson, B. F. G.; Raja, R.; Sankar, G.; Midgely, P. A. *Acc. Chem. Res.* **2003**, *36*, 20.
- (4) Lee, B.; Bao, L.-L.; Im, H.-J.; Dai, S.; Hagaman, E. W.; Lin, J. S. *Langmuir* **2003**, *19*, 4246.
- (5) Stein, A.; Melde, B. J.; Schroden, R. C. *Adv. Mater.*, **2000**, *19*, 1403.
- (6) Che, S.; Liu, Z.; Ohsuna, T.; Sakamoto, K.; Terasaki, O.; Tatsumi, T. *Nature* **2004**, *429*, 281.
- (7) Buchanan, A. C., III; Kidder, M. K.; Britt, P. F., unpublished results.
- (8) Buchanan, A. C., III; Kidder, M. K.; Britt, P. F. *J. Am. Chem. Soc.* **2003**, *125*, 11806.
- (9) Buchanan, A. C., III; Kidder, M. K.; Britt, P. F. *J. Phys. Chem. B* **2004**, *108*, 16772.
- (10) Buchanan, A. C., III; Britt, P. F.; Skeen, J. T.; Struss, J. A.; Elam, C. L. *J. Org. Chem.* **1998**, *63*, 9895.
- (11) Jarupatrakorn, J.; Tilley, T. D. *J. Am. Chem. Soc.* **2002**, *124*, 8380.